

Atrial activation time estimation using cross-correlation between higher order neighboring electrodes

in epicardial electrograms

by

B. Kölling

to obtain the degree of Master of Science
at the Delft University of Technology,

Student number: 4228219
Project duration: September 3, 2018 – September 27, 2019
Thesis committee: Dr. ir. Richard C. Hendriks, TU Delft, supervisor
Dr. Borbala Hunyadi, TU Delft
Prof. Dr. Natasja M. S. de Groot, Erasmus MC
Bahareh Abdikivanani MSc, TU Delft

An electronic version of this thesis is available at <http://repository.tudelft.nl/>.

Preface

The subject of this thesis is the mapping of the electrical activity in the human atria, to gain a better understanding of the tissue's conductive properties. More insight into the behaviour of the cardiac tissue will help better understand the mechanisms that could lead to cardiac arrhythmias.

This research is part of the Medical Delta Cardiac Arrhythmia Lab, a joint project between Erasmus MC, LUMC and TU Delft. This particular topic was part of a project between two research groups, the Circuits and Systems (CAS) group from TU Delft and the Department of Cardiology from Erasmus MC. In the thesis committee dr.ir. R.C. Hendriks, dr. B. Hunyadi and B. Abdikivanani MSc represent TU Delft and prof.dr. N.M.S. de Groot represents Erasmus MC.

B. Kölling
Delft, September 2019

Acknowledgements

Firstly I would like to sincerely thank my supervisors, Richard Hendriks and Bahareh Abdi. The regular meetings helped keep the thesis project progressing steadily and there was always room for productive discussions aiding in determining the final direction of this thesis.

I also would like to thank the people at the Department of Cardiology at Erasmus MC for taking the time to provide information about and insight into the clinical side on this research project.

Furthermore, would like to thank my family for supporting me throughout my student career.

Lastly I would like to thank the Electrotechnische Vereeniging for the facilitation of sufficient coffee breaks during this thesis project and the years before.

Contents

1	Introduction	1
2	Electrical activity of the human atria	3
2.1	Electrical conductivity in the human heart	3
2.1.1	Electrical conduction in cardiac cells	3
2.1.2	The human atrial action potential	4
2.1.3	The surface electrocardiogram.	5
2.2	Atrial Fibrillation	6
2.2.1	Classification of AF.	6
2.2.2	Mechanisms of AF	6
2.2.3	Treatment	6
2.3	Epicardial mapping	7
2.3.1	The epicardial electrogram.	8
2.4	Local activation times.	8
2.4.1	Local activation time estimation	9
2.4.2	Steepest (Negative) deflection	9
2.4.3	Cross-correlation	10
2.4.4	Deconvolution.	10
2.4.5	Spatial gradient	11
2.4.6	Template matching	11
3	Simulated and recorded atrial electrogram data	13
3.1	Simulated data	13
3.1.1	Simulation	13
3.1.2	Data sets	13
3.1.3	Example of simulated electrograms	14
3.2	Real-world data	16
3.2.1	Data format	16
3.2.2	Data acquisition	16
4	LAT estimation using cross-correlation estimation over higher order neighbors	19
4.1	The atrial epicardial electrogram as separate excitation waves	19
4.2	Spatial structure of the data.	20
4.2.1	Graphs	20
4.2.2	Grid graphs	21
4.2.3	Higher order neighbors in the electrode array	21
4.3	Cross-correlation over higher order neighbors	23
4.3.1	Relation of cross-correlation to maximum likelihood	25
4.4	From inter-electrode lag to LAT	26
4.4.1	Assuming equal noise variances	26
4.4.2	Assuming unequal, unstructured noise variances	27
4.4.3	Assuming unequal, structured noise variances.	28
4.4.4	Off-diagonal elements in the noise covariance matrix	30
4.4.5	Cramér-Rao lower bound	31
4.4.6	Combination with steepest deflection estimates	31
4.5	Data window determination and comparison.	32
4.5.1	Time windowing	32
4.5.2	Determining fractionated electrodes.	33
4.5.3	Performance metric	33

5	Results	35
5.1	Experiments on simulated data	35
5.1.1	Data sets used	35
5.1.2	Cross-correlation over a higher order neighbors	35
5.1.3	Dependence on regularization	41
5.1.4	Comparison with gradient method	41
5.1.5	Ignoring close neighbors	41
5.1.6	Combining steepest deflection and cross-correlation	44
5.1.7	Estimation of error covariance matrix	46
5.2	Experiments on real-world, clinical data	48
5.2.1	Time windowing	48
5.2.2	Regular sinus rhythm	48
5.2.3	Signals with disturbances	49
5.2.4	Multiple wavefronts	51
6	Conclusions	55
6.1	Summary of results	55
6.2	Future work	56
A	CRLB derivation	57
B	List of Abbreviations and Symbols	59
	Bibliography	61

Introduction

Globally, the number one cause of death is cardiovascular disease [1]. The total direct (medical expenses) and indirect (loss of productivity) cost to society from cardiovascular diseases is more than any other diagnostic group [2].

From this group of cardiovascular diseases, a common cardiac arrhythmia is atrial fibrillation (AF). With increased age, the incidence of AF increases, and AF is associated with a higher overall risk of mortality [3]. Worldwide, atrial fibrillation is becoming more widespread [4]. Currently there is some understanding about the mechanisms behind AF, however a global consensus is absent which hinders the progress in treatment of the disease [5]

More than a century ago, tools were first developed for visualizing and recording cardiac activity. The contraction of the cardiac muscle cells is governed by electrical potentials and currents. To measure this process Electrocardiography was developed, which has as a goal to record the electrical activity of the heart. This was first accurately measured with the string galvanometer developed by Willem Einthoven [6], [7]. Electrical leads were attached to the limbs of patient and from those leads a current could be measured. Subsequent discoveries resulted in the now common 12-lead ECG method [8].

Recording the ECG with electrodes on the body surface of a patient gives an impression of the total electrical activity of the heart. Obtaining information about the localized activity in the cardiac tissue is difficult in this setting. Therefore, invasive mapping studies have been performed where an array of electrodes is used to record the electrical activity on the heart's surface during open-chest surgery [9]. From these epicardially recorded signals the depolarization of the tissue can be attempted to be recovered at a higher spatial resolution.

The recorded electrograms from this invasive approach need to be processed to obtain proper estimates of the underlying activity. The moment in time when the tissue under an electrode depolarizes, called the local activation time (LAT), is particularly of interest. This information about the activation times can be used to reconstruct the propagation pattern of the signal that triggers the tissue to contract. The path that this "wave" of activations takes can reveal obstructions due to conductivity problems or interfering sources, resulting in multiple wavefronts being present.

There are multiple methods to estimate the LAT from the epicardial electrogram. Manual annotation can be done by a physician and has as an advantage that the expert can review and interpret the signals carefully. These signals can become quite complex in morphology. Multiple automated solutions are also available, most notable is the so called steepest (negative) deflection [10]. This uses the point of maximum negative slope (maximum negative derivative) of an electrogram signal as the LAT.

Methods using the cross-correlation have also been applied previously to the epicardial signals [11]. The cross-correlation is a powerful tool in situations where the delay between two similar signals is sought. The result from cross-correlating a pair of signals is a spectrum, with a maximum from which the delay can be derived. Cross-correlation thus does not directly provide LATs for the whole electrode array, only differences in the LAT of pairs of signals.

In this thesis the application of the cross-correlation for the mapping of atrial signals is investigated. Specifically the benefits of not only cross-correlating electrode pairs that are close, but also those with a larger distance between them is of interest. To be more specific,

- A framework is developed to estimate the LAT based on the cross-correlation between a pair of electrodes. A graph structure is used to define which electrode pairs are considered when calculating the cross-correlation. These are not only the direct neighbouring electrodes, but also pairs of electrodes that we define as higher order neighbors, that are, pairs of electrodes where their shortest distance in terms of electrodes-to-electrode hops in the graph structure is equal to or less than a specific number.
- The inter-electrode delays obtained from cross-correlation are used to estimate the LATs using a least-squares estimator. Different assumptions for the underlying error model are investigated and estimators are formulated for each model.
- A simulation of a 2D section of atrial tissue with specific patterns of non-conducting cells is used to generate several data sets. First, a set of artificial shapes of conduction blocking cells is simulated to magnify the differences between methods. Then a set of more realistic patterns of non-conducting cells is also simulated.
- The estimation of LATs using cross-correlation over higher order neighbors is shown to improve performance over only using direct neighbors on the simulated data sets.
- The performance of the cross-correlation LAT estimation is shown to be better than other commonly used methods such as the steepest deflection method when using higher order neighbors, when they are applied to the range of simulated data sets.
- On real-world signals recorded from patients during open-heart surgery, it is shown that the estimates of the LATs of the cross-correlation method can deviate significantly from those estimated with a steepest deflection method.
- The observed differences when using the real-world signals are illustrated using some examples, to highlight the possible advantages and disadvantages of the methods.

Outline This thesis is organized as follows: In Chapter 2 first the electrical properties of the cells in the atria are briefly explained. Then epicardial mapping is introduced and different methods of LAT estimation from the epicardial electrograms are discussed. In Chapter 3 the simulation that is used to generate the simulated data is discussed, along with the method with which the data from real-world patients was obtained. In Chapter 4 the cross-correlation method using higher order neighbors is introduced and the estimation of LATs from the obtained delays is discussed. In Chapter 5 the methods from Chapter 2 are compared to those developed in Chapter 4. They are compared on both simulated and real-world clinical data. In Chapter 6 the conclusions from those results are discussed and future work is considered.

2

Electrical activity of the human atria

In this chapter, the electrical activity of the human atria is discussed. Methods to model and measure the underlying mechanisms of the electrical activity are investigated, as the malfunctioning of these mechanisms is responsible for cardiac arrhythmias such as atrial fibrillation. In Section 2.1 the electrical conductive properties of the cells in the human heart are first introduced, followed by a model of the human atrial myocytes. In Section 2.2 atrial fibrillation is discussed as a malfunctioning of the regular conduction pattern in the atria. Epicardial mapping can be used to get a better understanding of the processes underlying atrial fibrillation in the cardiac tissue and is discussed in Section 2.3. Finally in Section 2.4 it is discussed how the recorded data can be used to obtain the activation pattern of the cells based on the estimated local activation time. This can be used to determine whether an area of slow or blocked conduction is present. Methods to estimate these local activation times are also explained.

2.1. Electrical conductivity in the human heart

The human heart has as a function to pump blood around the body. This blood then supplies oxygen and nutrients to the body and takes waste products with it. An image of the human heart and its key components is shown in Fig. 2.1.

The human heart consists of four chambers. These are, the left atrium and ventricle and the right atrium and ventricle. There are four valves in the heart, two between the atria and the ventricles, and two between the ventricles and the arteries. The upper and lower systemic veins enter the right atrium, the right ventricle pushes blood originating from those veins to the pulmonary arteries leading to the lungs. The pulmonary veins then transport oxygen-rich blood to the left atrium. Blood then flows to the left ventricle and is pushed into the Aorta [13].

2.1.1. Electrical conduction in cardiac cells

The cardiac muscle cells (cardiac myocytes) contract due to an electrical signal propagating through the muscle tissue. Cells that activate (depolarize) then trigger their neighboring cells and as such the signal is conducted. This is regulated by a network of conducting (pacemaker) cells that determine the rate of contraction.

The electrical impulses in the heart normally originate from the sinoatrial node (SA node). The tempo of contraction governed by the SA node is called sinus rhythm (SR). The impulse from the SA node causes the atria to contract first. The electrical signal then travels through the network of conducting cells to the atrioventricular node (AV node) and then to the ventricles through the bundle of His. This conduction is slower allowing blood to fill the ventricles before it is pumped into the arteries when the ventricles contract [13].

The conduction velocity (CV) through the cardiac muscle is not equal in all directions (not isotropic) [14]. The anisotropic ratio is defined by the ratio between the conduction velocity in the primary direction versus the orthogonal secondary direction of conduction. In the cardiac myocytes the primary direction is the longitudinal direction of the fibers, and the secondary is the transverse direction.

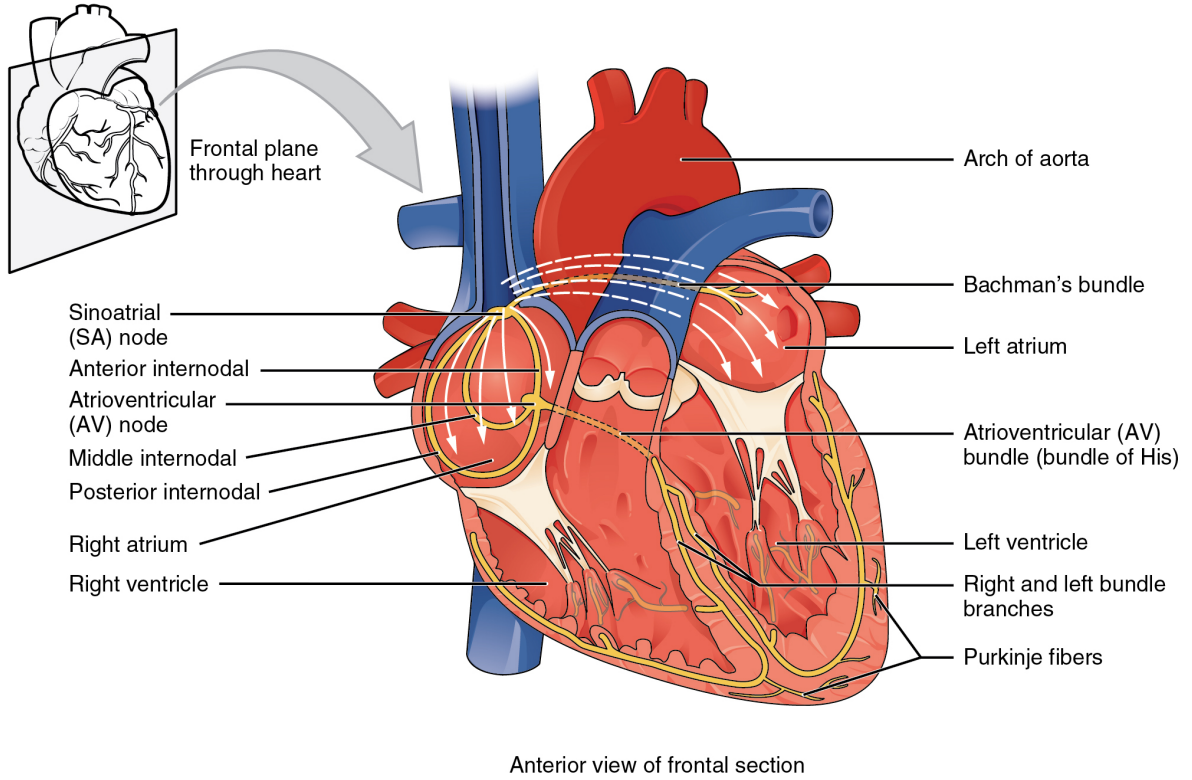


Figure 2.1: The human heart with the conduction system highlighted (via www.openstax.org, 2013. Accessed 5-9-2018 [12])

2.1.2. The human atrial action potential

The depolarization of a cell manifests electrically by a shift in the electrical potential of the cell when it is excited by neighboring cells or by another source. The resulting pattern in the potential is called the action potential (AP). The morphology of the AP depends on the type of excitable cell.

Under normal conditions the AP for the atrial myocytes follows a regular pattern, shown on the right in Fig. 2.2. The changes in potential are a consequence of multiple ionic current flows during the depolarization and repolarization process. The AP is believed to be mostly controlled by the inward sodium and calcium currents and four different potassium currents, among other currents [15].

The action potential of the cells can be modelled as a reaction-diffusion system. The time domain derivative of the membrane potential V_m in the Courtemanch model is [16]

$$C_m \frac{dV_m}{dt} = I_{tm} + I_{stim} - I_{ion}, \quad (2.1)$$

where C_m is the membrane capacitance. I_{tm} , I_{stim} and I_{ion} are the transmembrane, stimulation and total ionic current, respectively. The total ionic current is a summation of the multiple ionic processes that take place in the cell's membrane. These modelled currents are [16]

$$I_{ion} = I_{Na} + I_{K1} + I_{to} + I_{Kur} + I_{Kr} + I_{Ks} + I_{Ca,L} + I_{p,Ca} + I_{NaK} + I_{NaCa} + I_{b,Na} + I_{b,Ca} \quad (2.2)$$

The ionic currents themselves are then dependent on the action potential, their specific equilibrium potentials and specific ion conductivities in the model. The transmembrane current I_{tm} can be calculated from the spatial difference in potential. The Courtemanch model with the electrical propagation included gives [16]

$$C_m \frac{dV_m}{dt} = S_v^{-1} \nabla \cdot \Sigma \nabla V_m + I_{stim} - I_{ion}, \quad (2.3)$$

where S_v is the cellular surface-to-volume ratio and Σ is the extracellular conductivity tensor. The term Σ then contains the directional conductivity information due to the anisotropic ratio and information about areas of lower conductivity in the tissue. The transmembrane current is thus

$$I_{tm} = S_v^{-1} \nabla \cdot \Sigma \nabla V_m. \quad (2.4)$$

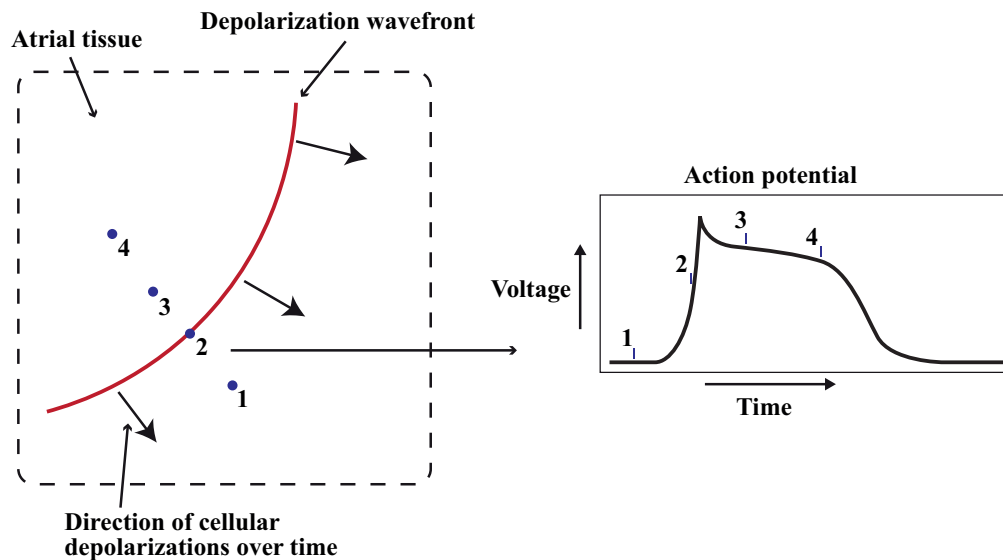


Figure 2.2: A 2-dimensional section of atrial tissue is shown on the left, with a depolarization wavefront indicated. The numbers 1 through 4 in the action potential plot on the right indicate locations on which the cells have a potential corresponding to different parts in of the standard atrial action potential.

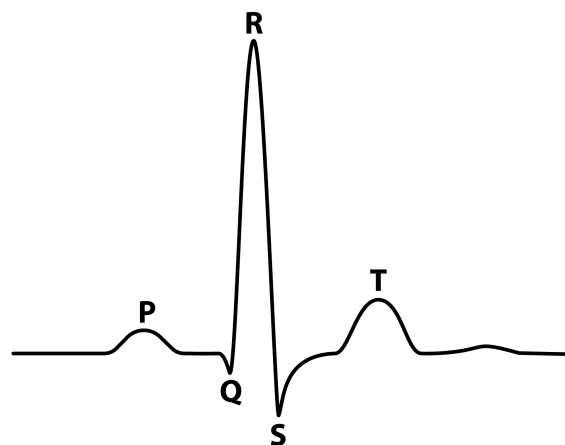


Figure 2.3: The shape of a normal surface ECG. The P-wave, QRS complex and T-wave are indicated.

Later, we will see that the transmembrane current is used to model the electrogram that would be measured when an electrode is brought near the cardiac tissue. The propagation of a wavefront of depolarizing cells is schematically shown on the left in Fig. 2.2. The action potential on the right that was mentioned previously, is shown there in a 2D part of atrial tissue in different locations, relative to a convex wavefront of propagating cell activations. The wavefront does not have to be convex, it depends on the conduction path taken.

2.1.3. The surface electrocardiogram

The surface electrocardiogram (ECG) is a representation of the electrical activity of the heart, recorded from the surface of the human body. It was first accurately measured with the string galvanometer by Willem Einthoven [6], [7]. Electrical leads were attached to limbs of a patient, and a current was measured and recorded. Before that, the capillary electrometer had been used by Einthoven to derive the shape of the signal, naming the P wave, QRS complex and T wave [17]. Subsequent discoveries resulted in the now common 12-lead ECG method [8] that uses 10 electrodes. An example of an ECG is shown in Fig. 2.3.

An ECG is normally shown with the vertical axis in (milli)volt and the horizontal axis in (milli)seconds. The P wave corresponds to the depolarization of the atria, the QRS complex to the depolarization of the ventricles and the T wave then to the repolarization of the ventricles. Repolarization of the atria is concealed by the QRS

complex.

2.2. Atrial Fibrillation

Atrial Fibrillation (AF) is the malfunctioning of the regular pattern of cell depolarizations in the atria, resulting in arrhythmic and chaotic contractions in the atrial muscle tissue. The condition was first described by Lewis in 1909 as auricular fibrillation [18]. It has been recognized as a common cardiac arrhythmia ever since [3].

The activations of the atria during AF are often chaotic, multiple activation wavelets travel through the atrium colliding and reexciting the tissue. Atrial flutter (AFL) is another condition that is characterized by high frequency contractions of the atrium in a less chaotic, more stable way. AFL can be a factor to let the atrial activations degenerate into AF [19].

2.2.1. Classification of AF

There are multiple systems to classify atrial fibrillation clinically based on different distinguishing properties [20]. The frequency of occurrence of episodes can be used to classify AF into *paroxysmal* (sudden/irregular episodes), *persistent* (continuous AF) or *permanent* (continuous and resisting treatment).

The designations paroxysmal, persistent and permanent have widespread use in diagnosis of AF as this is informative about the severity of the condition on a daily basis. This does not give information about the type or severity of AF during these episodes. Distinguishing between different types of AF on a beat-to-beat basis has not seen widespread use of a single classification system [20].

2.2.2. Mechanisms of AF

The mechanisms responsible for and governing the onset and perpetuation of AF are not completely understood [21]. One early theory about the mechanisms underlying AF is Moe's multiple wavelet hypothesis [22], which came about supported by a computer model [23]. This hypothesis proposes that above a certain number of wavelets traveling in the atrium, AF sustains itself. This does not specify the mechanisms that start AF in the first place.

Areas that block a wave or slow it down have been identified during AF [24], [25]. This could result in an activation wave "reentering" the atrium. These were not consistently present in the same area, but changed per activation period. Electric decoupling of side-to-side connections in parallel muscle fibers could explain the observed areas where conduction is blocked [26]. It was much more prevalent in patients with persistent AF than it was in patients with artificially induced AF.

With AF patients [27], spontaneous impulses (foci) that did not occur at the same location were observed. This could be attributed to an impulse from the endocardial layer in the atrium breaking through to the surface and causes a new impulse.

With paroxysmal AF a discrete source of disturbance was identified [28], coming from inside the pulmonary veins. A disruptive depolarization wave could originate there and disturb the regular contraction pattern of the atria. The earliest irregular activity in the pulmonary veins during could be detected 2 to 4 cm into the vein.

Another mechanism perpetuating AF, electrical "rotors", was known to be present in AF in animal testing [29]. These rotors are activation waves traveling in a circular motion and reexciting the tissue. They were shown to be present around an area of non-conducting tissue and thus had a stable center point. Wandering rotors were also observed, which had centers that moved [30]. Rotors do not appear constantly when the conditions would exist for them, but could need a certain trigger to start. They then could maintain AF for prolonged periods of time.

Current consensus The existence or absence of various mechanisms during AF is a difficult subject. It is still up to debate what mechanisms are exactly responsible for the maintenance of the reentrant waves during AF [5]. Both rotor and foci based AF have been simulated and activity indicating both their presences has been observed. However, no consensus has been reached about the mechanisms. It might be very difficult to pinpoint a single mechanism that initiates or sustains AF as it may vary per patient or per episode of AF, even in a single patient [21].

2.2.3. Treatment

Both pharmacological and electrical methods are available to treat certain forms of AF. Drugs may be used to control the ventricular rate and lower the heart rate to safe levels. Spontaneous onset of AF is often first

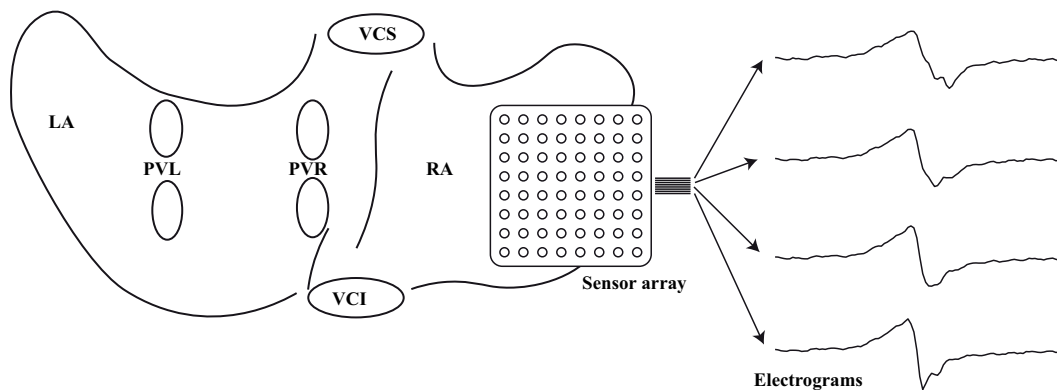


Figure 2.4: A schematic example of epicardial mapping of the atria. An example of an 8×8 array is shown being applied to a schematic map of the atria on the left, with the left atrium (LA), left and right pulmonary veins (PVL, PVR), superior and inferior vena cava (VCS, VCI) and right atrium (RA) indicated. Examples of measured signals are shown on the right.

treated with drugs. There are also drugs available for the maintenance of the normal sinus rhythm in patients with episodes of AF. These can be taken regularly or when an episode occurs [31].

Electrical or cryogenic ablation of AF is usually done by eliminating the origin of the disturbed signal or the tissue conducting it. Patients with paroxysmal AF caused by impulses originating in the pulmonary veins can be treated with this technique successfully [28]. Ablation of the tissue is then done with a catheter applying very high or low temperatures to the area around the pulmonary veins at the atria.

Ablation can also be used on other areas of the atria. For patients with persistent AF, just isolating the pulmonary veins may have limited success. During surgery, foci (often around connections to veins or appendages) can be sought and ablated. Linear ablation can also be applied to a certain part of the atria. These methods can prolong the periods between AF and terminate AF in patients with persistent AF [32].

From the limited (randomly controlled) studies available, it seems ablation of areas of irregular activity combined with pulmonary vein ablation is more successful than using the methods separately [5], [33].

2.3. Epicardial mapping

Although informative and non-invasive, the ECG is measured on a relatively large distance from the heart. The spatial resolution is therefore low, only showing spatially averaged behavior. A more invasive, but also more informative approach, is to use an array of electrodes positioned directly on the heart to obtain information about the depolarization occurring in the heart tissue. This can be used to directly *map* the activity. A schematic representation of this process can be seen in Fig. 2.4.

The mapping of the atrial activation patterns can give insight into the abnormalities in atrial conductivity and underlying mechanisms of AF [34]. Precise information about the time and location of electrical activity is valuable as it can shed more light on the conductive properties of the tissue. The mapping process can be split into two parts. The first is to acquire the epicardial electrograms using multiple electrodes in an array structure. The second is to estimate the activation pattern in the tissue from the recorded data. Methods used to map the atria are discussed here, methods to evaluate the measured signals will be discussed later.

Initial mapping studies [35], [36], [37] were done on canine and human hearts. In these studies, evidence was found of the existence of large reentry circuits and multiple simultaneous activations. This supported Moe's multiple wavelet hypothesis [22] for the sustaining of AF. The human atrium was also mapped with a higher resolution array, while rapid pacing was used to induce AF in patients with no history of the arrhythmia [24]. The higher resolution approach showed more complex patterns.

Lower resolution mapping systems [38], [39] (with electrodes placed further apart) were used to record both human atria concurrently and evaluate AF cycle lengths, as well as the rationale behind surgical intervention for AF. With this approach, surgical isolation of the pulmonary veins and cryogenic ablation along the atria were evaluated. A basket catheter was also used to map the inside of the left atrium at a low resolution [30]. In this mapping study it was concluded that both focal sources and rotors were present during human AF.

In patients with chronic AF, the right atrium was separately mapped [40]. Disorganized activations with multiple activation waves present at the same time were found there, as well as more organized activity in

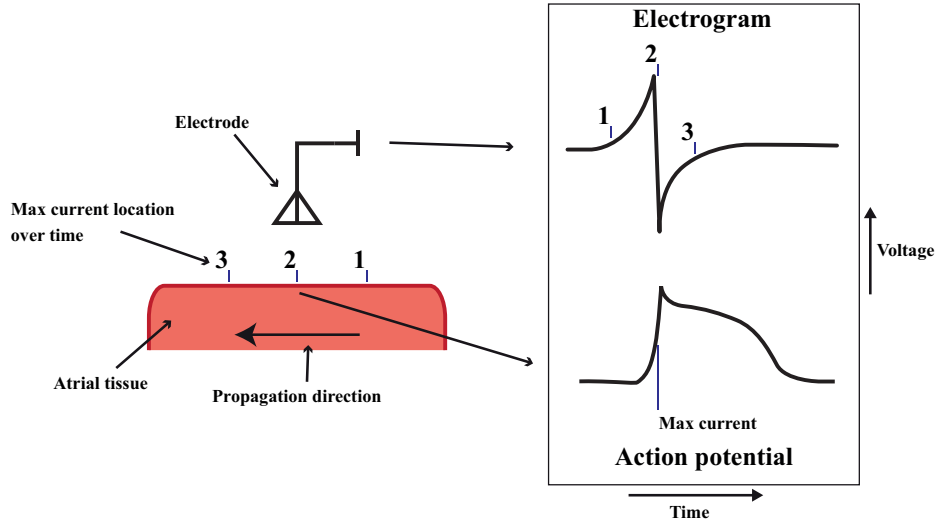


Figure 2.5: A side view is given for a piece of atrial tissue where the numbers 1 through 3 indicate different locations where the maximum current will be during propagation, and their corresponding location in a recorded electrogram. The action potential at location 2, directly under the electrode, is also shown.

other patients. It was impossible though to pinpoint if it was driven by reentrant or focal activity.

More recently a high resolution electrode array was used to record atrial activity during SR and during induced AF [9]. These mapping studies investigated areas of slow conduction or blockage of conduction in the atria [25]. These high resolution mapping studies were continued and used for the research presented in this thesis.

2.3.1. The epicardial electrogram

When electrodes are brought to the surface of the heart, they record the electrical activity in the tissue beneath them. An illustration of the atrial action potential propagating through tissue and generating an electrogram is given in Fig. 2.5. It can be observed that the propagating depolarization generates a signal which starts with a positive voltage which turns into a negative voltage as the point of maximum current passes underneath the electrode. For the atria, the model of the transmembrane current was given in Section 2.4.3. Using a current source approximation and assuming the extracellular conductivity σ_e is homogeneous and isotropic [41] the electrogram ϕ can be modelled as

$$\phi(\mathbf{y}, t) = \frac{1}{4\pi\sigma_e} \int \frac{I_{tm}(\mathbf{x}, t)}{\|\mathbf{y} - \mathbf{x}\|} d\mathbf{x}, \quad (2.5)$$

where \mathbf{x} is the location of the cells and \mathbf{y} is the electrode location. The result is a signal that depends on the activation (and as such on the transmembrane current I_{tm}) of a large area of cells, each with its own transmembrane current. The contribution of each cell to the overall electrogram depends on the distance $\|\mathbf{y} - \mathbf{x}\|$ between the cell and the electrode. The recorded electrogram is sometimes called a unipolar electrogram as it gives a potential with respect to a reference. Bipolar recordings are sometimes used, where the difference in potential between two electrodes is taken. In this thesis unipolar recording are considered.

2.4. Local activation times

In Fig. 2.2 an example of a section of atrial tissue was shown where the depolarization of the cells propagates through the tissue. It is the Local Activation Time (LAT) for a given location that is of particular interest. The LAT is the exact time at which the cells at one particular location (under an electrode for example) become active and depolarize. The LATs can be used to calculate the conduction velocity in the tissue and detect reentrant activity or multiple wavefronts propagating simultaneously. Low conduction velocity can indicate problems with conduction in the tissue and identifying abnormal wave paths can be of use in the treatment of AF.

When data is gathered with an epicardial electrode array, it is difficult to determine at what point in time the cells exactly underneath an electrode depolarize. The activation wave propagates through the tissue,

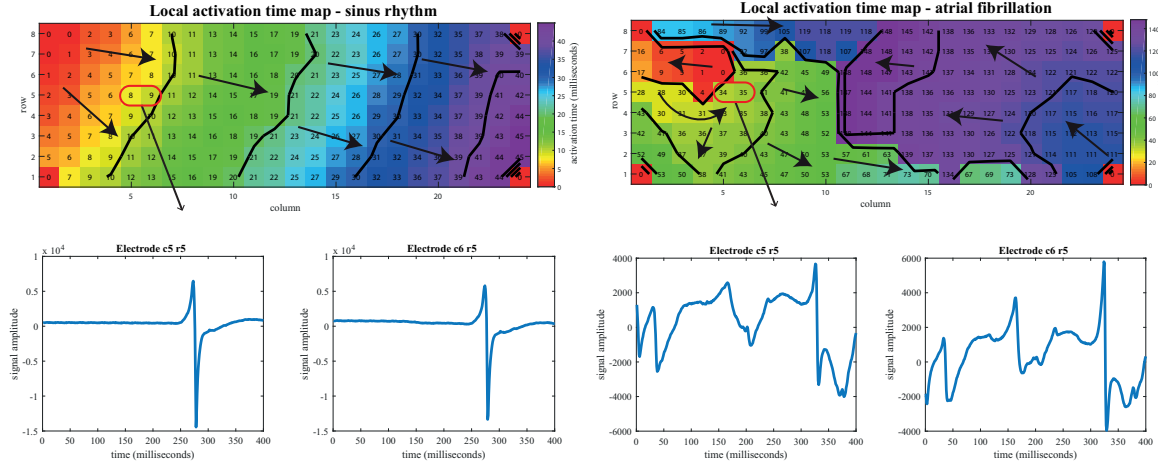


Figure 2.6: On the left an example is given of an estimated map of local activation times from a recording of regular sinus rhythm. On the right the same location is recorded on the same patient but with induced atrial fibrillation. Beneath each map the epicardial electrograms from two electrodes is shown. Black lines indicate isochrones in these maps and arrows indicate the estimate propagation paths.

which implies that the group of cells underneath the electrode do not all depolarize simultaneously.

Two examples of LAT maps are given in Fig. 2.6, with some of the underlying epicardial electrograms also shown. The maps show estimated LATs in milliseconds for a single beat of SR and for induced atrial fibrillation (IAF). The SR map shows a clear uniformly propagating wavefront and has electrograms showing a single activation wave propagating. The map for IAF shows multiple wavefronts and much more chaotic electrograms.

2.4.1. Local activation time estimation

From Eq. (2.5) it follows that the atrial electrogram ϕ is generated by the activation of a number of cells weighted by the distance to the electrode. The local transmembrane currents that make up this signal are not synchronized if the cells are not activated at the same time. The result is that the electrogram ϕ_i for electrode i , with $i \in 1, 2, \dots, M$ and M the number of electrodes, records a mixture of all of the activation times in the area.

The goal with the estimation of LATs is then to extract the true local activation time τ_i of the electrode location, from the electrogram ϕ_i . Because the electrogram is a signal that is comprised of the contributions from cells with different activation times, this is not trivial.

Several techniques have been proposed to extract LATs for each electrode or for any part of the mapped area [42]. Apart from the automated methods of LAT estimation it can also be done manually by physicians. The accuracy of this manual annotation is difficult to determine as the methods of interpretation vary from expert to expert. The most widely used automated methods will be explained in this section.

2.4.2. Steepest (Negative) deflection

When measuring unipolar electrograms, the steepest negative deflection (point of maximum negative derivative) was reported to correspond well to the activation time [10], [43]. This steepest deflection (SD) has a physical relation to the processes in the cells as it relates to the moment of maximum rate of increase of the sodium current [44]. The activation time of electrode i is calculated by the minimum of the time derivative

$$\tau_i = \operatorname{argmin}_t \frac{d\phi_i(t)}{dt} \quad (2.6)$$

where $\phi_i(t)$ is the epicardially measured signal from electrode i and τ_i is the LAT. In practice, $\phi_i(t)$ is only available at discrete moments in time as it is sampled during the measurement. The LAT of the discrete time signal $x_i(k)$ is then

$$\tau_i = \operatorname{argmin}_k \phi_i(k) - \phi_i(k-1). \quad (2.7)$$

This method has as a disadvantage that it evaluates each electrode signal individually, the data from the surrounding electrodes is not taken into account. Using purely the derivative of the measured signal to estimate

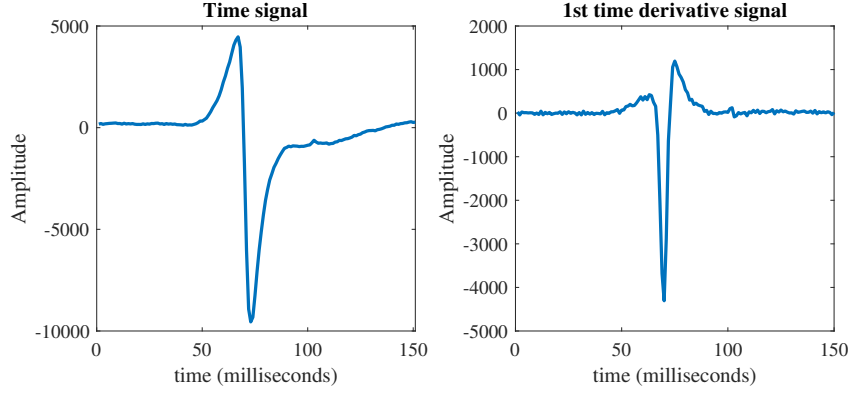


Figure 2.7: On the left an example of an epicardial electrogram measured on the human atrium is shown. On the right the derivative of this signal is shown.

the LAT makes is susceptible to spikes added by measurement noise and other noise sources. An example of the regular atrial electrogram and its derivative is shown in Fig. 2.7. The relation between the derivative and the action potential has shown to be powerful on a microscopic scale when evaluating the depolarization of the cells, however using it on a much larger scale, such as in epicardial mapping of the atria, makes the recorded signal subject to "distant active membrane" [45]. A larger area of tissue is influencing the electrogram and the derivative may not be a perfect method to obtain information about the depolarization of the local cells.

2.4.3. Cross-correlation

The cross-correlation of a signal is an excellent method to find a delay between two signals if the signals are rather similar, except for a time shift, and are thus highly correlated. If the signals differ in morphology, however, the resulting lag might not be accurate. Existing cross-correlation methods use only the closest neighboring electrodes to create pairs for which delays are calculated [46]. The resulting delays between the electrodes then do need to be converted to absolute times.

The data used to cross-correlate is taken from data vector $\mathbf{x}(k) = [x_1(k), x_2(k), \dots, x_M(k)]^T$, where $x_i(k)$ can be the electrogram or its derivative (of which an example was shown in Fig. 2.7), and $k \in 1, 2, \dots, K$ where K is the number of samples in the data. The normalized cross-correlation (NCC) function $\rho_{i,j}$ of electrode i and j , where $i, j \in 1, 2, \dots, M$ is then calculated as a function of the shift in samples s as

$$\rho_{(i,j)}(s) = \frac{1}{N} \frac{\sum_k (x_i(k) - \mu_i)(x_j(k-s) - \mu_j)}{\sqrt{\sigma_i^2 \sigma_j^2}}. \quad (2.8)$$

The means μ_i, μ_j of the signals from electrode i and j are subtracted and their variances σ_i^2, σ_j^2 are used for normalization, resulting in values between $[-1, +1]$. For $s \neq 0$ the two signals do not completely overlap, so they are zero-padded to make them of equal length.

All the electrodes are then to be cross-correlated with their neighboring electrodes, if electrode j is a neighbor of i it is denoted as $j \in N(i)$. The lag between electrode i and j , $\hat{\Delta}_{(i,j)}$, is then estimated as

$$\text{for } j \in N(i), \quad \hat{\Delta}_{(i,j)} = \underset{s}{\operatorname{argmax}} \rho_{(i,j)}(s). \quad (2.9)$$

The estimated delays $\hat{\Delta}$ between pairs of neighboring signals then have to be converted to LATs for each electrode [46]. Higher time resolution can be obtained by using the Hilbert transform of the cross-correlation [11]. Using a (weighted) combination of the maximum negative slope and a cross-correlation estimate can also potentially improve the result [47].

2.4.4. Deconvolution

A convolution is a mathematical operation defined as

$$(f * h)(t) = \int_{-\infty}^{\infty} f(\tau)h(t - \tau)d\tau = g(t). \quad (2.10)$$

The functions $f(t)$ and $h(t)$ can be input and system response functions.

Deconvolution is then used to try and reverse this process. As this is usually an ill-posed problem some prior knowledge is needed about the functions that are convolved. For example, if an estimate of one of the functions, $\hat{h}(t)$, is available it can be used. A cost function can be minimized to estimate the other function $f(t)$ as

$$\operatorname{argmin}_f \|g(t) - (f * \hat{h})(t)\|. \quad (2.11)$$

The difficulty comes from obtaining this accurate prior knowledge about the system and also realizing there might be noise and other disturbances present in the measured data.

In the context of epicardial mapping, the convolution is relevant as the measured signal from a electrode can be seen as a convolution of an input signal with the system response of the cardiac tissue. The model for the epicardial electrogram Eq. (2.5) can be seen as having the properties of a convolution. Deconvolution methods in epicardial mapping can then be applied to try and recover the system response (the different conductivities in the tissue) or estimate the input signal and its timing (the LATs).

A deconvolution method was used to estimate the activation time from a single electrogram [48]. The model used to obtain a system response to use in deconvolution was that of a constant velocity activation wave traveling through tissue.

A spatial deconvolution method was also applied to estimate current in the tissue and LATs together with a wavelet filtering approach [49]. This deconvolution method did not assume constant velocity but a known spatial kernel for the recorded signals.

Abdi et al. (2019) [50] proposed a simplified model for the conduction in the atria. From the model of the conduction maps, an inverse problem was formulated to estimate the tissue conductivity.

2.4.5. Spatial gradient

Another method to estimate the LAT is to use the spatial gradient (SG) of the data [51], which exploits the high spatial current density during the propagation an activation wave. The spatial gradient of the electrograms $\nabla\Phi$ in two dimensions (\hat{i} and \hat{j} represent unit vectors in these dimensions) is used, which is

$$\nabla\Phi = \frac{d\Phi}{d\hat{i}} + \frac{d\Phi}{d\hat{j}}. \quad (2.12)$$

To implement this, a central difference method is used that calculates the spatial gradient $\nabla\phi_i(k)$ for each electrode i using the four neighboring electrodes. The LAT is then determined from the maximum magnitude of this spatial gradient

$$\tau_i = \operatorname{argmax}_k \|\nabla\phi_i(k)\|, \quad (2.13)$$

where τ_i is the estimated LAT for electrodes i and $\nabla\phi_i(k)$ is the spatial gradient at sample k for that electrode.

2.4.6. Template matching

Electrograms recordings can also be matched to a library of templates. How these templates are gathered or defined and how they are matched varies between methods.

A single recording from an electrode can be taken and used as a template for subsequent electrodes. This was done for ventricular data and the templates were adaptively updated during the matching, trying to minimize the mean-square error [52].

Template matching was also done specifically for AF to map activation waves traveling through the fibrillating tissue [53]. This method used the normalized cross-correlation to estimate the activation time and obtain a correlation coefficient, similar to the method described in Section 2.4.3.

3

Simulated and recorded atrial electrogram data

In the research used in this thesis we use both natural and simulated data. In this chapter the methods for data acquisition (for natural data) and data generation (for simulated data) are explained.

In Section 3.1 we first discuss the simulation of a 2D surface of atrial tissue. Multiple scenarios of different tissue conditions have been generated. This is a valuable tool as the ground truth of the activation times is available together with the electrograms that would be measured by an electrode.

In Section 3.2 we describe the clinically recorded natural data. It was recorded at Erasmus MC (Rotterdam, the Netherlands) using the methods described in [9]. This natural data consists of epicardial electrograms of the human atria recorded with an array of electrodes.

3.1. Simulated data

3.1.1. Simulation

In this study, we used the approach described in [50] to generate simulated electrograms. It is based on the monodomain reaction-diffusion model of the atrial action potential [54] together with the Courtemache model of the human atrial myocytes [16].

The simulated electrograms can be generated based on the transmembrane currents, available in the monodomain formulation [41]. Based on the compact model for atrial electrograms [50], the simulated electrogram $\Phi_m(t)$ is then computed as

$$\phi_m(t) = \frac{1}{4\pi\sigma_e} \sum_{n=1}^{N_c} \frac{I_{tm}(\mathbf{x}_n, t)}{r_{m,n}} \Delta x^2, \quad (3.1)$$

where the I_{tm} is the transmembrane current at time t , at position \mathbf{x}_n , with n the cell index with $n \in 1, 2, \dots, N_c$. The total number of cells is N_c and $m \in 1, 2, \dots, M$ is the electrode index. The cells are assumed to be on a 2D uniform square grid with a spacing Δx . The assumption is that the electrode array is located on a plane parallel to the plane of the cells, at a height of z_0 . The distance $r_{m,n}$ of a cell to an electrode is then $r_{m,n} = \sqrt{z_0^2 + \|\mathbf{x}_n^2 - \mathbf{y}_m^2\|}$, where \mathbf{y}_m is the location of the electrode on its plane.

The simulations are started by instigating the propagation from a specified cell. A stimulating current is simulated at the start to depolarize the first cells. In the simulations shown in this thesis, this will always be at the bottom-left corner of the simulated tissue.

3.1.2. Data sets

Multiple data sets have been generated using the aforementioned simulation. For each data set a square grid of 11×11 electrodes was simulated with an inter-electrode distance of 2 mm. This electrode array was centered on an area of cells with an inter-cell distance Δx of 2/3 mm. The distance of the array to the tissue z_0 was set to 0.1 mm. The figures that are shown only show the simulated conductivity under the electrode array, the patterns do extend beyond this visible area (to 89×89 cells in total), to generate accurate signals.

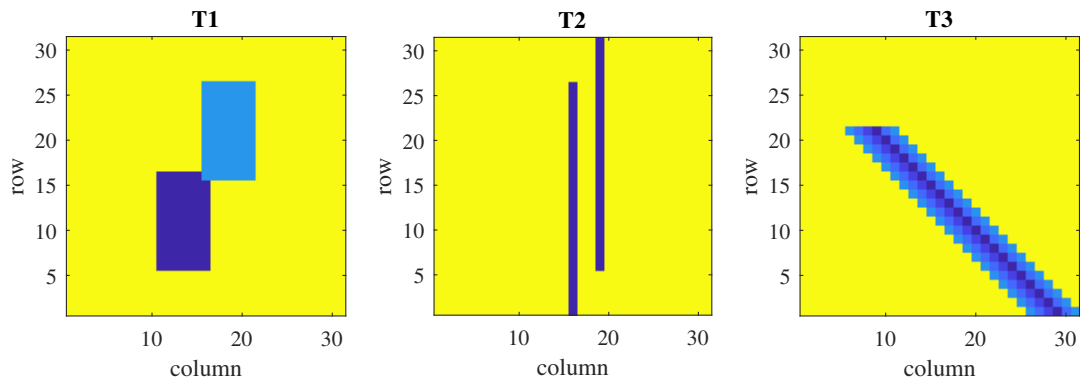


Figure 3.1: The conductivity maps for simulating specific shapes of blocks in the tissue.

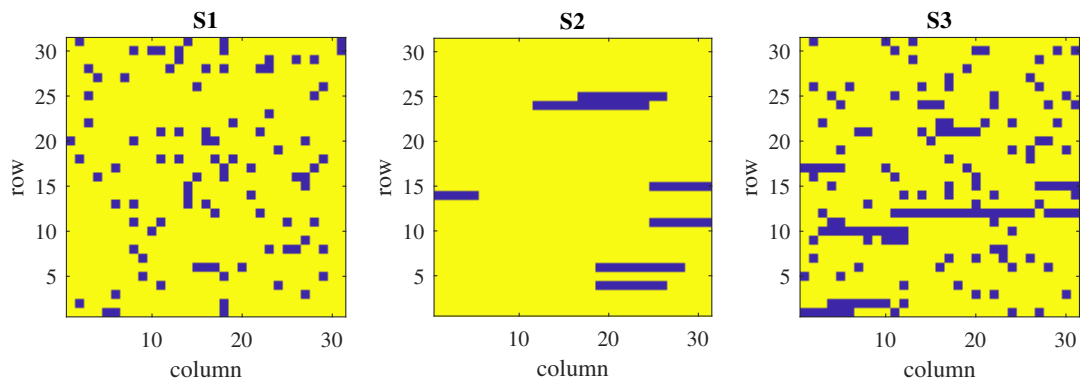


Figure 3.2: Examples of the conductivity maps generated for the different types of fibrosis tissue simulations.

The simulation was ran with a time step size of 0.02 ms. It was then downsampled to 1 ms to match the 1000 Hz sample rate of the clinical data.

For evaluation of LAT estimation methods in this thesis, two categories of data sets were created: Artificial blocking shapes and fibrosis tissue simulations.

Artificial blocking shapes A set of three simulations was done with specific patterns of blocking or slow conduction. Their conductivity maps are shown in Fig. 3.1. Simulation **T1**, **T2** and **T3** are less realistic, but used to exaggerate differences between the methods of LAT estimation.

Fibrosis tissue Three more realistic types of patterns were also simulated and shown in Fig. 3.2. These are examples of the different patterns that mimic decoupling of conduction between areas of atrial tissue [26]. This can be caused by excessive deposition of collagen due to fibrosis in the heart. There is simulation **S1** with spots of no conduction, **S2** with lines of no conduction and **S3**, a combination of both. Multiple realization of these types can be generated to test consistent performance in the methods.

3.1.3. Example of simulated electrograms

In this section the conduction pattern of **T2** will be used to demonstrate the simulation of the electrograms. In Fig. 3.3 the LATs for each of the electrodes in the 11×11 simulated array are shown, shifted in time so the first LAT is at 0 ms. These LATs will be used as a ground truth to compare the estimated LATs to.

The underlying simulation uses cells that activate and generate transmembrane current, as was explained in Section 3.1.1. The true activation times of the cells themselves are shown in Fig. 3.4. Four locations of electrodes are highlighted. They are on row 7, column number 5 to 8.

The highlighted electrodes do not only detect the signal from the point directly under them. The electrogram is a signal influenced by all the cell currents in the area, which was explained in Section 2.3.1. The signals simulated from the highlighted electrodes is shown in Fig. 3.5. The multiple excitations shown by the simulated electrograms can be related to the path the wave takes in this simulation.

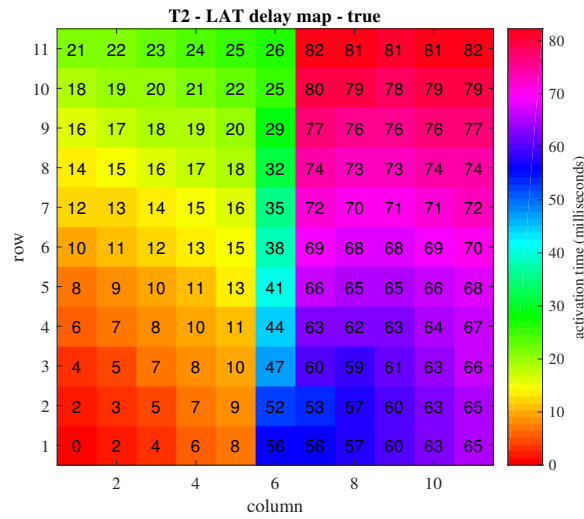


Figure 3.3: The true activation times in milliseconds for each of the simulated electrodes for simulation T2 is shown. They are aligned so the first electrode's activation time is at 0 ms.

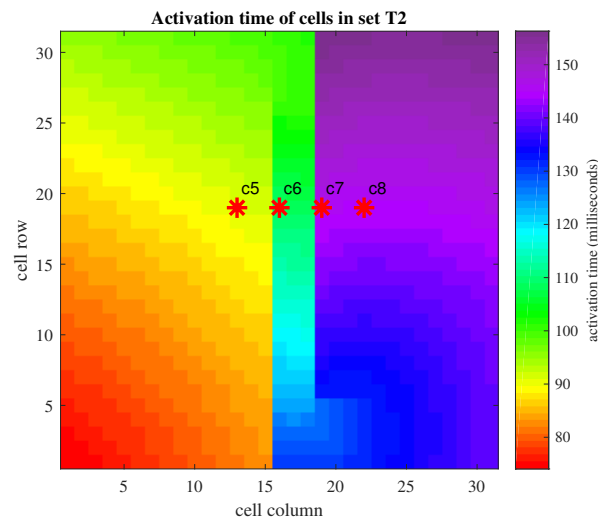


Figure 3.4: For the 31×31 cells beneath the electrodes array of T2 the true activation times are shown. The location of four electrodes in row 7 of the array are highlighted with a red *.

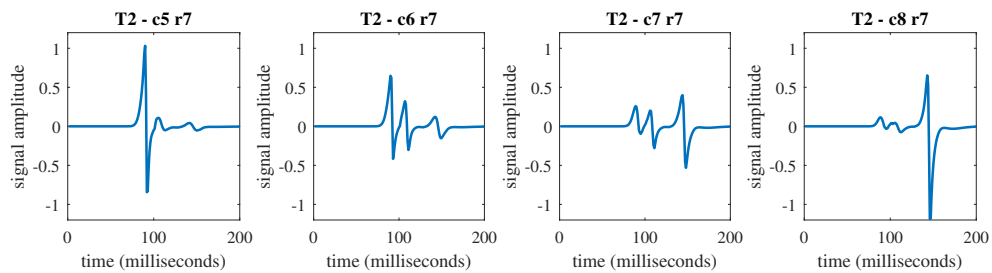


Figure 3.5: The recorded signals from the four highlighted electrodes from Fig. 3.4 are shown.

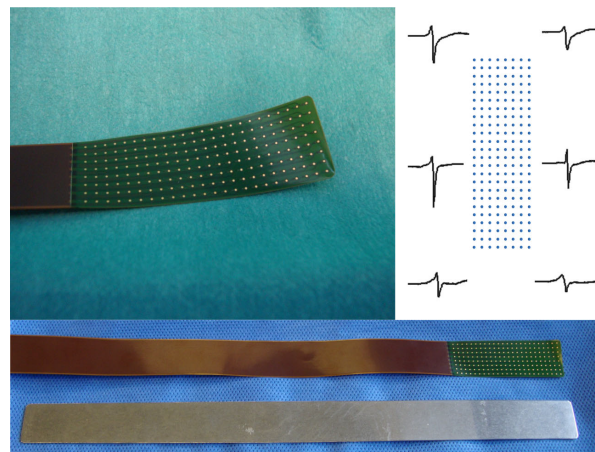


Figure 3.6: The electrode array used in obtaining the real-world data sets. (source: [9])

3.2. Real-world data

The method for gathering natural data in a clinical setting used for this thesis is described in [9]. An electrode array was used to obtain data from different recording sites on the surface of the human left and right atria. The electrode array is shown in Fig. 3.6. It is comprised of a flexible printed circuit board with the 192 contact points. The recording was done during open heart surgery. The array was manually placed on the different locations on the atria, by hand or with a metal spatula also shown in the bottom part of Fig. 3.6.

3.2.1. Data format

The electrode array used for measurements consisted of 8×24 electrodes with 2 mm of spacing resulting in 192 signal channels. Four electrodes are not used for epicardial measurements, but serve other purposes. These are the electrodes on the corners of the array. One of channels of a corner electrode is used to measure the surface ECG. The other three corner signals are not used. The data is stored row after row in one vector per time sample. The data was preprocessed before it was stored. It was amplified with a gain of 1000, bandpass filtered (0.5-400 Hz), sampled at 1 kHz and quantized with 16 bits.

3.2.2. Data acquisition

The real-world, natural data that is used in this thesis was recorded at Erasmus MC in Rotterdam, the Netherlands using the methods described first in [9]. Hundreds of data sets from patients have been recorded there. The patients were undergoing cardiac surgery for coronary and/or structural heart disease. Patients were 18 years old and older, with and without histories of AF.

At different recording sites on the atria mapping was performed. The recording sites are shown in Fig. 3.7. The recordings sites were on the Left Atrium (LA, LAV), between the Pulmonary Veins (PVL, PVR), on Bachmann's bundle (BB) and on the right atrium (RA). At each location 5 seconds of SR and 10 seconds of AF was recorded. To induce AF rapid pacing using electric stimuli was done. In this thesis the focus will only be on the SR data.

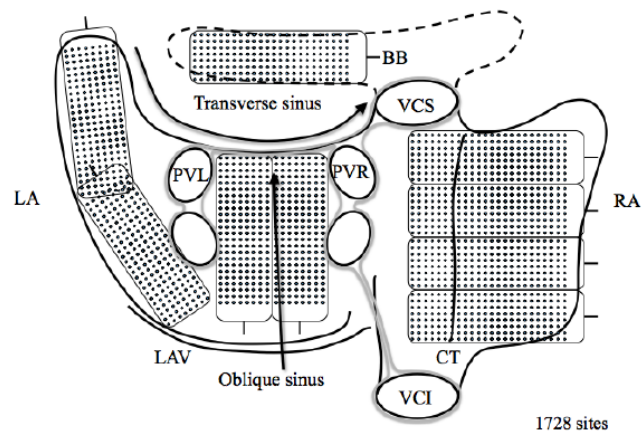


Figure 3.7: The different locations used for recording atrial activity shown on a folded-out illustration of the atria.

4

LAT estimation using cross-correlation estimation over higher order neighbors

In this chapter, the proposed method for LAT estimation is presented, which uses the cross-correlation to determine the delay between electrodes in an electrode array, based a framework that defines higher order neighbors in the array. Additional steps are then discussed to obtain absolute time estimates from the delays.

In Section 4.1, a representation of the atrial electrograms is shown where the signal from an electrode is modelled as a scaled and shifted version of a standard signal of an activation wave propagating in the atria. In Section 4.2 a grid graph is used to define the connectivity between neighboring electrodes. This is then used to define the connections between pairs of electrodes when higher order neighbors in that graph are evaluated. In Section 4.3, cross-correlation is discussed for estimation of delays in time for higher order neighbors. Subsequently, in Section 4.4 a least squares approach to estimate the LATs from the delays obtained using cross-correlation is discussed. Finally, in Section 4.5 it is explained how a section of data is segmented and compared, to observe the performance of LAT estimation methods.

4.1. The atrial epicardial electrogram as separate excitation waves

In Section 2.3.1, the model for the atrial electrogram as it would be measured on the heart's surface was presented. The model for the electrogram ϕ_i of electrode i , with $i \in 1, 2, \dots, M$, was shown to be generated by the transmembrane currents. The model for the transmembrane currents described in Section 2.1.2 was shown to depend on the tissue conductivity.

Let us then assume a tissue surface is measured with a homogeneous conductivity and let us ignore differences in curvature of an activation wavefront. The measured electrogram $\phi_i(k)$ can then be modelled as a scaled and shifted version of the standard electrogram response from the tissue $\phi_0(k)$. The standard electrogram $\phi_0(k)$ is assumed to be a "regular" electrogram for an activation wave traveling through homogeneous tissue below an electrode. A measured electrogram can then be modelled as

$$\phi_i(k) \approx \alpha_i \phi_0(k - \tau_i) + n_i(k) \quad (4.1)$$

where α_i is a scalar determining the amplitude, τ_i is the time shift with which the signal is measured, and $n_i(k)$ is noise from the measurement. Under these assumptions, different electrodes show comparable signals as they are scaled and shifted reference responses. The response from another electrode j will then be

$$\phi_j(k) \approx a_{(i,j)} \phi_i(k - \Delta_{(i,j)}) + n(k) \quad (4.2)$$

where $a_{(i,j)}$ is another scaling term, $\Delta_{(i,j)}$ is the difference in activation time between the two electrodes and $n(k)$ is assumed to be uncorrelated noise. The electrograms would then be scaled and shifted versions of each other.

When there are sections of tissue that do not conduct, multiple separate activations may be detected spread out in time. This can then be modelled as

$$\phi_i(k) \approx \alpha_i \phi_0(k - \tau_i) + \left(\sum_w \beta_w \phi_0(k - \tau_w) \right) + n(k) \quad (4.3)$$

where the disturbances can then be seen as additional activations at times τ_w with a scaling β_w . An example of this structure appearing in the measured signal was given in Section 3.1.3 where the multiple waves are visible in the electrode signals. These additional activation might be present in one electrode signal at different time shifts than in another electrode signal, resulting in Eq. (4.2) being less accurate. When cross-correlation is applied to a pair of electrodes i and j , it is important to keep in mind that the disturbances at times τ_w from electrode i can also correlate with the activations present in electrode j , influencing the resulting cross-correlation values.

4.2. Spatial structure of the data

The array consists of multiple electrodes arranged in a certain pattern, providing spatial information. This spatial information can and should be somehow exploited to achieve better estimates of the electrical activity in the atria. The connections between the electrodes will be represented as a graph. A connection represents that these electrodes are *neighbors* and should have some spatio-temporal relation.

4.2.1. Graphs

A graph \mathcal{G} is defined as a vertex (node) set \mathcal{V} and an edge (link) set \mathcal{E} , so $\mathcal{G} = (\mathcal{V}, \mathcal{E})$. The graph's structure is then a set of nodes connected by links. The links define a spatial structure, indicating some interaction is possible between the connected nodes. In this section, we assume the size of the vertex set is M (there are M nodes) and the size of the edge set is L (there are L links).

A graph with non-directional links between nodes is called an *undirected* graph. When the links between nodes have directions associated with them, implying some kind of one-way connection between the nodes, they are called *directed* graphs. Links can also have a number or weight attached to them. They are then called *weighted* graphs. These weights can indicate some metric like distance, delay, bandwidth, etc. Examples of these types of graphs are shown in Fig. 4.1.

An *adjacency matrix*, say $\mathbf{A} \in \mathbb{R}^{M \times M}$, is a way to structure the information about the graph connections. If there is no edge between node i and node j in either direction then $A_{i,j} = A_{j,i} = 0$. If there is an edge from node i to node j , $A_{i,j}$ has some non-zero value. An adjacency matrix of an undirected graph, which is shown on the left in Fig. 4.1, would be

$$\mathbf{A}_{undirected} = \begin{bmatrix} 0 & 1 & 1 & 1 & 1 \\ 1 & 0 & 0 & 0 & 1 \\ 1 & 0 & 0 & 1 & 0 \\ 1 & 0 & 1 & 0 & 1 \\ 1 & 1 & 0 & 1 & 0 \end{bmatrix}. \quad (4.4)$$

This is a symmetrical matrix, because the graph is undirected, with 1's indicating the links. The adjacency matrix of a directed graph, shown in the middle in Fig. 4.1, would look like

$$\mathbf{A}_{directed} = \begin{bmatrix} 0 & 1 & 1 & 1 & 0 \\ 0 & 0 & 0 & 0 & 1 \\ 0 & 0 & 0 & 1 & 0 \\ 0 & 0 & 1 & 0 & 0 \\ 1 & 0 & 0 & 1 & 0 \end{bmatrix}. \quad (4.5)$$

Here the matrix is not symmetric anymore as there are one-way connections between nodes. Two way connection can still exist, they are then interpreted as two opposing one-way connections. Weights can also be added to the adjacency matrix. The weighted directed graph shown on the right in Fig. 4.1 would then be

$$\mathbf{A}_{weighted} = \begin{bmatrix} 0 & 2 & 2 & 4 & 0 \\ 0 & 0 & 0 & 0 & 3 \\ 0 & 0 & 0 & 1 & 0 \\ 0 & 0 & 3 & 0 & 0 \\ 1 & 0 & 0 & 2 & 0 \end{bmatrix} \quad (4.6)$$

where the weights are shown instead of the 1's for a connection.

Another method to describe the edges present in a graph is the *incidence matrix*, here called \mathbf{B} . This matrix has a size of $M \times L$. The rows then correspond to the nodes and every column corresponds to an edge.

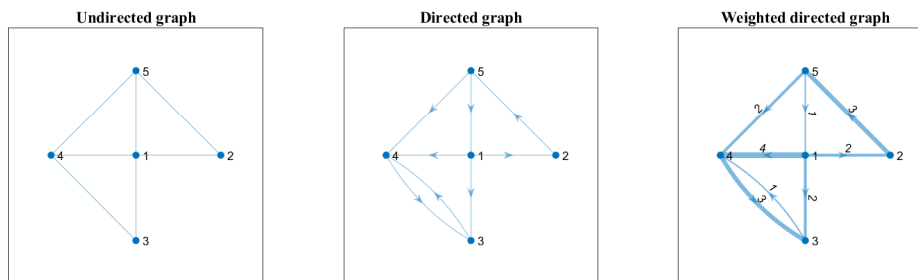


Figure 4.1: Examples of different types of graphs. From left to right an undirected, a directed and a weighted directed graph is shown.

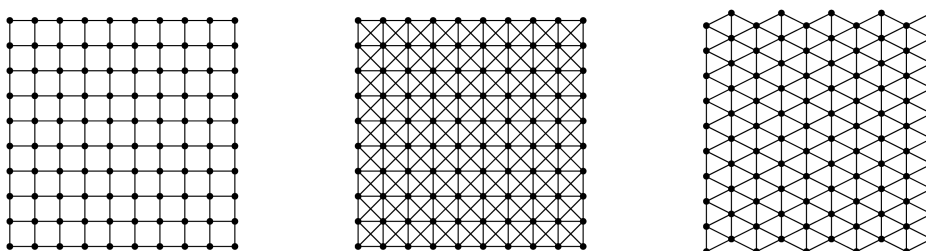


Figure 4.2: Different types of grid graphs. From left to right the square grid graph, the square grid with diagonal connections and the triangular grid graph are shown.

For a directed graph, in each column there is a -1 placed at the node from which the edge departs and a 1 at a node where the edge arrives. The incidence matrix of the directed graph shown previously in Fig. 4.1 would be

$$\mathbf{B}_{directed} = \begin{bmatrix} -1 & -1 & -1 & 0 & 0 & 0 & 1 & 0 \\ 1 & 0 & 0 & -1 & 0 & 0 & 0 & 0 \\ 0 & 1 & 0 & 0 & -1 & 1 & 0 & 0 \\ 0 & 0 & 1 & 0 & 1 & -1 & 0 & 1 \\ 0 & 0 & 0 & 1 & 0 & 0 & -1 & -1 \end{bmatrix}. \quad (4.7)$$

The adjacency and incidence matrices will be used in this section to indicate which electrode pairs have a link between them. The combined data from the pairs that have such a connection will then be used, and the electrodes that are paired can be varied to see differences in the performance of the LAT estimation.

4.2.2. Grid graphs

Grid graphs, or lattice graphs, are suited to represent the connections in the data as the electrode array is also a regularly spaced grid. The simulated and clinical data for this thesis is gathered by an array of electrodes in a two-dimensional grid. Some examples of two-dimensional grid graphs are given in Fig. 4.2.

For the electrode array that was used to gather data, a square grid graph is adopted. This graph is shown in Fig. 4.3 for the entire array. The 192 electrodes present are shown as nodes and their connections in the square grid pattern can be observed. For demonstrative purposes a 8×8 graph is created and shown in Fig. 4.4. This has the same square grid as the electrode array graph shown in Fig. 4.3 and will be used to explain concepts more easily in the next section.

4.2.3. Higher order neighbors in the electrode array

The square electrode grid that was defined is then described by adjacency matrix \mathbf{A} . This contains information about the electrodes and their neighbors as was explained before. It is constructed for electrodes i and

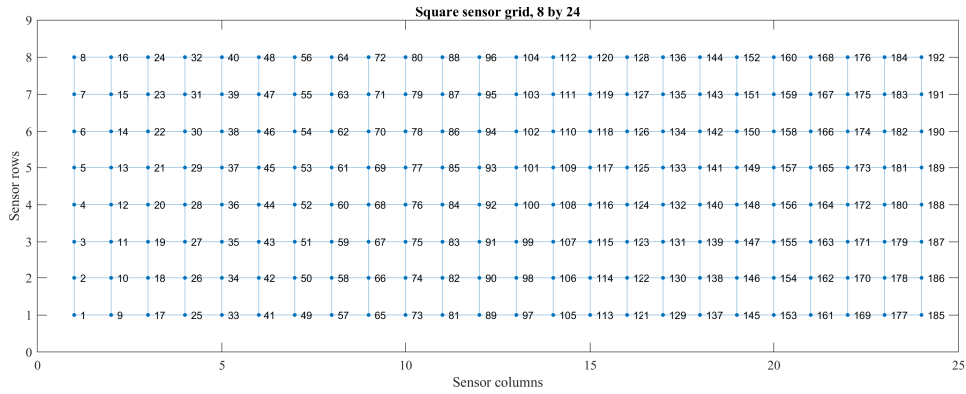


Figure 4.3: The 24×8 electrode array is shown with the electrodes indices denoted. The array is connected in a square grid.

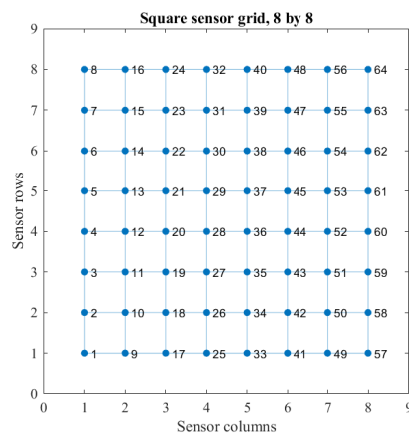


Figure 4.4: An 8×8 array is shown with the electrodes indices denoted. The array is connected in a square grid and will be used as an example.

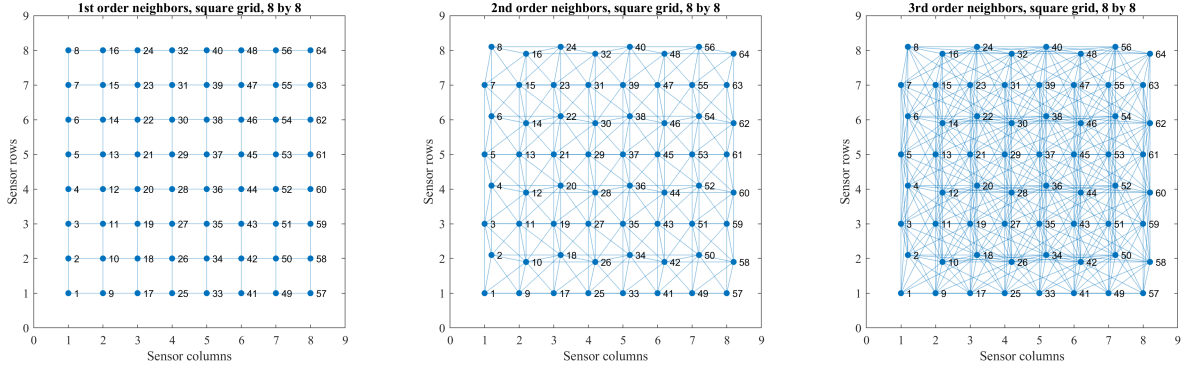


Figure 4.5: An 8×8 array is shown with the electrodes indices denoted. The square grid is used as a basis. From left to right the first, second and third order neighbor are connected. So from left to right $\Xi^{(1)}$, $\Xi^{(2)}$ and $\Xi^{(3)}$ are shown.

j , where $i, j \in 1, 2, \dots, M$, as

$$A_{i,j} = \begin{cases} 1 & \text{if } j \in N(i) \\ 0 & \text{otherwise} \end{cases} \quad (4.8)$$

where $N(i)$ are the neighboring electrodes of i in the square grid, so the neighbors of electrode number 28 in Fig. 4.4 for example are electrodes 20, 27, 29 and 36.

Another adjacency matrix Ξ is defined to indicate connectivity between electrodes that will be used in the LAT estimation method introduced later. Matrix A only has the connections from neighboring electrodes, or one *hop* away in the grid graph. For a graph where the nodes are connected over P hops of the template grid, the connectivity graph adjacency matrix $\Xi^{(P)}$ is defined as

$$\Xi^{(P)} = \sum_{p=1}^P A^p. \quad (4.9)$$

The order P of $\Xi^{(P)}$ thus determines over what distances the nodes are connected by edges. The entries in the connectivity graph adjacency matrix $\Xi^{(P)}$ can have values > 1 for $P > 1$, this is not an issue as we later only check if a value > 0 is present or not. An example of increasing P is shown in Fig. 4.5. The 8×8 graph is shown there for $P = 1, 2, 3$. At $P = 1$ the graph is just the square grid graph. At $P = 2$ each node is connected with nodes 2 hops away in the square graph,. The diagonal connections are present as a result, as are the connections 2 inter-electrode distances away in the column and row direction. At $P = 3$ the connections 3 hops away are all shown and it can be seen the network becomes even more interwoven.

In Fig. 4.6 the same graph is shown, but only the connections originating in node number 28. This shows the patterns from the perspective of a single electrode for increasing P . The parameter P and the connectivity matrix $\Xi^{(P)}$ can now be used as a framework to determine which nodes are connected. The connectivity of the electrodes then determines which electrograms will be correlated, which will be explained in the next section.

4.3. Cross-correlation over higher order neighbors

Where previously the cross-correlation would be used to calculate lags between only neighboring electrodes, it can also used to calculate the lags between nodes further away. The reasoning for only cross-correlating the electrodes that are closest to each other could be that these correlate well, while the electrodes become less correlated over longer distances and the estimated lags would be less informative. An illustration to show the effect of using higher order neighbors to estimate LATs from the time delays is given in Fig. 4.7.

In this thesis, the performance benefit of cross-correlating nodes that are further away will be evaluated. The normalized cross-correlation will be reformulated to determine the inter-electrode lags for a set of pairs, dependent on P . A data vector $\mathbf{x}(k)$ of size M (the total amount of electrodes) is used. This is then the time-series data of the electrograms $\phi(k)$ or the derivative of the electrograms,

$$\mathbf{x}(k) = \phi(k) \quad \text{or} \quad \mathbf{x}(k) = \frac{\phi(k) - \phi(k-1)}{T_s} \quad (4.10)$$



Figure 4.6: An 8×8 array is shown with the electrodes indices denoted. Here only the connections are shown for electrodes number 28 with a square grid basis. From left to right the first, second and third order neighbor are connected. So from left to right $\Xi^{(1)}$, $\Xi^{(2)}$ and $\Xi^{(3)}$ are shown when looking at the links originating from electrode 28.

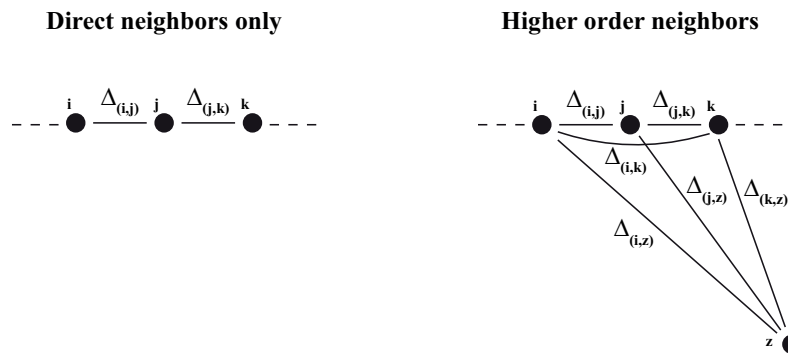


Figure 4.7: A schematic example is given of the differences between only using directly neighboring nodes (link (i, j) and link (j, k)) to calculate delays (Δ) in time, and using higher order neighbors. Pairs of nodes are connected over much larger distances in the array, an example of such a far away node (node z) is shown on the right side. The delays calculated over these distances are used as extra information in the LAT estimation process.

where T_s is the sample time. The normalized cross correlation $\rho_{(i,j)}(s)$ for electrodes $i, j \in 1, 2, \dots, M$ as a function of the shift in samples between two signals s is then calculated as

$$\rho_{(i,j)}(s) = \frac{1}{N} \frac{\sum_k (x_i(k) - \mu_i)(x_j(k-s) - \mu_j)}{\sqrt{\sigma_i^2 \sigma_j^2}} \quad (4.11)$$

where μ_i, μ_j are the means and σ_i^2, σ_j^2 are the variances of $x_i(k)$ and $x_j(k)$. All the electrode pairs up to P hops apart in this graph are then to be cross-correlated. The lag between electrode i and j , $\hat{\Delta}_{i,j}$, is then estimated as

$$\text{for } \Xi_{i,j}^{(P)} \neq 0, \quad \hat{\Delta}_{i,j} = \arg \max_s \rho_{(i,j)}(s). \quad (4.12)$$

The resulting lags can be put in a matrix \mathbf{D} of size $M \times M$ where element i, j is the lag between the corresponding electrodes. This matrix can then be seen as a weighed adjacency matrix for a graph containing the delay information. This graph contains the same links and nodes as $\Xi^{(P)}$. If a delay of 0 ms is found between two electrodes, a minuscule value might need to be added during processing, as a 0 in \mathbf{D} indicates no connection present.

4.3.1. Relation of cross-correlation to maximum likelihood

In Section 4.1 it was proposed that the electrograms from different electrodes can be approximately modelled as shifted versions of each other. Assuming this is now the true case, the data used for cross correlation would be

$$x_j(k) = a_{(i,j)} x_i(k - \Delta_{(i,j)}) + n(k) \quad (4.13)$$

where $a_{(i,j)}$ is a scalar and $\Delta_{(i,j)}$ is the lag between electrodes i and j . The noise will be modelled as uncorrelated zero-mean Gaussian noise with a variance σ_n^2 , so $n(k) \sim \mathcal{N}(0, \sigma_n^2)$. The likelihood $L(\Delta_{(i,j)})$ as a function of the lag is then

$$L(\Delta_{(i,j)}) = \prod_k \left(\frac{1}{\sqrt{2\pi\sigma_n^2}} \exp \left(\frac{-[x_j(k) - a_{(i,j)} x_i(k - \Delta_{(i,j)})]^2}{2\sigma_n^2} \right) \right). \quad (4.14)$$

It is often easier to take the logarithm of the likelihood. The logarithm is a monotonically increasing function so the maximum will be reached at the same value of the parameters. The log-likelihood is then

$$\ln L(\Delta_{(i,j)}) = K \ln \left(\frac{1}{\sqrt{2\pi\sigma_n^2}} \right) - \frac{1}{2\sigma_n^2} \sum_k [x_j(k) - a_{(i,j)} x_i(k - \Delta_{(i,j)})]^2. \quad (4.15)$$

The terms K and σ_n^2 are constant in this setting and they will be written as such for ease of notation. The resulting log-likelihood is then

$$\ln L(\Delta_{(i,j)}) = -\frac{1}{2\sigma_n^2} \left(\sum_k [x_j(k)]^2 - \sum_k [a_{(i,j)} x_j(k) x_i(k - \Delta_{(i,j)})] + \sum_k [a_{(i,j)} x_i(k - \Delta_{(i,j)})]^2 \right) + \text{constant}. \quad (4.16)$$

The sums of the squared values of x_i and x_j can also be written as constant terms with respect to the time shift and can be replaced by the variance of the electrode $\sigma_i^2 = \frac{1}{K} \sum_k [x_i(k)]^2$, which does not depend on the time shift of the signal. This then results in

$$\ln L(\Delta_{(i,j)}) = -\frac{1}{2\sigma_n^2} \left(K\sigma_j^2 + a_{(i,j)}^2 K\sigma_i^2 - \sum_k [a_{(i,j)} x_j(k) x_i(k - \Delta_{(i,j)})] \right) + \text{constant}. \quad (4.17)$$

We also assume that $a_{(i,j)}$ is constant with respect to the time shift, but unknown. It is not dependent on k or $\Delta_{(i,j)}$, so it can be moved outside the summation over k , resulting in

$$\ln L(\Delta_{(i,j)}) = \frac{a_{(i,j)}}{2\sigma_n^2} \sum_k [x_j(k) x_i(k - \Delta_{(i,j)})] + \text{constant} \quad (4.18)$$

where the summation over the product of the two electrode signals with a time shift is the only term remaining which depends on $\Delta_{(i,j)}$. This exact term also appears in the cross-correlation calculation, if the means of the data are subtracted, and so

$$\arg \max_{\Delta_{(i,j)}} \ln L(\Delta_{(i,j)}) = \arg \max_{\Delta_{(i,j)}} \rho_{(i,j)}(\Delta_{(i,j)}). \quad (4.19)$$

Under these strict assumptions the cross-correlation estimate of the lag is equal to the ML estimate.

4.4. From inter-electrode lag to LAT

The cross-correlation method does not provide LATs directly. It provides estimated time differences (lags) $\hat{\Delta}$ between pairs of electrodes. The time differences can be expressed as a linear system of the absolute times τ as

$$\begin{bmatrix} \hat{\Delta}_{(1,2)} \\ \hat{\Delta}_{(1,3)} \\ \vdots \\ \hat{\Delta}_{(i,j)} \end{bmatrix} = \begin{bmatrix} \tau_2 - \tau_1 \\ \tau_3 - \tau_1 \\ \vdots \\ \tau_j - \tau_i \end{bmatrix} + \begin{bmatrix} \epsilon_{(1,2)} \\ \epsilon_{(1,3)} \\ \vdots \\ \epsilon_{(i,j)} \end{bmatrix} \quad (4.20)$$

where $\hat{\Delta}_{(i,j)}$ is the time difference estimated between electrodes i and j , τ_i is the true activation time of electrode i and with $\epsilon_{(i,j)}$ being an error introduced by the estimation of the lag of a pair of electrodes. Rewriting this system gives

$$\begin{bmatrix} \hat{\Delta}_{(1,2)} \\ \hat{\Delta}_{(1,3)} \\ \vdots \\ \hat{\Delta}_{(2,3)} \\ \vdots \\ \hat{\Delta}_{(i,j)} \end{bmatrix} = \begin{bmatrix} -1 & 1 & 0 & 0 & \dots & 0 & \dots & 0 \\ -1 & 0 & 1 & 0 & \dots & 0 & \dots & 0 \\ \vdots & \vdots & \vdots & \vdots & & \vdots & & \vdots \\ 0 & -1 & 1 & 0 & \dots & 0 & \dots & 0 \\ \vdots & \vdots & \vdots & \vdots & & \vdots & & \vdots \\ 0 & 0 & 0 & 0 & \dots & -1 & \dots & 1 \end{bmatrix} \begin{bmatrix} \tau_1 \\ \tau_2 \\ \tau_3 \\ \vdots \\ \tau_i \\ \vdots \\ \tau_j \end{bmatrix} + \begin{bmatrix} \epsilon_{(1,2)} \\ \epsilon_{(1,3)} \\ \vdots \\ \epsilon_{(2,3)} \\ \vdots \\ \epsilon_{(i,j)} \end{bmatrix}. \quad (4.21)$$

This system can be constructed using the incidence matrix \mathbf{B} of the graph of Ξ as the time delays were calculated for all the links in that graph. The system in vector form then becomes

$$\mathbf{d} = \mathbf{B}^T \boldsymbol{\tau} + \mathbf{e} \quad (4.22)$$

where \mathbf{d} is a length L vector of the lags estimated with a cross-correlation method, it can also be seen as a list of the weighted links from adjacency matrix \mathbf{D} . This is related to the absolute activation times $\boldsymbol{\tau}$ by the incidence matrix \mathbf{B} of size $M \times L$. This is an underdetermined system as it is rank deficient. For a connected graph, the rank of the incidence matrix \mathbf{B} is one less than its maximum rank, in this case the rank is $M - 1$.

4.4.1. Assuming equal noise variances

Information about the error introduced when obtaining the delays between electrodes can help in estimating the LATs. The mean and variance of the error are properties that, if known, can be used to obtain linear estimators with the lowest variance of the desired parameters [55]. To start, say we want to find the parameters $\boldsymbol{\tau}$ that minimize the square of the error as

$$\hat{\boldsymbol{\tau}} = \arg \min_{\boldsymbol{\tau}} \|\mathbf{e}\|_2^2 = \arg \min_{\boldsymbol{\tau}} \|\mathbf{d} - \mathbf{B}^T \boldsymbol{\tau}\|_2^2. \quad (4.23)$$

Let us assume the error is zero-mean, so

$$E[\epsilon_i] = 0, \text{ for } i \in 1, 2, \dots, L. \quad (4.24)$$

Let us also assume the error is homoscedastic, which means all observation have the same finite variance. The covariance matrix is then a diagonal matrix

$$\text{Cov}(\mathbf{e}) = c\mathbf{I} \quad (4.25)$$

with $0 \leq c < \infty$. The Gauss-Markov theorem [55] then gives a best linear unbiased estimator (BLUE). This is also called the ordinary least squares (OLS) estimator, and for the estimate of the absolute times $\hat{\boldsymbol{\tau}}$, that is,

$$\hat{\boldsymbol{\tau}} = (\mathbf{B}\mathbf{B}^T)^{-1}\mathbf{B}\mathbf{d}. \quad (4.26)$$

However since \mathbf{B}^T is not full rank this cannot be directly solved. One option is to add an extra entry to the linear system, setting one τ to a specific value, making the system not underdetermined anymore. Another option is using the Moore-Penrose inverse (pseudoinverse) of matrix \mathbf{B}^T to find a solution to Eq. (4.23), that is,

$$\hat{\boldsymbol{\tau}} = (\mathbf{B}^T)^\dagger \mathbf{d}. \quad (4.27)$$

This pseudoinverse can be calculated for rank-deficient matrices using the singular value decomposition (SVD), which is given by

$$\text{SVD}(\mathbf{B}^T) = \mathbf{U} \begin{bmatrix} \boldsymbol{\Sigma} & \mathbf{0} \\ \mathbf{0} & \mathbf{0} \end{bmatrix} \mathbf{V}^T \quad (4.28)$$

where in reality the smallest singular values will not exactly be 0 but a threshold is adopted. In this case this will be easy as the rank of matrix \mathbf{B}^T is known as was previously mentioned. This can then be used to calculate the pseudoinverse [56]

$$(\mathbf{B}^T)^\dagger = \mathbf{V} \begin{bmatrix} \boldsymbol{\Sigma}^{-1} & \mathbf{0} \\ \mathbf{0} & \mathbf{0} \end{bmatrix} \mathbf{U}^T. \quad (4.29)$$

This solution then has the minimum norm $\|\boldsymbol{\tau}^T \boldsymbol{\tau}\|$ and is sometimes called a minimum length solution.

Another method to estimate the activation times from the lags is by using a regularized least squares approach with Tikhonov (L2) regularization. The cost function to be minimized is then

$$\hat{\boldsymbol{\tau}} = \underset{\boldsymbol{\tau}}{\text{argmin}} \|\mathbf{d} - \mathbf{B}^T \boldsymbol{\tau}\|_2^2 + \lambda \|\boldsymbol{\tau}\|_2^2 \quad (4.30)$$

The amount of regularization is determined by the parameter λ . The solution to the least squares cost function is then

$$\hat{\boldsymbol{\tau}} = (\mathbf{B}\mathbf{B}^T + \lambda \mathbf{I})^{-1} \mathbf{B}\mathbf{d}. \quad (4.31)$$

This finally leads to a vector of estimated activation times per electrode $\hat{\boldsymbol{\tau}}$. The difference between the pseudoinverse and regularization methods shrinks as λ becomes smaller. Eventually they become the same values as the following limit exists [56],

$$\lim_{\lambda \rightarrow 0} (\mathbf{B}\mathbf{B}^T + \lambda \mathbf{I})^{-1} \mathbf{B} = (\mathbf{B}^T)^\dagger. \quad (4.32)$$

It might be useful to not let λ go to 0 for some cases, to not overfit on large errors.

The estimated absolute times are then distributed around zero, having a common reference time ($\tau = 0$). This reference can be changed by subtracting the minimum activation time, implying the first activation happens at time-point 0, so $\min_i \hat{\tau}_i = 0$.

4.4.2. Assuming unequal, unstructured noise variances

It can also be assumed that the noise covariance matrix \mathbf{C} is not a scaled version of the identity matrix. For this generalization the covariance is

$$\text{Cov}(\boldsymbol{\epsilon}) = \mathbf{C}, \quad (4.33)$$

which then is used to estimate the parameters $\boldsymbol{\tau}$. The result is the generalized least squares (GLS) estimator, which for the LATs would be [57]

$$\hat{\boldsymbol{\tau}} = (\mathbf{B}\mathbf{C}^{-1}\mathbf{B}^T)^{-1}\mathbf{B}\mathbf{C}^{-1}\mathbf{d}. \quad (4.34)$$

The covariance matrix is most likely not known beforehand. This means it has to be estimated. First let us assume the errors of different observations are not correlated and can be different, so the observations are heteroscedastic. The covariance matrix will then be a diagonal matrix of the form

$$\mathbf{C} = \begin{bmatrix} \sigma_{(1,2)}^2 & 0 & 0 & 0 & 0 & 0 \\ 0 & \sigma_{(1,3)}^2 & 0 & 0 & 0 & 0 \\ 0 & 0 & \ddots & 0 & 0 & 0 \\ 0 & 0 & 0 & \sigma_{(2,3)}^2 & 0 & 0 \\ 0 & 0 & 0 & 0 & \ddots & 0 \\ 0 & 0 & 0 & 0 & 0 & \sigma_{(i,j)}^2 \end{bmatrix} \quad (4.35)$$

where $\sigma_{(i,j)}^2$ is the variance of the estimated lag between electrodes i and j . A method to estimate the variances is to use the residual r of the OLS solution's estimates [58]. First the LATs are calculated as in the homoscedastic example, that is,

$$\hat{\mathbf{t}}_{init} = (\mathbf{B}\mathbf{B}^T + \lambda\mathbf{I})^{-1}\mathbf{B}\mathbf{d}. \quad (4.36)$$

The initial OLS estimates $\hat{\mathbf{t}}_{init}$ are then used to calculate the residuals in a length L vector \mathbf{r} as

$$\mathbf{r} = \mathbf{d} - \mathbf{B}^T\hat{\mathbf{t}}_{init} \quad (4.37)$$

The squares of the residuals are then used as an estimate for the variance. They are thus put on the diagonal of an $L \times L$ matrix. A term for quantization noise is also added. Because the cross-correlation estimates of the lags can only be multiples of the sample time, this quantization effect can be modelled as an error resulting from a uniform distribution from $-T_s/2$ to $T_s/2$ for every observation. The resulting estimated noise covariance matrix is

$$\hat{\mathbf{C}} = \text{diag}([r_1^2, r_2^2, \dots, r_L^2]) + q\mathbf{I}, \quad (4.38)$$

where r_l^2 is the l th squared entry of the residual vector and q is the quantization noise variance.

Having now calculated the estimated correlation matrix $\hat{\mathbf{C}}$, the GLS estimate for the LATs can be determined. Because the matrix \mathbf{B} is still rank-deficient, regularization is again applied. The resulting estimate is

$$\hat{\mathbf{t}} = (\mathbf{B}\hat{\mathbf{C}}^{-1}\mathbf{B}^T + \lambda\mathbf{I})^{-1}\mathbf{B}\hat{\mathbf{C}}^{-1}\mathbf{d} \quad (4.39)$$

The covariance matrix can be iteratively estimated further [59]. What would be done is that the estimated covariance matrix for step n , $\hat{\mathbf{C}}_{(n)}$, would be used to calculate the estimated LATs $\hat{\mathbf{t}}_{(n+1)}$ as

$$\hat{\mathbf{t}}_{(n+1)} = (\mathbf{B}\hat{\mathbf{C}}_{(n)}^{-1}\mathbf{B}^T + \lambda\mathbf{I})^{-1}\mathbf{B}\hat{\mathbf{C}}_{(n)}^{-1}\mathbf{d}. \quad (4.40)$$

These updated LATs are then used to calculate a new residual, which is used to then obtain a new $\hat{\mathbf{C}}_{(n+1)}$. It must be noted that for smaller sample sizes there is no guarantee these methods provide better performance than the OLS method [59].

4.4.3. Assuming unequal, structured noise variances

In the previous section, the variance of each observation (delay) was estimated separately. The errors were assumed to be independent across all the links in the connectivity graph. The underlying graph structure can be used to construct a more structured approach to estimating the error covariance matrix.

In this section we assume that the error variances of the links are determined by the nodes in the graph, not by the links individually. However, for now we also assume the errors are still independent. The reason this might be an interesting assumption is that when cross-correlating one node with two different connected nodes, the resulting errors after the cross-correlation process can heavily depend on the morphology of the signals of those connected nodes. The assumption that these errors are always positively or negatively correlated might then be inaccurate. The result will then be an estimated covariance matrix with only entries on the diagonal, that depend on the parameters from the nodes. In Section 4.4.4 we will investigate what happens if we do not assume that the errors of the observed delays are independent.

We assume now that the variance of the error of an observation on link (i, j) is a summation of the variances belonging to nodes i and j , so

$$\text{Var}(\epsilon_{(i,j)}) = \sigma_i^2 + \sigma_j^2. \quad (4.41)$$

The covariance between two different links, (i, j) and (f, g) where $i, j, g, f \in 1, 2, \dots, M$ and $(i, j) \neq (g, f)$, is assumed to be 0, so $\text{Cov}(\epsilon_{(i,j)}, \epsilon_{(f,g)}) = 0$. The error between of different links are thus still assumed to be uncorrelated. The resulting covariance matrix \mathbf{C} then is assumed to have the structure

$$\text{Cov} \begin{pmatrix} \epsilon_{(1,2)} \\ \epsilon_{(1,3)} \\ \vdots \\ \epsilon_{(2,3)} \\ \vdots \\ \epsilon_{(i,j)} \end{pmatrix} = \mathbf{C} = \begin{bmatrix} \sigma_1^2 + \sigma_2^2 & 0 & 0 & 0 & 0 & 0 \\ 0 & \sigma_1^2 + \sigma_3^2 & 0 & 0 & 0 & 0 \\ 0 & 0 & \ddots & 0 & 0 & 0 \\ 0 & 0 & 0 & \sigma_2^2 + \sigma_3^2 & 0 & 0 \\ 0 & 0 & 0 & 0 & \ddots & 0 \\ 0 & 0 & 0 & 0 & 0 & \sigma_i^2 + \sigma_j^2 \end{bmatrix} \quad (4.42)$$

where the summation of the variances of the nodes belonging to the links can be seen on the diagonal. In the same way as was done for the unstructured variance method, the OLS residuals can be used to estimate the variances. The residual on link (i, j) would be

$$r_{(i,j)}^2 = \sigma_i^2 + \sigma_j^2 \quad (4.43)$$

where σ_i^2 and σ_j^2 must then be determined. This can be done by putting the residuals in a vector, creating a linear set of equations

$$\begin{bmatrix} r_{(1,2)}^2 \\ r_{(1,3)}^2 \\ \vdots \\ r_{(i,j)}^2 \end{bmatrix} = \begin{bmatrix} 1 & 1 & 0 & 0 & \dots & 0 & \dots & 0 \\ 1 & 0 & 1 & 0 & \dots & 0 & \dots & 0 \\ \vdots & \vdots & \vdots & \vdots & & \vdots & & \vdots \\ 0 & 0 & 0 & 0 & \dots & 1 & \dots & 1 \end{bmatrix} \begin{bmatrix} \sigma_1^2 \\ \sigma_2^2 \\ \sigma_3^2 \\ \vdots \\ \sigma_i^2 \\ \vdots \\ \sigma_j^2 \end{bmatrix} \quad (4.44)$$

which is a system that uses the positive incidence matrix \mathbf{B}^+ of the graph Ξ , so it is the incidence matrix used before but with all positive entries. The squared residuals vector is $\boldsymbol{\eta}$, and the vector of variances to be estimated is $\boldsymbol{\zeta}$. The linear system then becomes

$$\boldsymbol{\eta} = \mathbf{B}^{+T} \boldsymbol{\zeta}. \quad (4.45)$$

A least squares estimation of the variances can then be done. The matrix \mathbf{B}^{+T} is a full rank (rank M) matrix so it should provide the desired estimates directly. The variances however cannot be negative, so a non-negative least squares (NNLS) implementation is used,

$$\begin{aligned} \hat{\boldsymbol{\zeta}} &= \arg \min_{\boldsymbol{\zeta}} \left\| \boldsymbol{\eta} - \mathbf{B}^{+T} \boldsymbol{\zeta} \right\|_2^2 \\ &\text{s.t. } \boldsymbol{\zeta} \geq 0 \end{aligned} \quad (4.46)$$

where $\hat{\boldsymbol{\zeta}}$ is the vector of estimated variances. If the model is correct the estimated variances should be positive anyway. To cope with the imperfections of this variance estimation method, the NNLS estimation is done in MATLAB with the `lsqnonneg` function. The estimated covariance matrix is then constructed as

$$\hat{\mathbf{C}} = \text{diag}(\mathbf{B}^{+T} \hat{\boldsymbol{\zeta}}) + q\mathbf{I} \quad (4.47)$$

with the quantization variance q again added. With this estimated covariance the LATs can be estimated in the same way as was done in the previous section with the GLS estimate.

4.4.4. Off-diagonal elements in the noise covariance matrix

In the previous sections the covariance matrix was assumed to only have non-zero entries on the diagonal. If the errors on the estimated lags are actually correlated, the covariance matrix can have off-diagonal entries. Let us assume the error on the estimate lag between electrode i and j , $\hat{\Delta}_{(i,j)}$, is comprised of the intrinsic error of electrode i , $\epsilon_{(i)}$, and the intrinsic error of electrode j , $\epsilon_{(j)}$. The estimated delay is then

$$\hat{\Delta}_{(i,j)} = \tau_j - \tau_i + \epsilon_{(j)} - \epsilon_{(i)}, \quad (4.48)$$

which means $\epsilon_{(i,j)} = \epsilon_{(j)} - \epsilon_{(i)}$. This has as a result that the covariance between the errors on the observations is not equal to 0, so for pairs (i, j) and (i, z) , with $i, j, z \in 1, 2, \dots, M$, the covariance is $\text{Cov}(\epsilon_{(i,j)}\epsilon_{(i,z)}) \neq 0$. Putting this in matrix form gives the model

$$\mathbf{d} = \mathbf{B}^T(\boldsymbol{\tau} + \boldsymbol{\epsilon}_\tau) \quad (4.49)$$

where \mathbf{d} is the the length L vector containing the estimated lags, \mathbf{B} is again the incidence matrix of Ξ , $\boldsymbol{\tau}$ is the vector of true activation times and $\boldsymbol{\epsilon}_\tau$ is the length M vector of errors belonging to each electrode. Let us again assume the error is zero-mean. The error covariance matrix \mathbf{C} of this model would then be

$$\mathbf{C} = E[\mathbf{B}^T \boldsymbol{\epsilon}_\tau \boldsymbol{\epsilon}_\tau^T \mathbf{B}] = \mathbf{B}^T \mathbf{C}_\tau \mathbf{B} \quad (4.50)$$

where \mathbf{C}_τ is the covariance matrix of the electrode error which is unknown for now. The covariance matrix with the structure $\mathbf{B}^T \mathbf{C}_\tau \mathbf{B}$ is actually a singular matrix as \mathbf{B} is rank-deficient as was mentioned before. There are methods available [60] that use the pseudoinverse to calculate the inverse of \mathbf{C} to use it in a GLS solution. For now lets assume it is non-singular to see what happens if we use it in a GLS setting. Taking the GLS estimate of $\boldsymbol{\tau}$ from Eq. (4.34) and using the covariance matrix found the estimate becomes

$$\hat{\boldsymbol{\tau}} = (\mathbf{B}(\mathbf{B}^T \mathbf{C}_\tau \mathbf{B})^{-1} \mathbf{B}^T)^{-1} \mathbf{B}(\mathbf{B}^T \mathbf{C}_\tau \mathbf{B})^{-1} \mathbf{d}. \quad (4.51)$$

If both sides are multiplied by $\mathbf{B}(\mathbf{B}^T \mathbf{C}_\tau \mathbf{B})\mathbf{B}^T$ this becomes

$$\mathbf{B}(\mathbf{B}^T \mathbf{C}_\tau \mathbf{B})^{-1} \mathbf{B}^T \hat{\boldsymbol{\tau}} = \mathbf{B}(\mathbf{B}^T \mathbf{C}_\tau \mathbf{B})^{-1} \mathbf{d}. \quad (4.52)$$

Multiplying both sides by $\mathbf{B}^T \mathbf{C}_\tau$ now gives

$$\mathbf{B}^T \mathbf{C}_\tau \mathbf{B}(\mathbf{B}^T \mathbf{C}_\tau \mathbf{B})^{-1} \mathbf{B}^T \hat{\boldsymbol{\tau}} = \mathbf{B}^T \mathbf{C}_\tau \mathbf{B}(\mathbf{B}^T \mathbf{C}_\tau \mathbf{B})^{-1} \mathbf{d}. \quad (4.53)$$

This can now be simplified to

$$\mathbf{B}^T \hat{\boldsymbol{\tau}} = \mathbf{d}, \quad (4.54)$$

which results in the estimate of the activation times

$$\hat{\boldsymbol{\tau}} = (\mathbf{B}\mathbf{B}^T)^{-1} \mathbf{B}\mathbf{d}. \quad (4.55)$$

The GLS solution for this type of error model is thus the OLS solution again. The estimation of the activation times in this model then does not depend on the covariance matrix of the errors of the electrodes \mathbf{C}_τ .

Let us now introduce the quantization error vector $\boldsymbol{\epsilon}_q$ to the model. This error is independent per measurement, with a covariance matrix $\mathbf{C}_q = q\mathbf{I}$. The model becomes

$$\mathbf{d} = \mathbf{B}^T \boldsymbol{\tau} + \mathbf{B}^T \boldsymbol{\epsilon}_\tau + \boldsymbol{\epsilon}_q. \quad (4.56)$$

From this model the maximum likelihood estimator can be derived when assuming $\boldsymbol{\epsilon}_\tau$ and $\boldsymbol{\epsilon}_q$ are independent and zero mean with a Gaussian distribution [61]. The estimate for the activation times then becomes [61]

$$\hat{\boldsymbol{\tau}} = (\mathbf{B}(\mathbf{B}^T \mathbf{C}_\tau \mathbf{B} + \mathbf{C}_q)^{-1} \mathbf{B}^T)^{-1} \mathbf{B}(\mathbf{B}^T \mathbf{C}_\tau \mathbf{B} + \mathbf{C}_q)^{-1} \mathbf{d}. \quad (4.57)$$

Rewriting this the expression,

$$\mathbf{B}(\mathbf{B}^T \mathbf{C}_\tau \mathbf{B} + \mathbf{C}_q)^{-1} \mathbf{B}^T \hat{\boldsymbol{\tau}} = \mathbf{B}(\mathbf{B}^T \mathbf{C}_\tau \mathbf{B} + \mathbf{C}_q)^{-1} \mathbf{d} \quad (4.58)$$

can be obtained. The matrix $\mathbf{C}_q = q\mathbf{I}$ is known to be a scaled version of the identity matrix. This gives

$$\mathbf{B}(\mathbf{B}^T \mathbf{C}_\tau \mathbf{B} + q\mathbf{I})^{-1} \mathbf{B}^T \hat{\boldsymbol{\tau}} = \mathbf{B}(\mathbf{B}^T \mathbf{C}_\tau \mathbf{B} + q\mathbf{I})^{-1} \mathbf{d}, \quad (4.59)$$

which can be rewritten again when multiplied by \mathbf{C}_τ to

$$\frac{1}{q} \mathbf{C}_\tau \mathbf{B} (\mathbf{B}^T \frac{1}{q} \mathbf{C}_\tau \mathbf{B} + \mathbf{I})^{-1} \mathbf{B}^T \hat{\boldsymbol{\tau}} = \frac{1}{q} \mathbf{C}_\tau \mathbf{B} (\mathbf{B}^T \frac{1}{q} \mathbf{C}_\tau \mathbf{B} + \mathbf{I})^{-1} \mathbf{d}. \quad (4.60)$$

Using the matrix identity [62] $\mathbf{A}^{-1} \mathbf{B} (\mathbf{B}^T \mathbf{A}^{-1} \mathbf{B} + \mathbf{I})^{-1} = (\mathbf{A} + \mathbf{B} \mathbf{B}^T)^{-1} \mathbf{B}$ with $\mathbf{A}^{-1} = \frac{1}{q} \mathbf{C}_\tau$ the following can be obtained

$$(q\mathbf{C}_\tau^{-1} + \mathbf{B} \mathbf{B}^T)^{-1} \mathbf{B} \mathbf{B}^T \hat{\boldsymbol{\tau}} = (q\mathbf{C}_\tau^{-1} + \mathbf{B} \mathbf{B}^T)^{-1} \mathbf{B} \mathbf{d}. \quad (4.61)$$

Multiplying each side by $(q\mathbf{C}_\tau^{-1} + \mathbf{B} \mathbf{B}^T)$, the result is

$$\mathbf{B} \mathbf{B}^T \hat{\boldsymbol{\tau}} = \mathbf{B} \mathbf{d}, \quad (4.62)$$

which then is again the same as the OLS solution,

$$\hat{\boldsymbol{\tau}} = (\mathbf{B} \mathbf{B}^T)^{-1} \mathbf{B} \mathbf{d}. \quad (4.63)$$

The results of assuming the error on the links is a summation of the intrinsic errors of the nodes, is that the information about the covariance of the errors is not used at all. The OLS estimator is for this model then the same as the GLS estimator.

4.4.5. Cramér-Rao lower bound

For unbiased estimators, there is a lower bound on the variance, given by the Cramér-Rao (lower) bound (CRLB) [63] and is determined by the inverse of the Fisher information matrix \mathbf{J} . The bound is given by

$$E[(\hat{\boldsymbol{\tau}} - \boldsymbol{\tau})(\hat{\boldsymbol{\tau}} - \boldsymbol{\tau})^T] \geq \mathbf{J}^{-1} \quad (4.64)$$

where $\hat{\boldsymbol{\tau}}$ is an unbiased estimator of the parameters $\boldsymbol{\tau}$. The entries of the Fisher information matrix are dependent on the distribution of our observations \mathbf{d} given the parameters $\boldsymbol{\tau}$. Given the probability density function $p(\mathbf{d}|\boldsymbol{\tau})$ of the observations, the Fisher information matrix is

$$\mathbf{J} = -E \left[\frac{d^2}{d\boldsymbol{\tau}^2} \ln p(\mathbf{d}|\boldsymbol{\tau}) \right]. \quad (4.65)$$

The derivation of this matrix for our data model is given in Appendix A. The resulting Fisher information matrix is

$$\mathbf{J} = \mathbf{B} \mathbf{C}^{-1} \mathbf{B}^T, \quad (4.66)$$

with \mathbf{B} the incidence matrix introduced before and \mathbf{C} the covariance matrix of the observations. The variance of the GLS estimator from Eq. (4.34) is [57]

$$\text{Var}(\hat{\boldsymbol{\tau}}_{GLS}) = (\mathbf{B} \mathbf{C}^{-1} \mathbf{B}^T)^{-1} = \mathbf{J}^{-1}, \quad (4.67)$$

which means it reaches the CRLB. However, the covariance matrix \mathbf{C} must be known beforehand to obtain this estimator. If the incorrect covariance matrix is used for the GLS estimate the variance will be higher.

4.4.6. Combination with steepest deflection estimates

Due to the wide array of different morphologies of electrograms that can occur in epicardial electrograms, special cases can exist where cross-correlation will work less effectively. The LATs estimated with the steepest deflection method can then be combined with the time delays estimated with the cross-correlation to obtain new LAT estimates.

The times at which the steepest deflection was found, t_{sd} , are added as separate observations to the least-squares estimation of the LATs. The minimization is then formulated as

$$\hat{\boldsymbol{\tau}} = \underset{\boldsymbol{\tau}}{\text{argmin}} \left\| \mathbf{W}^{\frac{1}{2}} \left(\begin{bmatrix} \mathbf{d} \\ t_{sd} \end{bmatrix} - \begin{bmatrix} \mathbf{B}^T \\ \mathbf{I} \end{bmatrix} \boldsymbol{\tau} \right) \right\|_2^2 \quad (4.68)$$

where W is a diagonal matrix to add weights to observations. The weights will be constructed as

$$W = \begin{bmatrix} \mathbf{I}_{(L \times L)} & 0 \\ 0 & w\mathbf{I}_{(M \times M)} \end{bmatrix} \quad (4.69)$$

where w is a scalar that determines the influence of the steepest deflection LAT estimates. The estimated LATs with the combined method then follow from minimizing Eq. (4.68). The added SD estimates make the problem no longer underdetermined, so no regularization or SVD pseudoinverse is needed. The expression for the estimated LATs using the OLS estimator then is

$$\hat{\mathbf{t}} = \left(\begin{bmatrix} \mathbf{B}^T \\ \mathbf{I} \end{bmatrix}^T W \begin{bmatrix} \mathbf{B}^T \\ \mathbf{I} \end{bmatrix} \right)^{-1} \begin{bmatrix} \mathbf{B}^T \\ \mathbf{I} \end{bmatrix}^T W \begin{bmatrix} \mathbf{d} \\ \mathbf{t}_{sd} \end{bmatrix}. \quad (4.70)$$

4.5. Data window determination and comparison

The data that is supplied will most likely be a single time series for every electrode, containing multiple beats of the heart during SR. For the comparison of multiple LAT estimation methods, first a time window of the data needs to be selected for which the different algorithms will be evaluated. Secondly, the electrodes where the electrogram shows distinct multiple deflections in a single time window will be designated as *fractionated*. The performance of different LAT estimation methods can then also be evaluated only on those special cases. Lastly in this section, the performance metric to compare LAT estimated to their ground truth, where available, is explained.

4.5.1. Time windowing

To apply cross-correlation, a segment of the data has to be taken where a beat or single activation of the tissue is present. The segment also has to be short enough not to include the ventricular activity. The depolarization of the ventricles can be measured in the electrode array and happens shortly after the depolarization of the atria, so excluding it is important. For this a method was developed to determine the time window in which to determine the LAT.

An electrode that is confirmed to function properly beforehand is taken as a reference. The data from this electrode is filtered by a highpass filter, to isolate the atrial activity. This filtered data will be denoted as a $\mathbf{y} = [y(0), y(1), \dots, y(K-1)]$.

The algorithm to determine the time windows to be used is given in Algorithm 1. The data \mathbf{y} is evaluated in windows of $N_{window}/2$ samples, with the start of this window being shifted with N_{step} samples, where $N_{step} < N_{window}/2$, until the end of the data is reached. The reason only the first half of the window is evaluated, is because there needs to be enough time after the activity is detected to include the propagation through the whole array in the data.

At each step the absolute values of the data in the window are compared to a threshold a_{thres} . This threshold is determined as a fraction η , where $0 < \eta < 1$, of the maximum absolute value in the entire filtered data \mathbf{y} . If the window contains a value greater than the threshold in magnitude, the window will be considered active. The starting points of the active windows, \mathbf{k}_{window} , will be returned afterwards.

Algorithm 1 Time window selection

- 1: **procedure** WINDOWSELECT($\mathbf{y}, N_{window}, N_{step}, \eta$) \triangleright Select all time windows where there is atrial activity
 - 2: $a_{thres} = \eta * \max(|\mathbf{y}|)$ \triangleright Set a fraction of the maximum absolute value as a threshold
 - 3: $k = 0$
 - 4: $\mathbf{k}_{window} = \{\}$
 - 5: **while** $k + N_{window} \leq K - 1$ **do**
 - 6: $\mathbf{y}_{window} = [y_k, y_{k+1}, \dots, y_{k+(N_{window}/2)}]$ \triangleright Select a subset of the data
 - 7: **if** $\max(|\mathbf{y}_{window}|) > a_{thres}$ **then**
 - 8: $\mathbf{k}_{window} = \{\mathbf{k}_{window}, k\}$ \triangleright Append the starting point of the window to the list
 - 9: $k = k + N_{window}$
 - 10: **else**
 - 11: $k = k + N_{step}$
 - 12: **return** \mathbf{k}_{window} \triangleright The starting points of the active windows are returned
-

4.5.2. Determining fractionated electrodes

When evaluating an area of atrial tissue, some electrodes might be above an area where the tissue conduction is normal, and other electrodes might be right on top of an area with a large section of non-conducting tissue. It can therefore be interesting to evaluate the performance of different LAT estimation methods for only those electrodes where there is a problem in tissue conduction and the signal morphology might differ from the regular electrograms.

In this case the term *fractionated* is used for electrograms that show these irregularities in morphology. To find these cases, the electrograms are examined individually. The regular epicardial electrogram for normal conducting tissue was shown in Chapter 2, and it shows one clear negative deflection. If an electrogram has at least two discernible negative deflections in it, it will be characterized as fractionated.

4.5.3. Performance metric

If the true activation times of the cells are available, they can be compared to the estimated LATs for the electrode locations. This can be done by taking the root-mean-square error (RMSE). The RMSE of the estimated times $\hat{\tau}_i$ and the true times τ_i is then

$$RMSE = \sqrt{\frac{\sum_{i=1}^M (\hat{\tau}_i - \tau_i)^2}{M}} \quad (4.71)$$

where M is the total number of electrodes. If the estimated or true time is not available for a certain electrode then this one will not be taken into account when calculating the error. Its estimate is then eliminated from $\hat{\tau}$ and the number of electrodes M is adjusted. This can happen if an electrode is above an area of blocked conduction in the simulated tissue and the true activation time does not exist. It can also happen that an electrode is malfunctioning and does not record proper data, its contribution to the error should then also be 0.

5

Results

In this chapter, the methods of Chapter 4 will be applied to simulated and clinical data described in Chapter 3. In Section 5.1, results on simulated data are presented. Cross-correlation methods for estimation of LATs that use more data than only direct neighboring nodes are examined for different types of simulated tissue. The cross-correlation methods for increasing orders of neighbors are compared to other known methods. Only using direct neighbors is also evaluated in this section, and the difference between using OLS and GLS estimators for the LATs is evaluated as well. Finally combining cross-correlation and steepest deflection information is evaluated.

In Section 5.2, the cross-correlation method of using higher order neighbors is tested on data recorded from patients during open-heart surgery and compared to the steepest deflection estimates of activation times. The methods are tested on a range of different signal morphologies, their estimates are shown and the differences are highlighted.

5.1. Experiments on simulated data

In Section 3.1, the simulation of the atrial tissue was explained. That simulation will be used to create data sets to test the methods for estimating LATs. This is useful as the ground truth is known for these simulations and the error of the different methods can be compared.

In each data set, a single activation of the tissue will be simulated. In Section 4.5, giving electrodes the label *fractionated* was discussed. In this chapter, a threshold of 30% of the maximum value of the derivative is used, to determine when a secondary deflection is severe enough to say an electrogram is fractionated.

5.1.1. Data sets used

Two categories of data sets were examined. One with specially created blocks and one with more randomly distributed tissue deficiencies. The set of artificial non-conductive tissue shapes, **T1**, **T2** and **T3**, mentioned in Section 3.1 were examined first. They are shown again in Fig. 5.1.

The second type of data sets that will be examined are the fibrosis tissue sets, also shown in Section 3.1. Three different kinds were used, **S1**, **S2** and **S3**. For each of those, 10 iterations were randomly generated, with different conduction patterns. The areas under the electrode array that are simulated for each of the **S** sets are shown in Fig. 5.2, Fig. 5.3 and Fig. 5.4.

5.1.2. Cross-correlation over a higher order neighbors

First three methods are compared. The steepest deflection (SD) method is put against the normalized cross-correlation (NCC) and the normalized cross-correlation of the derivative (NDCC). Using the square grid graph as a base, the performance is compared when taking the cross-correlation over an increasing number of hops, so an increased order of neighbors P for the connectivity graph $\Xi^{(P)}$.

The estimation of the covariance matrix C of the observed lags between electrode pairs is not considered here yet. The OLS solution from Section 4.4 will be applied to transform the inter-electrode delays to the LATs. The effects of the covariance estimation are investigated later in Section 5.1.7.

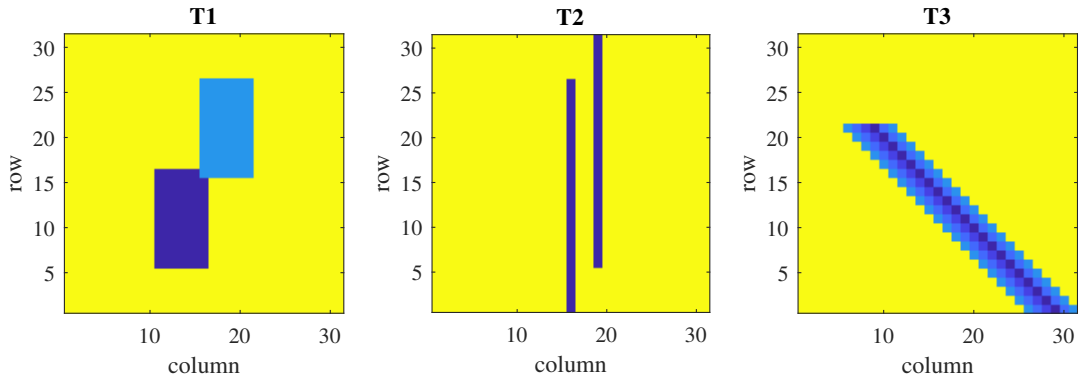


Figure 5.1: The conductivity maps for simulating specific shapes of blocks in the tissue, sets **T1**, **T2** and **T3**, are shown.

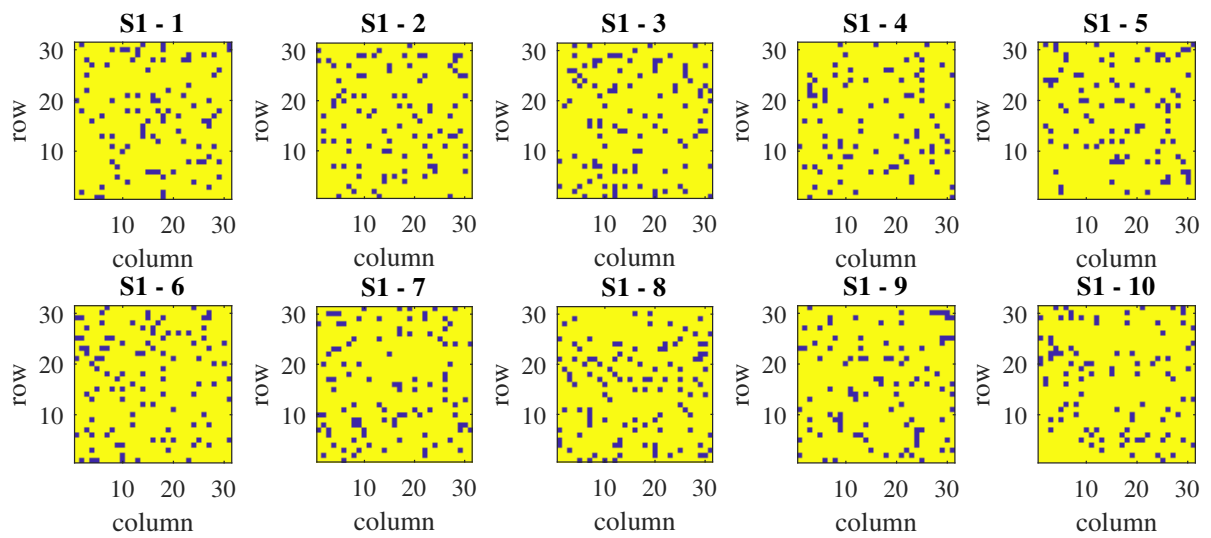


Figure 5.2: The 31×31 cells under the simulated electrodes are shown for the data sets **S1**.

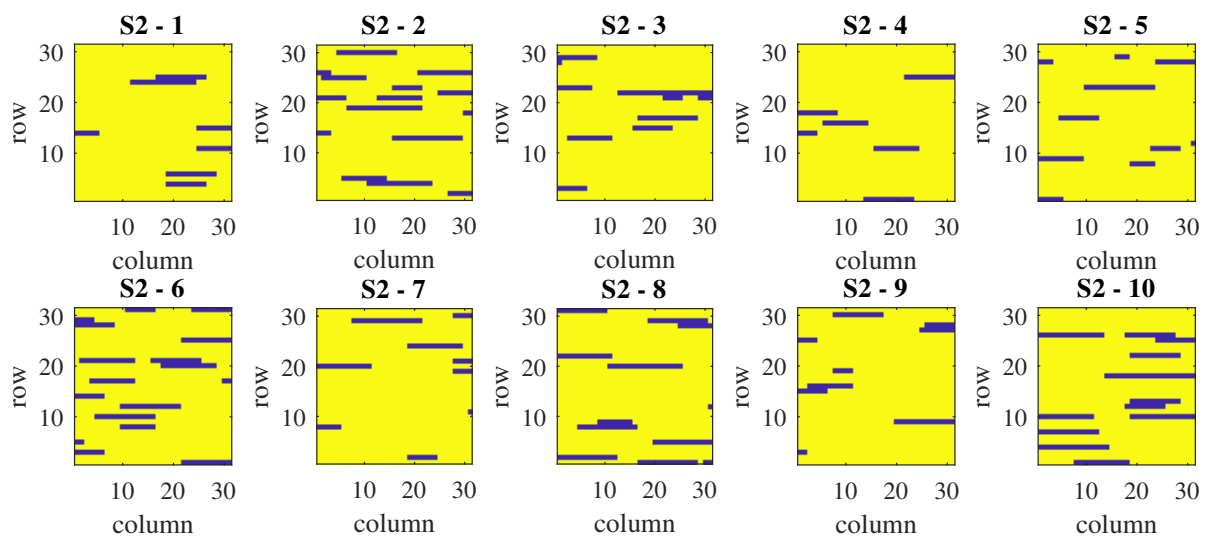


Figure 5.3: The 31×31 cells under the simulated electrodes are shown for the data sets **S2**.

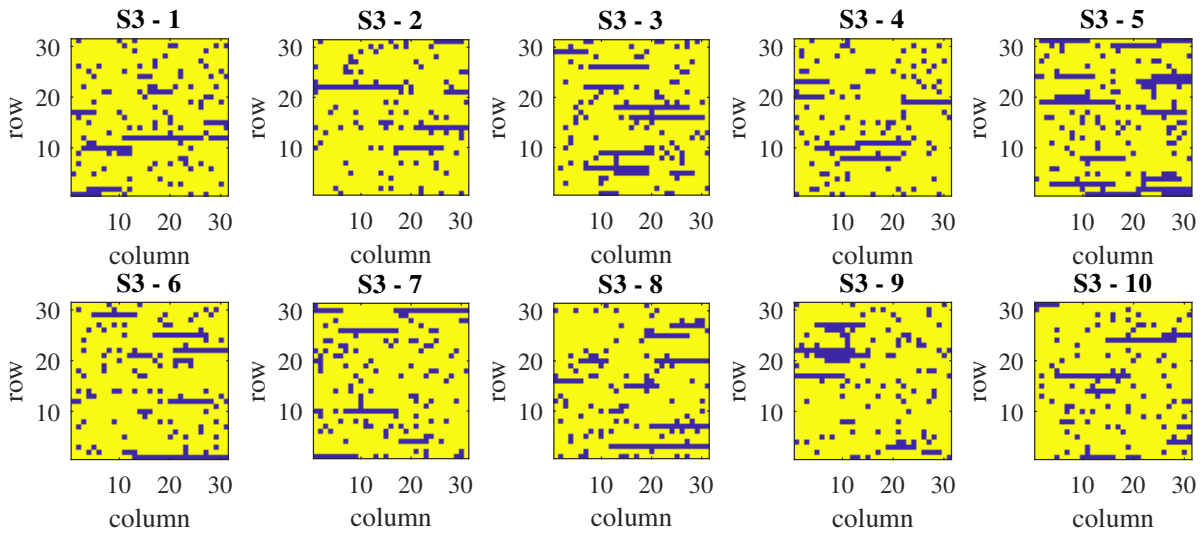


Figure 5.4: The 31×31 cells under the simulated electrodes are shown for the data sets S3.

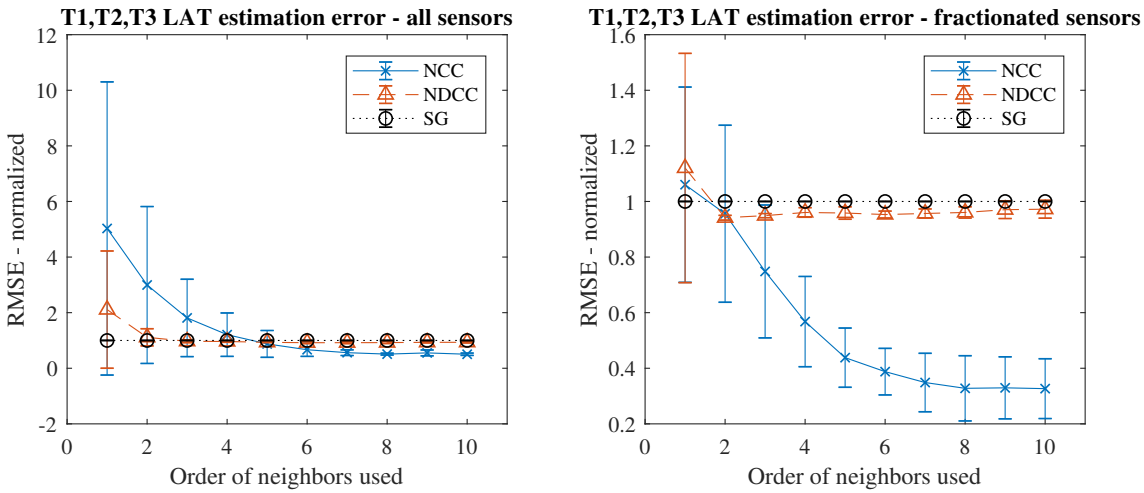


Figure 5.5: The normalized RMSE for sets T1, T2, T3 is shown. The error bars indicate the standard deviation. On the left the error on all electrodes is taken, on the right only the fractionated electrode signals are taken into account.

Special blocking shapes In Fig. 5.5 the resulting mean RMSE and standard deviation are shown for the T data sets. The RMSE is shown as normalized on the error of the SD, so the RMSE for SD is always 1 for every data set.

What can be observed is that the error of the cross-correlation LAT estimation methods is decreasing by using higher order neighboring pairs. This means increasing P in $\Xi^{(P)}$, so increasing the distance in the grid graph over which cross-correlations are calculated. The NCC method's error keeps decreasing well below the error of the SD method. This happens when taking all electrodes into account, and also when taking only the RMSE on electrodes where the signal is fractionated.

The NDCC method's error does decrease when higher-order neighbors are used but it converges to a value only marginally below the error of the SD. It seems the NDCC method does benefits from having a larger number of delays to calculate the LAT with when P increases at first. The derivative of the data however can be seen as a high-pass filtered version of the original electrogram. The high frequency components, such as steep deflections, will thus be more prominent than the low frequency components. The cross-correlation will then focus on these steep deflections and the resulting estimate is in the end similar to that of the SD method.

To give an overview of the non-normalized results, the RMSE in milliseconds is shown in Table 5.1 for the individual T data sets.

Table 5.1: The RMSE in milliseconds of the different methods for the special blocking shape data sets is shown, calculated for all electrodes and for only fractionated electrodes, indicated with an (f). The cross-correlation methods are shown for their direct (1-hop) neighbors and their 10th order neighbors (10-hops).

	SD	NCC-1	NCC-10	NDCC-1	NDCC-10
T1	2.41	3.00	1.27	2.21	2.26
T2	11.54	32.17	5.26	10.02	11.03
T3	0.93	10.31	0.49	4.24	0.85
T1 (f)	8.66	6.60	2.41	7.87	8.24
T2 (f)	27.69	40.08	12.46	23.72	26.47
T3 (f)	3.44	3.34	0.87	5.49	3.47

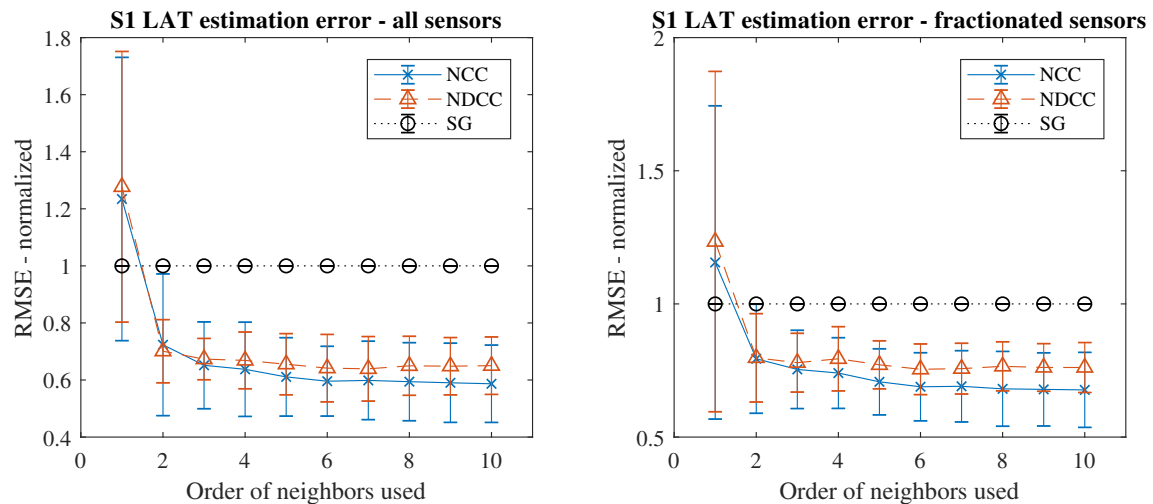


Figure 5.6: The normalized RMSE is shown for the 10 iterations of **S1**. The error bars indicate the standard deviation. On the left the error on all electrodes is taken, on the right only the fractionated electrode signals are taken into account.

Fibrosis tissue The same methods are now applied to the 10 sets generated for **S1**, **S2**, **S3**. In Fig. 5.6 the normalized RMSE is shown for set **S1**. As with the special blocking shapes, the error of the cross correlation methods drops below the error of the SD when using a higher order neighbors for which to calculate lags. The error measured only on the fractionated electrodes does not differ significantly from the error on all electrodes here.

What is also interesting is the NDCC method performing almost as well as the NCC method. This data set with the random dots of conduction block has limited blocking potential for activation going through it, so the absolute error is low and there is limited room for performance increases.

The results for **S2** are shown in Fig. 5.7. The zoomed-in version is shown in Fig. 5.8. The same trend is visible, the cross-correlation methods again perform better than the SD method when a higher order of neighbors is used. It is also visible that the method using the derivative, NDCC, performs somewhat worse than the regular NCC method.

The results for **S3** are shown in Fig. 5.9. The zoomed-in version is shown in Fig. 5.10. The same trend as in the other two sets is visible. The spread of the RMSE however has become larger. A larger area of the simulated tissue is now covered in non-conductive tissue so the potential for improvement will also be greater in this set.

The mean of the RMSE in milliseconds of the methods used for these simulations is shown in Table 5.2. Using the higher order neighbors to determine lags in NCC methods gives the best performance in every simulation examined.

Conclusions From both the **T** sets and the **S** sets it can be observed that the methods using the cross-correlation improves vastly when using more than the direct neighboring nodes to calculate the lag. It can also be observed that the NCC method outperforms the other methods when using lag estimation over higher order neighbors instead of only direct ones.

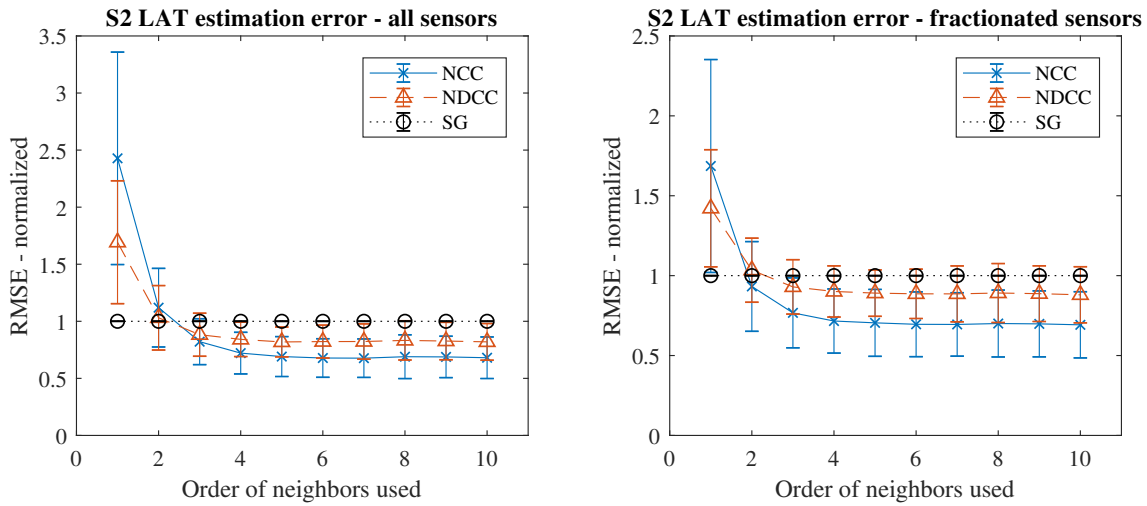


Figure 5.7: The normalized RMSE is shown for the 10 iterations of **S2**. The error bars indicate the standard deviation. On the left the error on all electrodes is taken, on the right only the fractionated electrode signals are taken into account.

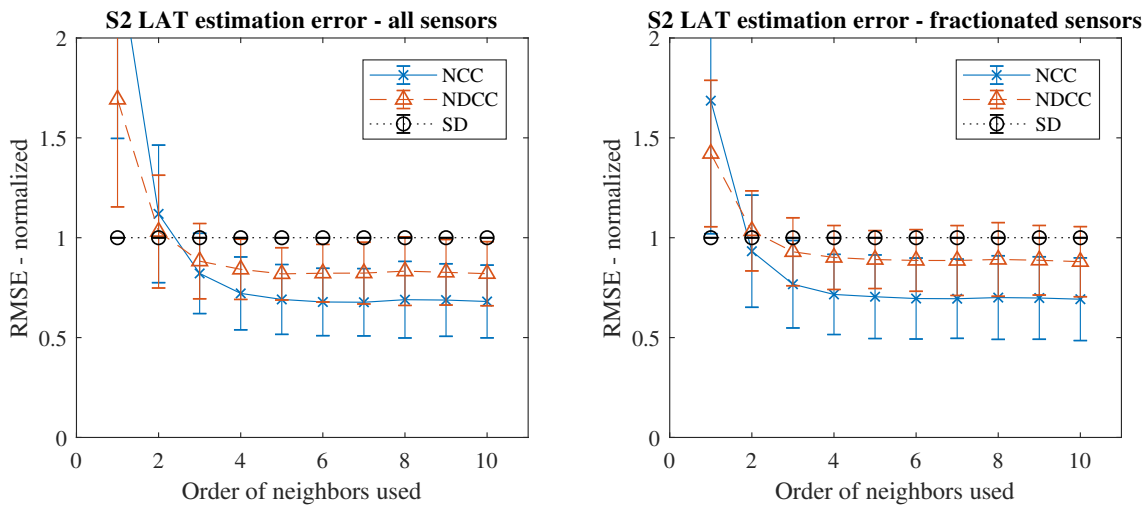


Figure 5.8: The normalized RMSE of **S2** from Fig. 5.7 is shown here with a zoomed-in y-axis. The error bars indicate the standard deviation. On the left the error on all electrodes is taken, on the right only the fractionated electrode signals are taken into account.

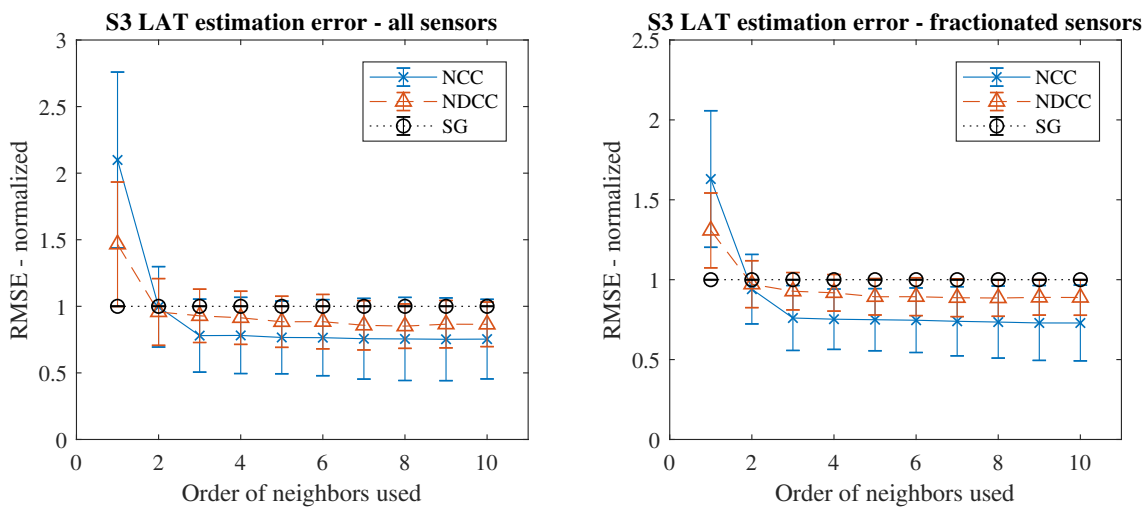


Figure 5.9: The normalized RMSE is shown for the 10 iterations of **S3**. The error bars indicate the standard deviation. On the left the error on all electrodes is taken, on the right only the fractionated electrode signals are taken into account.

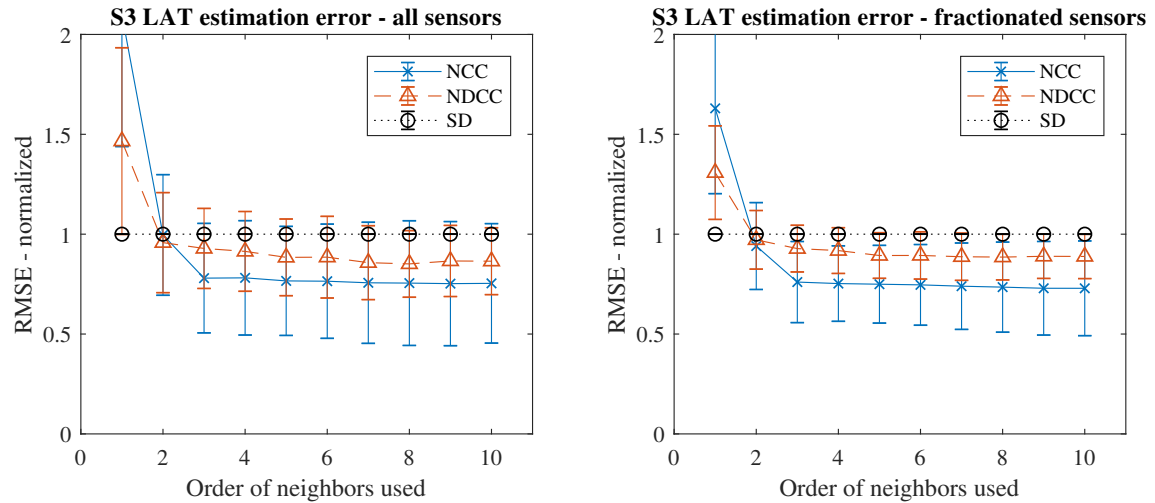


Figure 5.10: The normalized RMSE of **S3** from Fig. 5.9 is shown here with a zoomed-in y-axis. The error bars indicate the standard deviation. On the left the error on all electrodes is taken, on the right only the fractionated electrode signals are taken into account.

Table 5.2: The mean RMSE in milliseconds for the 10 simulations for sets **S1**, **S2** and **S3** is shown, calculated for all electrodes and for only fractionated electrodes, indicated with an (f). The cross-correlation methods are shown for their direct (1-hop) neighbors and their 10th order neighbors (10-hops).

	SD	NCC-1	NCC-10	NDCC-1	NDCC-10
S1	0.69	0.82	0.40	0.85	0.44
S2	1.26	3.16	0.89	2.11	1.08
S3	1.63	3.07	1.06	2.09	1.29
S1 (f)	1.27	1.31	0.88	1.44	0.98
S2 (f)	2.73	4.55	1.94	3.73	2.47
S3 (f)	2.64	4.12	1.83	3.37	2.31

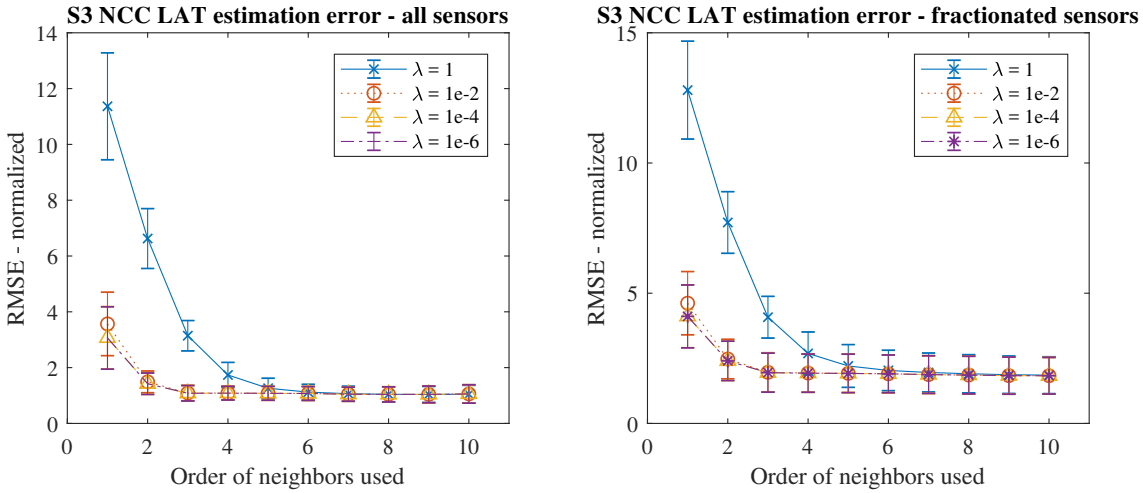


Figure 5.11: The RMSE of NCC in **S3** is shown here with different regularization parameters λ . The error bars indicate the standard deviation. On the left the error on all electrodes is taken, on the right only the fractionated electrode signals are taken into account.

5.1.3. Dependence on regularization

In Section 4.4 the methods of converting lags between pairs of electrodes to LATs was discussed. In the results shown up to now in this chapter all have been obtained using the SVD method discussed there.

In the regularized least squares method, the parameter λ is used during the conversion of relative lag to absolute times. The influence of the regularization parameter is shown in Fig. 5.11 with the mean RMSE on the set **S3**, as an example.

Using a smaller values for λ makes the LAT estimates converge. These LATs for small values of λ are also the estimates found when using the SVD pseudo-inverse method. It is also interesting to see the value of λ does not make a great difference anymore for higher P .

Conclusions For these simulations the regularized least squares method of obtaining the LATs performs as expected, as reducing the amount of regularization makes the estimate converge to those estimated using an SVD pseudoinverse method.

5.1.4. Comparison with gradient method

The spatial gradient (SG) method is also compared to the SD and NCC method. This method uses the derivative in space instead of in time and was described in Section 2.4.5. The resulting LATs are compared to that of SD, NCC-1 and NCC-10 for the **T** and **S** simulations.

The resulting RMSE for data sets **T1**, **T2**, **T3** is shown in Table 5.3. It can be observed that the SG method sometimes performs better than the SD method, but never better than the NCC method using 10th order neighbors.

The mean RMSE for data sets **S1**, **S2**, **S3** is shown in Table 5.4. On these simulations the SG method on average performs worse than the SD method, although their results are close. The NCC method with the bigger connectivity performs better than both of them again.

Conclusions The results from using the spatial gradient method indicate it has no clear advantage over the steepest deflection method. As the SD method has performed worse than the higher order neighbor NCC method, the SG method also performs worse.

5.1.5. Ignoring close neighbors

Previous results have shown improvement in cross-correlation LAT estimation when adding the delays of higher order neighboring pairs of electrodes. Now performance on simulated data will be examined when using only the further away pairs, so ignoring the delay estimates from more directly neighboring nodes.

First NCC is examined when using only pairs of nodes exactly P hops away and not the node pairs closer to each other on the grid. This then only uses the links present in $\Xi^{(P)}$ that are not present in $\Xi^{(P-1)}$. This is then called the single hop-order normalized cross-correlation (SNCC) method.

Table 5.3: The RMSE in milliseconds of the different methods for the special blocking shape data sets is shown, calculated for all electrodes and for only fractionated electrodes, indicated with an (f). The NCC method is now compared to the spatial gradient (SG) method. The NCC method is shown for their direct (1-hop) neighbors and their 10th order neighbors (10-hops).

	SD	NCC-1	NCC-10	SG
T1	2.41	3.00	1.27	2.66
T2	11.54	32.17	5.26	9.99
T3	0.93	10.31	0.49	4.01
T1 (f)	8.66	6.60	2.41	8.39
T2 (f)	27.69	40.08	12.46	23.74
T3 (f)	3.44	3.34	0.87	15.55

Table 5.4: The mean RMSE in milliseconds for the 10 simulations for sets **S1**, **S2** and **S3** is shown, calculated for all electrodes and for only fractionated electrodes, indicated with an (f). The NCC method is now compared to the spatial gradient (SG) method. The NCC method is shown for their direct (1-hop) neighbors and their 10th order neighbors (10-hops).

	SD	NCC-1	NCC-10	SG
S1	0.69	4.57	0.40	0.92
S2	1.26	5.68	0.89	1.58
S3	1.63	6.58	1.05	1.63
S1 (f)	1.27	5.28	0.89	1.62
S2 (f)	2.73	7.23	1.95	2.96
S3 (f)	2.64	7.72	1.83	2.79

Two examples of performance are given on two types of simulated data. The normalized RMSE (normalized on SD again) for set **T1** is shown in Fig. 5.12. The mean normalized RMSE for the 10 iterations of **S3** is also shown in Fig. 5.13. These sets are chosen as an example to give representative information about the performance of this method.

The results for the special shape set **T1** in Fig. 5.12 shows an interesting pattern. Only using pairs exactly P hops away (SNCC) seems to show improved performance over the regular NCC method for P between 2 and 8. Especially looking at the fractionated electrodes, this can improve the LAT estimates. The estimates of SNCC for the highest P then fail to further improve. This also has to do with the electrode being only a 11×11 array. For $P = 10$ the center electrode only has four links, to the very corners of the array, making LAT estimation more difficult for that electrode.

The results for the 10 iterations of **S3** in Fig. 5.13 show a quite consistent pattern in the case of using all electrodes and also when only looking at the fractionated electrodes. The SNCC method performs slightly worse than regular NCC, except for $P = 2$. This shows there is some benefit in using all of the links instead of only the higher order ones in these simulations. This can be said with the side note that when using second order neighboring nodes as pairs it does seem better to remove the direct links between neighboring cells in these simulations.

Another method to examine the influence of using close pairs versus distant pairs of nodes is also tested. In this method the 10th order neighbors are used, and step by step the first Q -hop connections are removed with Q going from 0 to 9. So this uses the links present in $\Xi^{(10)}$ that are not present in $\Xi^{(Q)}$.

Again two examples of performance on sets given on simulated sets **T1** and **S3**. The normalized RMSE for set **T1** is shown in Fig. 5.14 and the mean RMSE for the 10 iterations of **S3** is shown in Fig. 5.15.

The results on the special blocking shape in Fig. 5.14 shows a very constant RMSE when looking at all electrodes, up until $Q = 6$ when the performance starts to degrade somewhat. On the fractionated electrodes there is a slight performance edge when excluding the lag estimates of closer neighbors, but it does not improve the performance over the whole array.

In Fig. 5.15 the resulting performance on the simulated fibrosis-type tissue seems to indicate there is some performance loss when eliminating electrode pairs that are closer from the lag estimation in general. This would indicate there is a benefit on average to including all the lag estimates between all pairs.

From all of these experiments it can be observed that using the estimated delays from two nodes that are close can degrade the performance in certain cases. This effect is visible in the **T** sets and is most noticeable when looking at the electrodes with fractionated signals. This would suggest that it can be beneficial to only use higher order neighbors to estimate the LATs, when heavy distortions of the regular shape of the electrogram are observed. The distortion of the regular morphology then makes Eq. (4.1) not hold, the electrogram

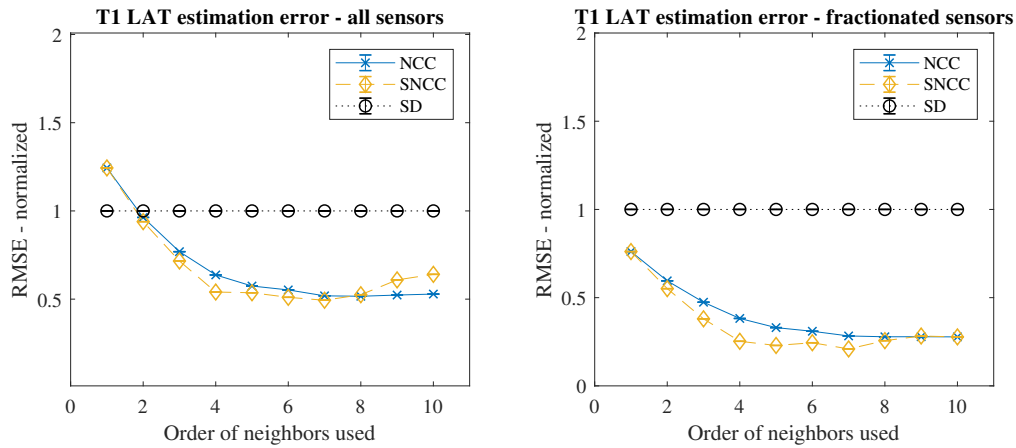


Figure 5.12: The normalized RMSE of NCC in **T1** is shown here in comparison with SNCC, which only uses lags of electrodes exactly P hops away, not less than P hops. On the left the error on all electrodes is taken, on the right only the fractionated electrode signals are taken into account.

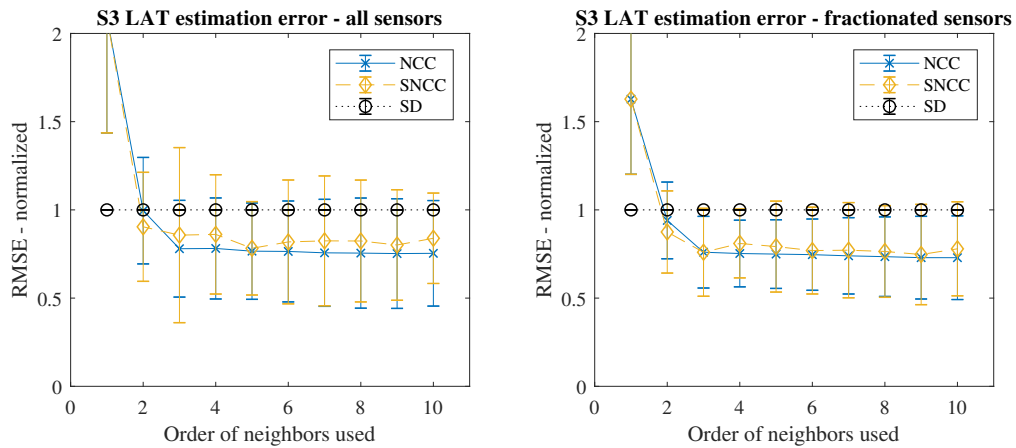


Figure 5.13: The normalized mean RMSE of NCC in **S3** is shown here in comparison with SNCC, which only uses lags of electrodes exactly P hops away, not less than P hops. The error bars indicate the standard deviation. On the left the error on all electrodes is taken, on the right only the fractionated electrode signals are taken into account.

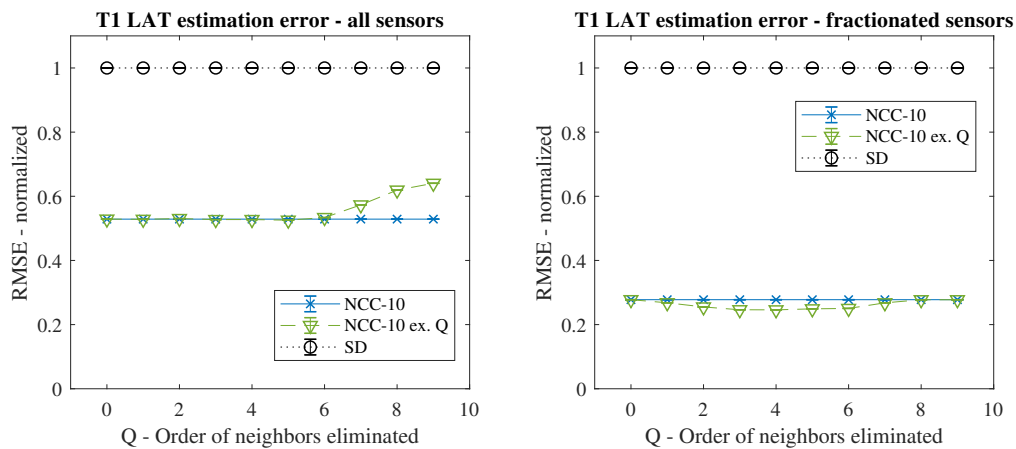


Figure 5.14: The normalized RMSE of NCC-10 in **T1** is shown here in comparison with NCC-10 where the neighbors the first Q hops away are not used. On the left the error on all electrodes is taken, on the right only the fractionated electrode signals are taken into account.

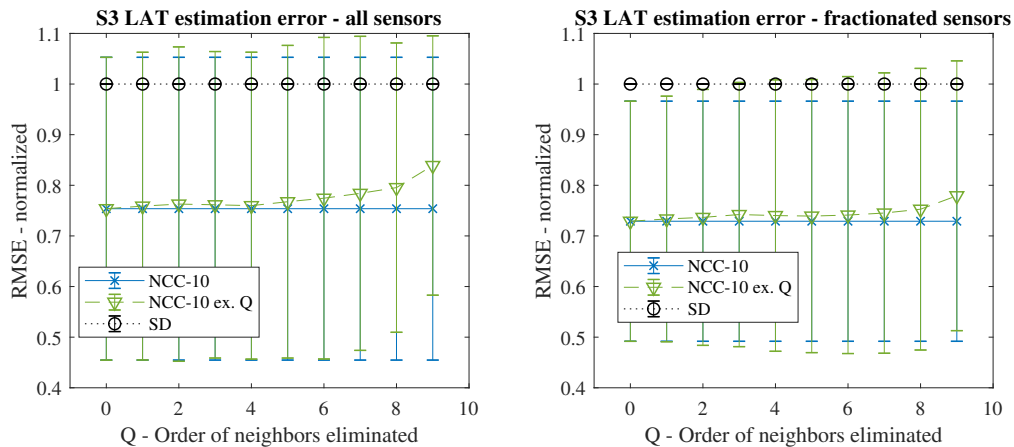


Figure 5.15: The mean normalized RMSE of NCC-10 in **S3** is shown here in comparison with NCC-10 where the neighbors the first Q hops away are not used. The error bars indicate the standard deviation. On the left the error on all electrodes is taken, on the right only the fractionated electrode signals are taken into account.

ϕ_i is not similar anymore to the standard electrogram ϕ_0 , giving

$$\phi_i(k) \neq \alpha_i \phi_0(k - \tau_i) + n_i(k). \quad (5.1)$$

These distortions might show up in roughly the same manner in two neighboring electrodes, making them correlate in an erroneous way. If they are only correlated with electrograms further away these distortions may correlate less and thus give an improved estimate of the delay through cross-correlation.

Conclusions Leaving the delays estimated between close neighbors out when estimating the LATs seems to not directly improve performance over all electrodes when looking at more realistic simulations. It also does not make the performance much worse. For electrograms that substantially differ in morphology from the standard electrogram due to distortions, it can potentially be beneficial.

5.1.6. Combining steepest deflection and cross-correlation

In Section 4.4.6 a method to combine the SD estimates of the activation times and the lag estimates of the NCC method was described. The RMSE of this method will be shown on **T1** and **S3** to give examples of the performance.

The SD observations are combined with NCC- P observations where P is the order of neighbors used, similar to the previous results shown. The performance is shown with no difference in weighting ($w = 1$) and with a weighting of $w = \frac{1}{10} \frac{L}{M}$, where L is the amount of links in $\Xi^{(P)}$ and M is the number of electrodes.

The resulting RMSE normalized on the error of SD for set **T1** is shown in Fig. 5.16. It can be observed that the combination methods perform better than both SD and NCC separately for low P . For higher P values the unweighted combination SD-NCC gives performance similar to the NCC method, the weighted method WSD-NCC starts to perform worse than the NCC method. The mean normalized RMSE for set **S3** is shown in Fig. 5.17. About the same performance characteristics of the combination methods can be observed, albeit less prominently.

To show what happens with different weights and to try and maximize performance, the combination of SD and NCC-10 is done while varying the weight w from a small to a large value. The normalized RMSE for different weights on **T1** is shown in Fig. 5.18. The error with a low weight converges to that of NCC-10, and with higher weights the error increases and goes to the level of SD. The mean normalized RMSE for **S3** for different weights is shown in Fig. 5.19. The difference here is that there seems to be a weighting value of around $w = 5$ where the combination performance is ever so slightly better than the NCC-10 performance. In this case the ground truth is known and the optimal weighting value can be observed. For clinical data this truth will not be available and it will have to be estimated.

Conclusions For a low P , so only using the cross-correlation between relatively close electrodes, the performance when combining SD and NCC can be better than the methods separately. For a higher P the performance advantage diminishes. There might be a little performance gain to be had, however the right balance

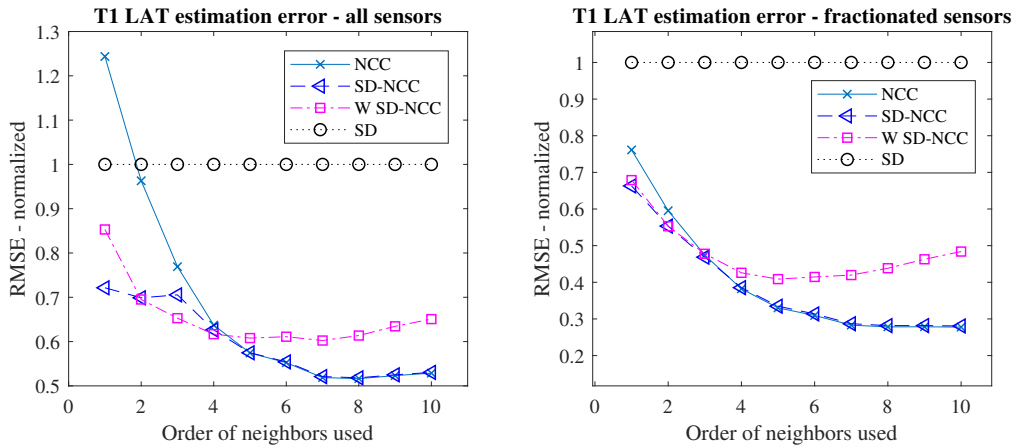


Figure 5.16: The normalized RMSE of SD and NCC-10 in T1 is shown here in comparison with the weighted combination method of SD and NCC-10. On the left the error on all electrodes is taken, on the right only the fractionated electrode signals are taken into account.

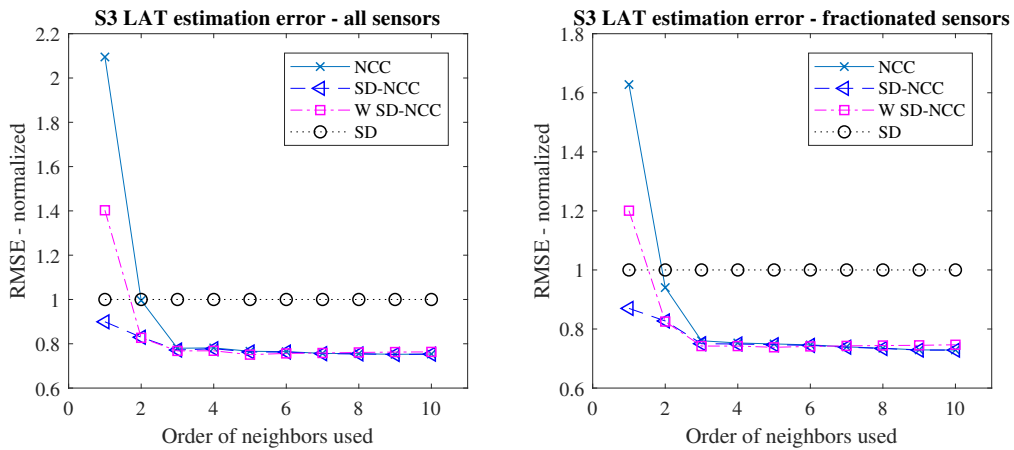


Figure 5.17: The mean normalized RMSE of NCC in S3 is shown here in comparison with its combination with SD (SD-NCC), and the weighted combination of both (W SD-NCC). On the left the error on all electrodes is taken, on the right only the fractionated electrode signals are taken into account.

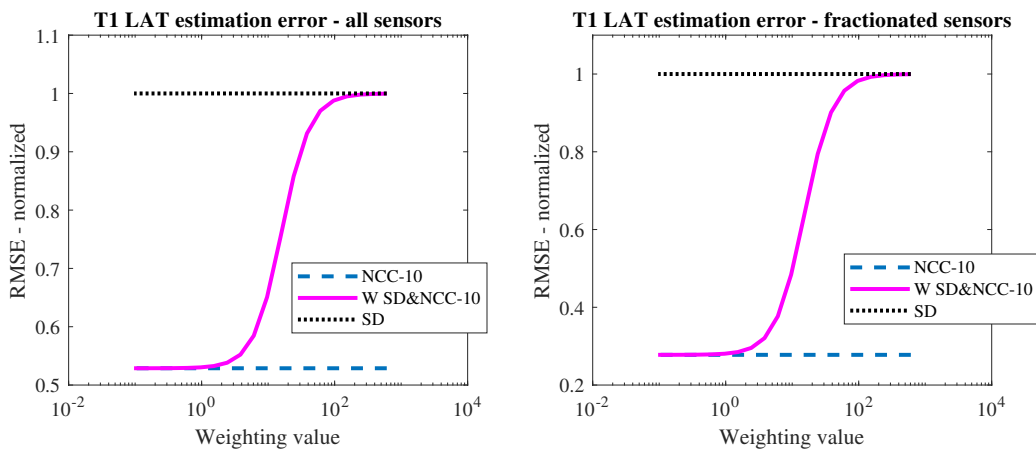


Figure 5.18: The RMSE of SD and NCC-10 in T1 is shown here in comparison with the weighted combination method of both. The performance for different weighting values w (on the x-axis) is shown. On the left the error on all electrodes is taken, on the right only the fractionated electrode signals are taken into account.

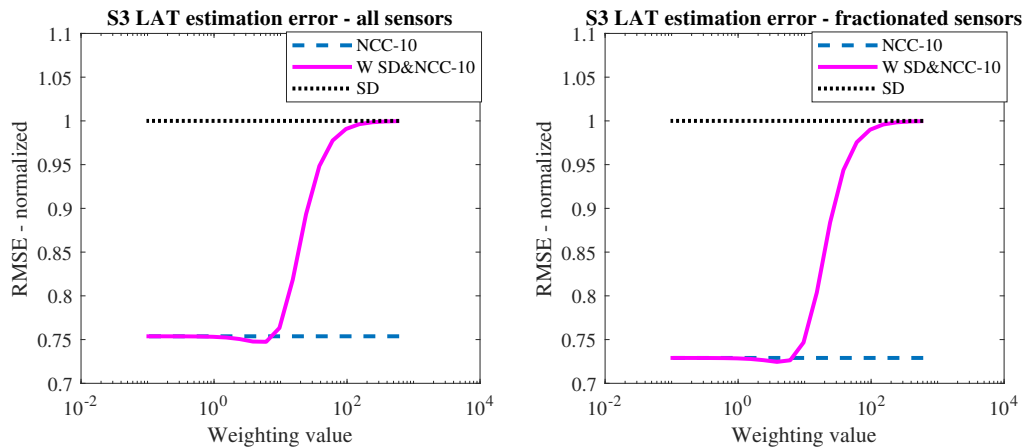


Figure 5.19: The mean normalized RMSE of NCC-10 in **S3** is shown here in comparison with the weighted combination method of both. The performance for different weighting values w (on the x-axis) is shown. On the left the error on all electrodes is taken, on the right only the fractionated electrode signals are taken into account.

must be struck when weighting the observations. Determining the correct weighing might prove difficult if the ground truth is not known.

5.1.7. Estimation of error covariance matrix

The previously shown results were all obtained without estimation of the error covariance matrix \mathbf{C} of the delays, before transforming those to absolute times using a least squares method. The OLS estimation method was thus used in all previous experiments as this does not use this information, as it assumes equal variances and independent errors.

In Section 4.4.2, a method was shown to estimate a diagonal matrix \mathbf{C} using the squared residuals, which we will call the *unstructured* method of variance estimation here. In Section 4.4.3, another method was proposed that assumed there to be more structure in the estimated variances, which we will simply refer to as the *structured* method. The covariance matrix is estimated using the residuals of the OLS method, as was explained in the previous chapter. The LATs are then estimated with these covariance matrices using the GLS estimator. No further iteration is done, as this showed no guarantee to improve the LAT estimates, so the residuals are only calculated once. Both methods are tested on the **T** and **S** sets.

First, the mean of the normalized RMSE is shown on the **T** sets in Fig. 5.20, to give an example of the performance. Looking at all electrodes, the methods perform somewhat better than the regular NCC method, although the difference becomes minimal for higher P . Interestingly, they perform slightly worse when only looking at fractionated electrodes.

The mean normalized RMSE is also shown for the **S3** sets in Fig. 5.21. The differences here are much smaller. The unstructured estimation method of \mathbf{C} seems to perform worse than the regular NCC method for higher P .

The RMSE results for the **T** sets are shown in Table 5.5, the mean RMSE for the **S** sets is shown in Table 5.6. The unstructured covariance estimation works fine on **T1** but lacks performance on the other sets. Looking at the performance on all electrodes the structured covariance estimation could give a very slight performance improvement for NCC-10.

Conclusions Covariance estimation for use in a GLS estimator can improve performance of LAT estimation for cross-correlation for lower values of P . For higher values of P the performance difference is small. However a slight performance increase can be had on average when assuming a structure in the covariance matrix related to the underlying nodes. The covariance has been estimated with using the residuals of the OLS estimate, finding other ways to estimate covariance might improve the performance further. The LATs estimated with the OLS method however also show good performance and GLS methods do not clearly beat them in all situations.

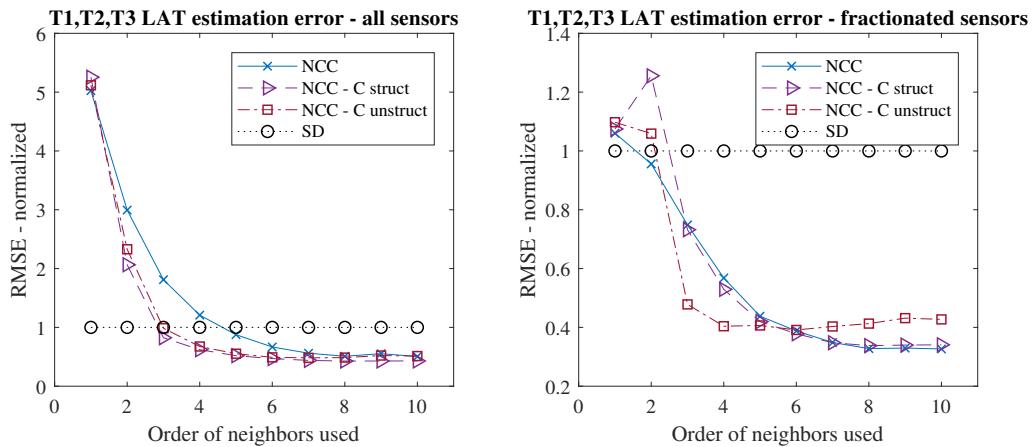


Figure 5.20: The mean normalized RMSE of NCC in the **T** sets is shown here in comparison with NCC where the covariance matrix **C** is estimated. Both the unstructured and structured estimation of **C** is done and shown. On the left the error on all electrodes is taken, on the right only the fractionated electrode signals are taken into account.

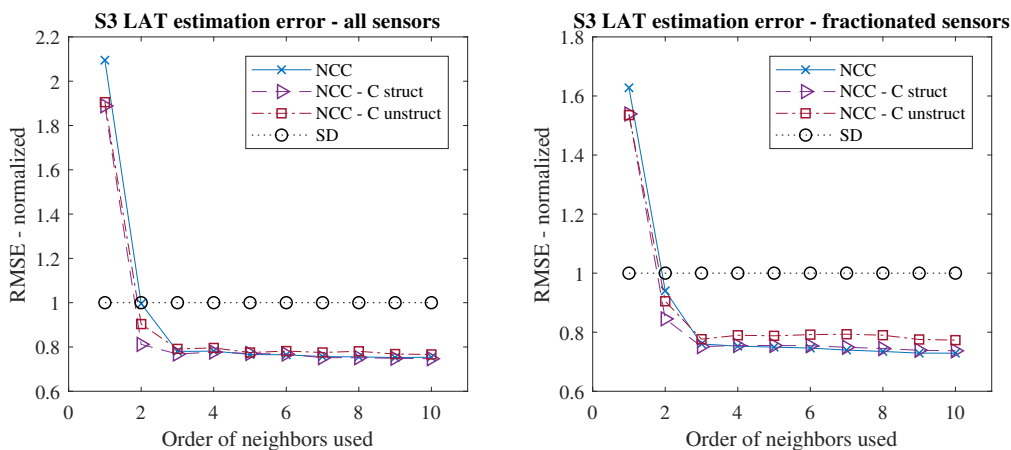


Figure 5.21: The mean normalized RMSE of NCC-10 in the **S3** sets is shown here in comparison with NCC where the covariance matrix **C** is estimated. Both the unstructured and structured estimation of **C** is done and shown. On the left the error on all electrodes is taken, on the right only the fractionated electrode signals are taken into account.

Table 5.5: The RMSE in milliseconds for the sets **T1**, **T2** and **T3** is shown, calculated for all electrodes and for only fractionated electrodes, indicated with an (f). The regular NCC-10 method is now compared to method with structured covariance estimation (NCC-10 C struct) and with unstructured covariance estimation (NCC-10 C unstruct)

	SD	NCC-1	NCC-10	NCC-10 C struct	NCC-10 C unstruct
T1	2.41	2.99	1.27	1.27	1.26
T2	11.54	32.16	5.26	5.37	5.46
T3	0.93	10.30	0.49	0.27	0.50
T1 (f)	8.66	6.59	2.41	2.35	2.27
T2 (f)	27.69	40.07	12.46	12.88	13.10
T3 (f)	3.44	3.34	0.87	0.98	1.88

Table 5.6: The mean RMSE in milliseconds for the 10 simulations for sets **S1**, **S2** and **S3** is shown, calculated for all electrodes and for only fractionated electrodes, indicated with an (f). The regular NCC-10 method is now compared to method with structured covariance estimation (NCC-10 C struct) and with unstructured covariance estimation (NCC-10 C unstruct).

	SD	NCC-1	NCC-10	NCC-10 C struct	NCC-10 C unstruct
S1	0.69	0.81	0.40	0.39	0.39
S2	1.26	3.15	0.89	0.87	0.94
S3	1.63	3.06	1.06	1.04	1.08
S1 (f)	1.27	1.30	0.88	0.88	0.89
S2 (f)	2.73	4.55	1.94	1.94	2.04
S3 (f)	2.64	4.11	1.83	1.85	1.95

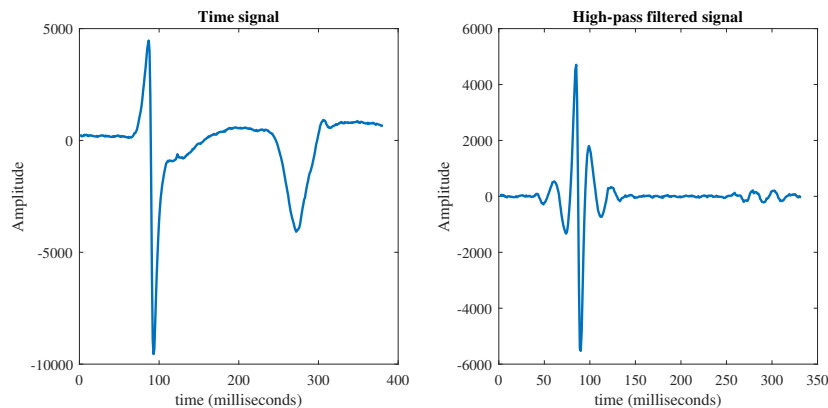


Figure 5.22: On the left an atrial electrogram is shown, where the initial atrial activity comes first and the ventricular activity afterwards is also shown. On the right this electrogram is shown when highpass filtered.

5.2. Experiments on real-world, clinical data

The clinically recorded, real-world mapping data as described in Section 3.2 can be evaluated using the same methods used as on simulated data. However, the true activation times of the cells are not available for this data. The resulting LATs estimated can then be compared to each other, but no direct measure of their accuracy is available.

The LATs of the clinical data will be estimated using SD and NCC methods to compare a currently standard practise with the method that was found to perform best on the simulated data. NCC-10 with OLS estimation will be used, although these estimated LATs do not significantly differ from the NCC-9 or NCC-11 estimates.

5.2.1. Time windowing

In Section 4.5, a method was described to obtain time windows from the recorded data. This method used highpass filtered data to detect the activation of the cells and remove unwanted disturbances, like the depolarization of the ventricles. For the recorded atrial electrograms an equiripple filter was used, designed in MATLAB with a 7.5 Hz stopband frequency, a 15 Hz passband frequency and a stopband attenuation of 60 dB. An example of the effect of this highpass filtering is shown in Fig. 5.22.

A window of **200 ms** is sought for each activation, so $N_{window} = 200$ samples, and the step size was set at $N_{window} = 50$ samples. The threshold to determine if a window was to be detected as active was set at $\eta = 0.3$, so if the signal had a maximum amplitude larger than 30% of the maximum amplitude of the electrogram the window was marked as active.

5.2.2. Regular sinus rhythm

The first data set that will be used was recorded from a patient undergoing coronary artery bypass surgery. This data set was recorded from the left pulmonary vein site, on the left atrium. From the 5 beats present in the 5-second recording of sinus rhythm from the patient, five time windows of 200 ms were extracted. The third beat, so the third time window, is evaluated here.

First, the total activation map of this beat is shown for the SD and NCC-10 method. The maps can be seen in Fig. 5.23. It can be observed there are quite some differences in estimated LATs. A few of those differences

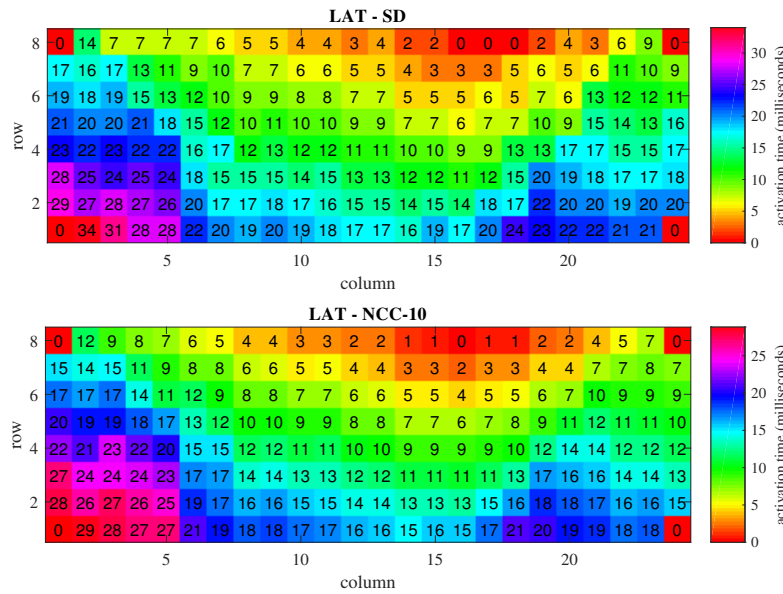


Figure 5.23: On top the estimated activation times in milliseconds with the steepest deflection (SD) method are shown. On the bottom the estimate times are shown for the normalized cross-correlation method using 10th order neighbors (NCC-10).

will be highlighted.

Looking at the 20th column, the 4th and 5th electrode are highlighted in Fig. 5.24. There it can be observed that the SD method sees an 8 ms difference in activation time between these two electrodes. The NCC-10 method sees only a 3 ms delay between these electrodes.

The two electrograms corresponding to these electrodes are also shown. They are shown separately in the upper plots, and they are shifted in the lower plots. In the lower plots the lag detected by each method is compensated for, so the signals should be synchronized and their activation time should be simultaneous. Shifting them by their time difference can give an indication if the delay estimated between them is plausible.

An obvious difference can be seen between the two methods from Fig. 5.24. When the signals are overlapped, both methods have different interpretation of how they should be synchronized to let their LATs coincide. Without any further knowledge about the ground truth available the correctness of the methods cannot be validated directly, unfortunately.

Looking at another part of the array, in the 8th row, there are 4 electrodes highlighted in Fig. 5.25. There, the SD method shows the electrodes all have an estimated LAT at the same exact moment. The NCC-10 method estimates there is a 1 ms delay between all the electrodes.

The time series signals are shown on the right in Fig. 5.25. The upper plot depicts the signals not shifted in time, as the SD method estimates these signals all have their activation time at exactly the same time. On the bottom right of Fig. 5.25 the signals are shown when shifted according to the NCC-10 method's estimated lag. There the signals are synchronized according to its estimate of their activation time. The estimates from both methods are again clearly different.

5.2.3. Signals with disturbances

The second data set that will be investigated is from a patient with a history of paroxysmal AF. This patient was also undergoing coronary artery bypass surgery. The data was recorded from the left atrium during SR and a single beat, the first of the recorded beats, will be evaluated.

The estimated LATs for SD and NCC-10 are shown in Fig. 5.26. In the right bottom corner the signal was especially chaotic, which might be because the contact with the atrial tissue was weak. That corner will be ignored and other locations in the array are compared.

In Fig. 5.27 the signals of two electrodes from row 7 are compared, those at column 11 and 12. The SD method detects a difference of 9 milliseconds in LAT. The NCC-10 method detects a difference of 4 milliseconds for the same two electrodes. The signals are shifted according to those delays between them that were estimated and are also shown in their shifted form. Because the point of steepest deflection is at the begin-

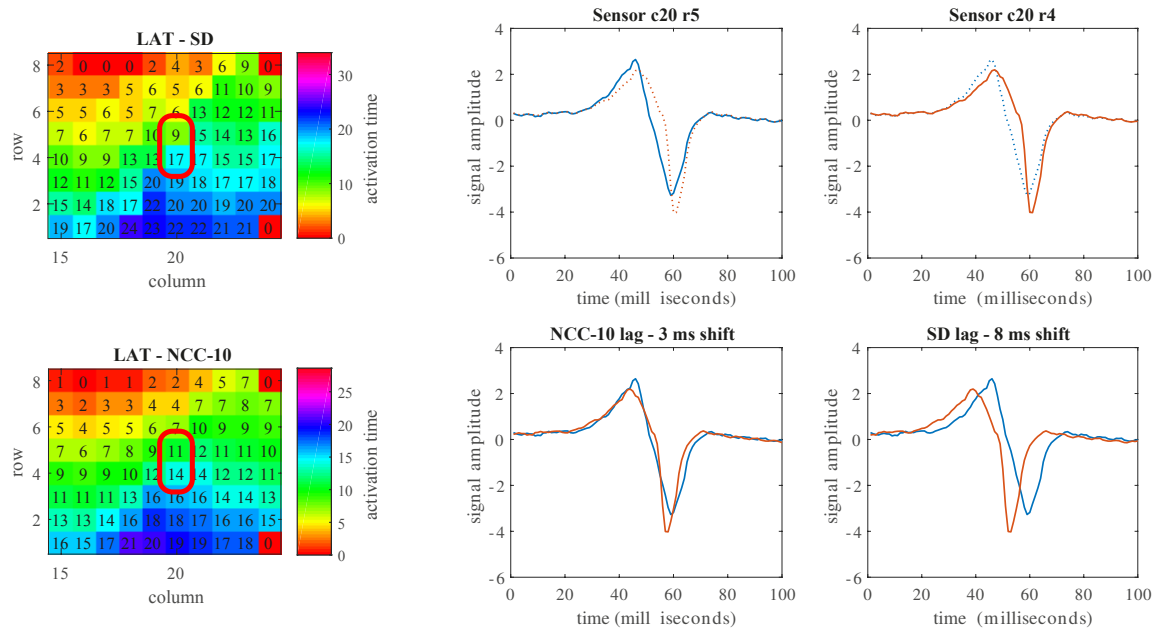


Figure 5.24: On the left side the LAT maps in milliseconds are shown for SD and NCC-10, for column 15 to 24 of the electrode array. On the right the signals from the highlighted electrodes are shown and compared.

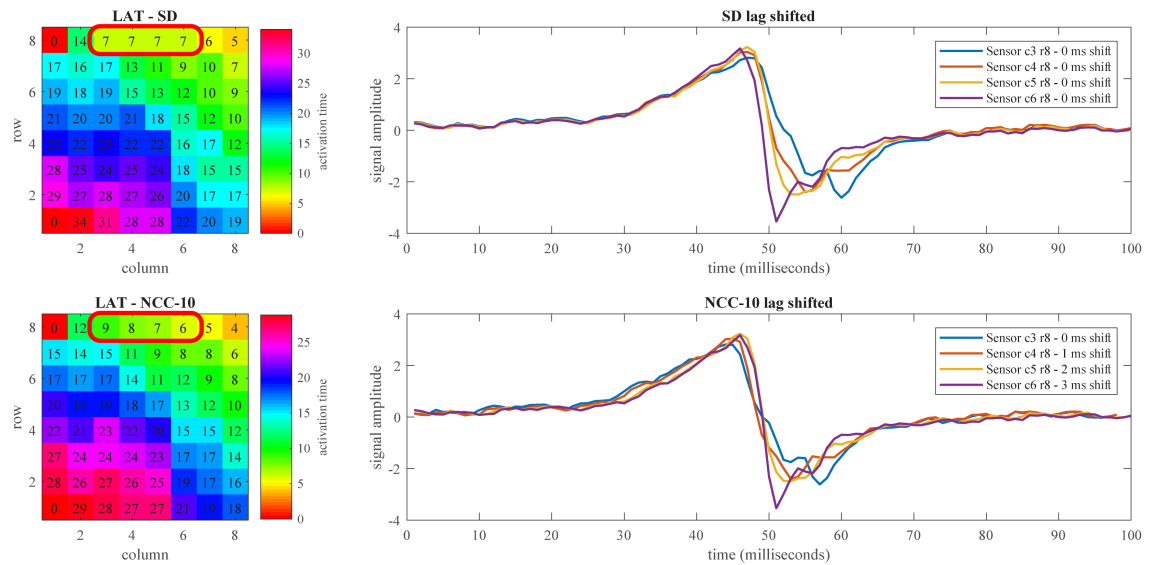


Figure 5.25: On the left side the LAT maps in milliseconds are shown for SD and NCC-10, for column 1 to 8 of the electrode array. On the right the signals from the highlighted electrodes are shown and compared.

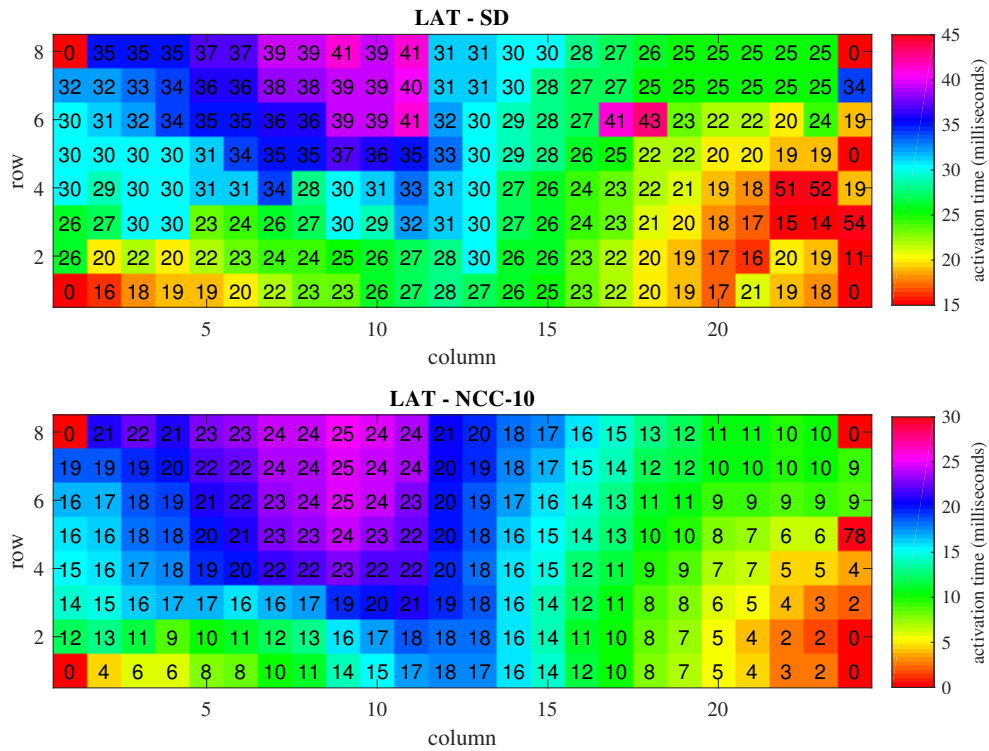


Figure 5.26: The LAT maps are shown in milliseconds for SD and NCC-10, for the first beat recorded on the left atrium during SR.

ning of the downward slope in one electrode and at the end of the slope in another electrode, the SD method detects a long delay. The NCC method tries to match the entire signals to each other and to many other signals in the array, and it detects a much lower lag.

Another set of 4 electrodes is compared. This time from row 6, column 16 to 19. The estimated LATs and the signals are shown in Fig. 5.28. The interesting thing here is the SD method detecting a much later LAT for the middle two electrodes. Looking at the shifted signals for SD and NCC-10 it can be observed that the SD method sees a second, smaller deflection as the LAT for the electrodes from column 17 and 18. The NCC method focuses on the bigger deflections.

Lastly for this beat, four other electrodes were compared. This time four electrodes from column 9 are taken, from row 2 to row 5. The activation maps and electrode signals are shown in Fig. 5.29. Taking the electrode from row 2 as a reference, the SD method detects lags of 5 ms, 5ms, and 12 ms for the other electrodes. The NCC-10 method detects lags of 4 ms, 7 ms, and 9 ms for those same electrodes.

The unshifted signals and the shifted signals according to those estimated lags are shown on the right in Fig. 5.29. The signals from the electrodes differ substantially in morphology, so overlapping them to see where they match becomes even more difficult. The estimates of the delay between the LATs of different locations in the array are again clearly different. The SD method estimates a lag of 7 ms between the electrodes in row 4 and 5 of column 9, the NCC-10 method estimates it is only a 2 ms lag.

5.2.4. Multiple wavefronts

Another data set that can be evaluated is that of another patient with paroxysmal AF. This patient was undergoing surgery for mitral valve disease. The first beat recorded from the left atrium during SR investigated here. In this beat there were parts of the array that clearly measured multiple activation waves.

The LATs for SD and for NCC-10 are shown on the right in Fig. 5.30, for column 1 to 16. From both these estimates of the LATs it is clear there is a segment of the electrode on the lower left where the tissue activates much earlier than the part on the top right, these parts seem to be excited by separate activation waves.

Four electrodes from row 2 are investigated, from column 10 to 13. The unshifted electrode signals are shown on the right. In these electrodes there are three or even four different activations visible in all elec-

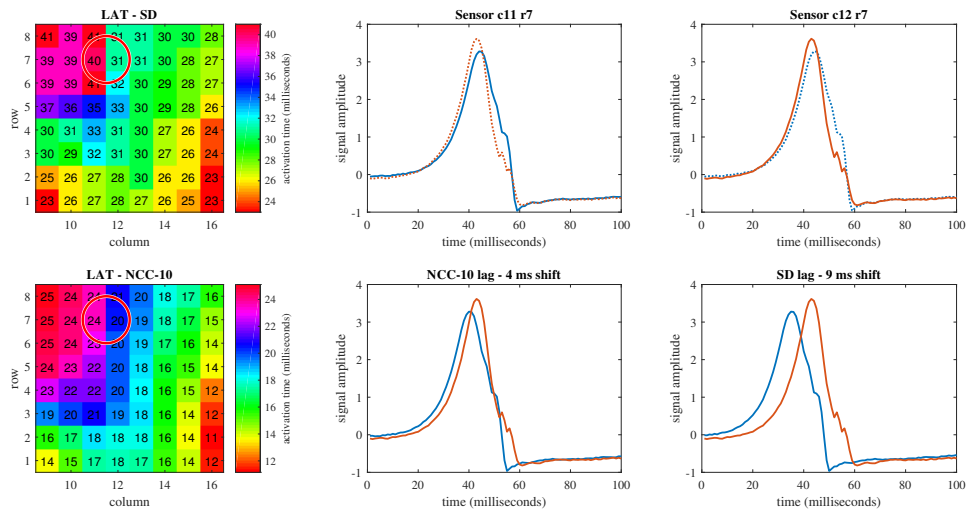


Figure 5.27: On the left side the LAT maps are shown in milliseconds for SD and NCC-10, for column 9 to 16 of the electrode array. On the right the signals from the highlighted electrodes from row 7 are shown and compared.

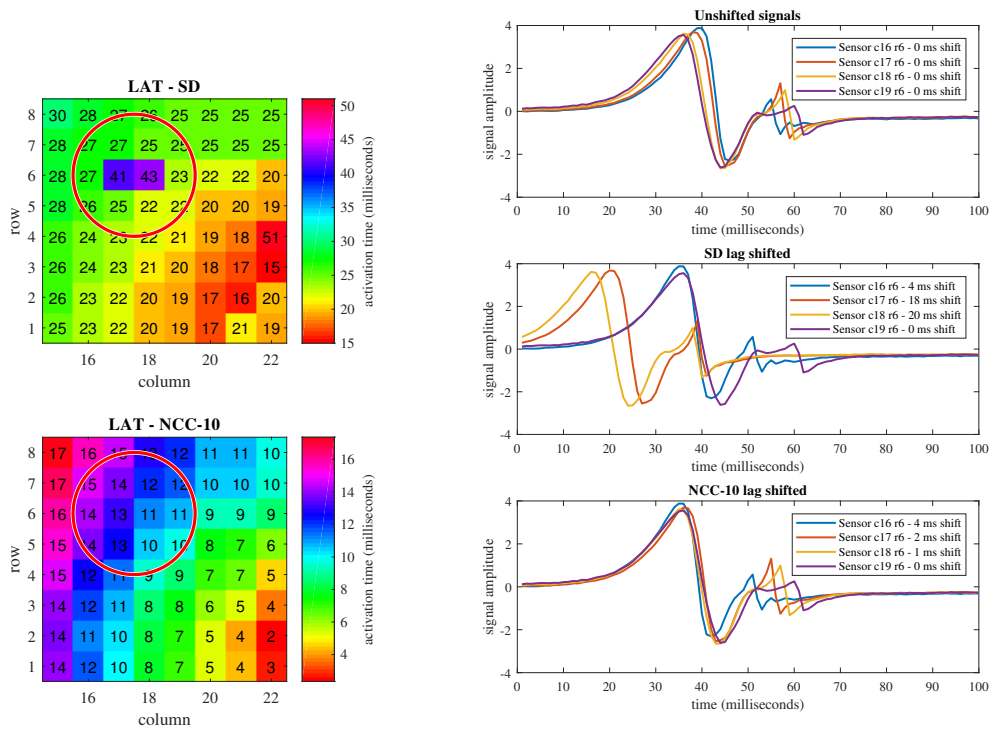


Figure 5.28: On the left side the LAT maps are shown for SD and NCC-10, for column 15 to 22 of the electrode array. On the right the signals from the highlighted electrodes in row 6 and their shifted versions are shown.

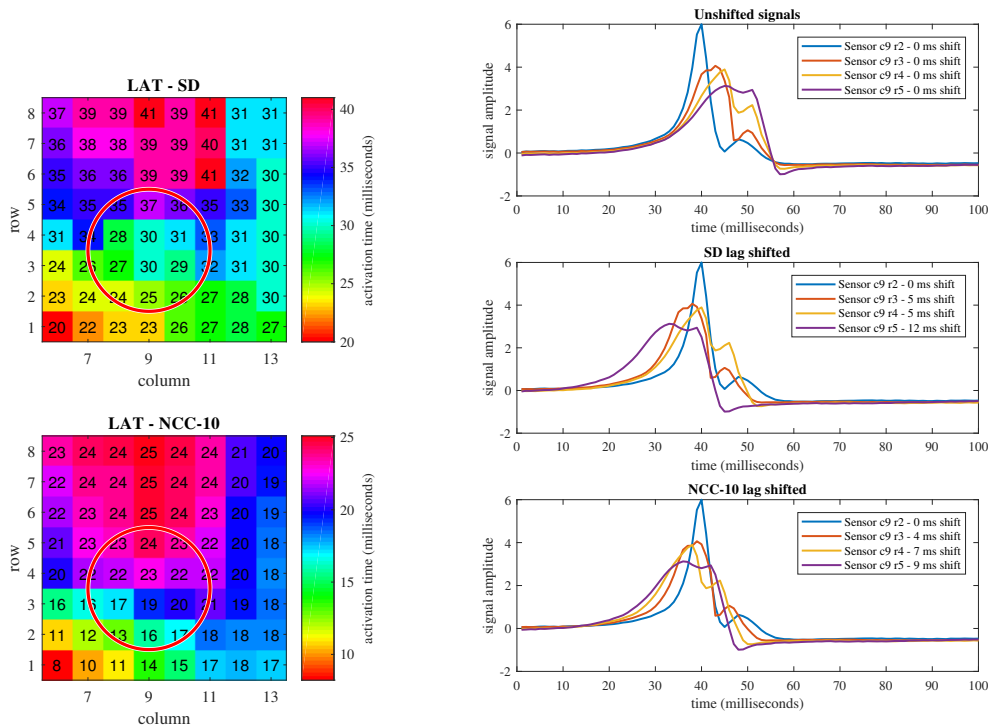


Figure 5.29: On the left side the LAT maps are shown in milliseconds for SD and NCC-10, for column 6 to 13 of the electrode array. On the right the signals from the highlighted electrodes in column 9 and their shifted versions are shown.

trodes. Shifting the electrode signals according to the estimated delays in LAT does not yield much results here as the shifted signals become hard to interpret.

The estimated times for the NCC method seem to have difficulties with the electrodes detecting all these different activation waves. Looking at the unshifted electrograms, it might be better in such cases to develop a method that can cross-correlate all the detected peaks individually, rather than try to correlate these multiple activation, spread out over 100 ms, at the same time.

Conclusions From investigating the estimated LATs on clinical data it can be observed that the cross-correlation method can provide distinctly different estimates when compared to the LAT estimates from a steepest deflection method.

For electrodes that have not measured discrete multiple activations in a short window, the cross-correlation method provides LAT estimates that show robustness to smaller disturbances and provides LAT maps that could give more information to help find accurate excitation patterns in the tissue.

For situations where there are multiple wavefronts, the cross-correlation method could have difficulties identifying which activation to focus on. It can be combined with other methods in a weighting scheme discussed before to help improve this, or the window over which the cross-correlation is done can be shortened to help identify individual propagating waves. Ideally, the time windows of the electrograms that are cross-correlated thus only contain a single wavefront.

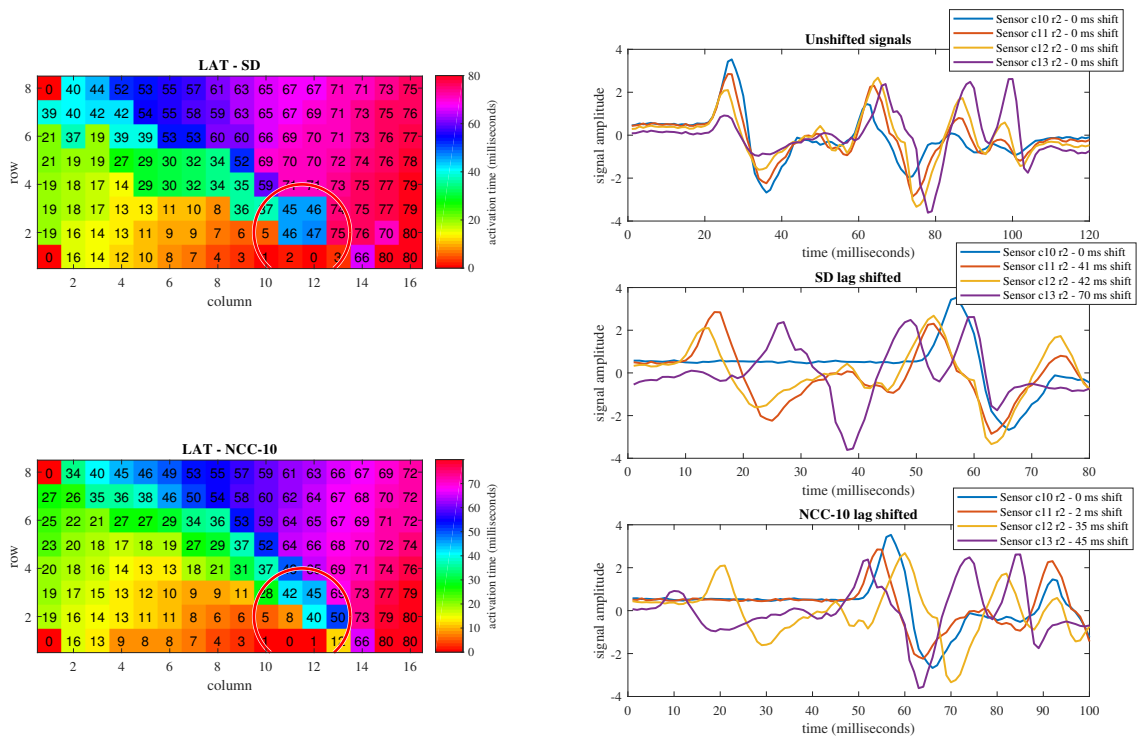


Figure 5.30: On the left side the LAT maps are shown in milliseconds for SD and NCC-10, for column 1 to 16 of the electrode array. On the right the signals from the highlighted electrodes in row 2 and their shifted versions are shown.

6

Conclusions

6.1. Summary of results

In this thesis, using cross-correlation to determine the delay between the activation time of pairs of electrodes measuring epicardial electrograms in the atria was investigated. Cross-correlation was applied to pairs of electrodes further apart, not only to directly neighboring electrodes. The obtained delay were then converted back to the local activation times and they were compared to the current accepted methods.

In Chapter 2 epicardial mapping for the human atria was introduced using an array of electrodes. A model of the action potential of the cardiac cells was discussed, which introduces the transmembrane currents that determine the measured electrogram. Several methods were introduced that use the measurements from the electrode to estimate the local activation times of the tissue underneath these electrodes.

In Chapter 3 multiple types of simulations were discussed where a 2D piece of atrial tissue with different conductive properties could be simulated. Furthermore, clinically recorded data of the atrial electrograms was introduced, where during open-heart surgery epicardial recording was done with an array of 192 electrodes.

In Chapter 4 a framework is first presented which uses a grid graph to define the spatial relations of the electrodes. Using the neighboring electrodes defined by this graph, higher order neighbors could be then defined as pairs of electrodes with a higher number of hops between them in the grid graph. Cross-correlation of measured signals could then be done between the higher order neighbors and not only the direct ones. Additionally, multiple methods were described to convert the delays between pairs of electrodes to absolute activation times. Estimation of the error covariance of the observed delays was presented for different error models, with and without the structure of the graph taken into account.

In Chapter 5 experiments with simulated data were used to compare the performance of several methods on different types of conduction patterns in atrial tissue. Experiments with clinical data were done to validate the functionality and observe differences between methods in a real-world setting.

Cross-correlation over higher order neighbors was first applied to simulated data, and the performance of the LAT estimates was observed to improve for increasing orders of neighboring pairs used. The results were compared to those obtained using steepest deflection and spatial gradient methods. Cross-correlation over higher order neighbors out-performed them on the simulated tissue. Further tests were done to see if results could be improved when observations were left out or combined with information from the steepest deflection. For cross-correlation methods only using pairs close together, this could improve performance. However, when many further away pairs were used, improvements on the estimated activation times were minimal. Estimation of the covariance was also done, yielding possible improvements in some cases.

In the experiments on data recorded from real-world patients the cross-correlation and steepest deflection estimates of activation times were compared. The estimates showed distinct differences in many situations. When the recorded electrograms' morphologies were reasonably standard for signals recorded in SR, with sometimes smaller disturbances, the cross-correlation over higher order neighbors was found to give estimates that were certainly probable. When the morphologies become more complex and multiple wave-fronts are detected by a single electrode the analysis became more difficult.

The results from the experiments clearly showed the advantages of cross-correlation over higher order neighbors when determining the delay between local activation times. The estimates of the absolute activa-

tion times from those lags were superior in simulation to methods using only close neighbors. Some other observation about the tested methods are discussed below.

Increasing P in NCC-P Increasing the order of neighbors used to in the cross-correlation methods improves the activation time estimation. The improvements do diminish at a certain point, and adding even more distant pairs does not help significantly anymore. Excluding electrode pairs that are close, so only using pairs with greater distances between them, can have a positive impact in some situations, which is also an interesting result to note.

NDCC vs NCC Using the derivative of the electrograms to perform cross-correlation on seems to give better results than using the time series data when only using direct neighbors (NDCC-1 vs NCC-1). When using higher order neighbors its advantage goes away and using the derivative performs worse in all tests. The regular time-domain cross-correlation seems to be able to better match the signals using their time-domain morphology.

NCC vs SD On the results using simulated data, the cross-correlation over higher order neighbors outperforms the steepest deflection method of estimating local activation times. Combining them both yielded improved estimates when using only close neighbors in delay estimation, however this improvement seemed to diminish with using higher order neighbors. The combination scheme could still be useful if it would be dependent on the type of electrograms present to play to the strengths of the individual methods.

Covariance estimation The ordinary least-squares estimation of the activation times from the observed delays was tested against generalized least-squares methods where the covariance matrix was estimated. Covariance estimation could improve the results for when using only close neighbors, however the improvements became negligible when higher order neighbors were taken. The ordinary least-squares estimate of the activation times seems difficult to improve upon.

Clinical signals In experiments on clinical signals, substantial differences arise in estimated activation times, most noticeably when comparing the differences in estimated times between neighboring electrode locations. To provide the most probable improvements in epicardial mapping procedures for the atria, cross-correlation could be a candidate. If the cross-correlation methods examined in our experiments are used where they are strong, in areas where there is a clear single activation wave with some smaller disturbances, the possibilities of improve estimates seem to be there.

6.2. Future work

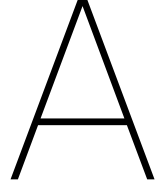
More research must be done into the application of cross-correlation for LAT estimation in epicardial atrial mapping. The performance increase when using the estimated lags between distant pairs was shown for a single type of array. The influence of higher or lower densities of electrodes can be investigated to see if the performance benefit increases or decreases.

The properties of the individual electrograms that contribute to proper estimates of the delay should also be investigated, to see if there is a property that can indicate these delays should get an increased weight when estimating the LATs. Using more real-world examples or different simulations of epicardial electrograms could help in investigated what kind of morphology of the signal is most suited for a cross-correlation estimate, and for which ones a steepest deflection estimate could be given more weight if their information would be combined.

For optimizing the cross-correlation LAT estimation performance, it is important that its time window is small enough to not include multiple passing wave fronts. Isolating these windows properly then allows for the proper estimation of the propagation of the depolarization through the tissue.

Furthermore, it can be investigate how generalized cross-correlation methods such as the phase transform (GCC-PHAT) can be applied in the atrial recording. The difficulties with these methods using cross-spectral analysis during testing arose due to the significant differences in morphology of the signals.

Lastly, a benchmark test using artificial tissue where the transmembrane currents are known could benefit research into this subject. Having the information about the true physical transmembrane currents can help in understanding what happens exactly in the cardiac tissue as recorded electrograms could be recreated in a controlled setting.



CRLB derivation

The Cramér-Rao lower bound [63] for an unbiased estimator for the length M parameter vector $\boldsymbol{\tau}$ in the model

$$\mathbf{d} = \mathbf{B}^T \boldsymbol{\tau} + \boldsymbol{\epsilon} \quad (\text{A.1})$$

will be investigated, with the error $\boldsymbol{\epsilon}$ from a zero-mean multivariate Gaussian distribution with a non-singular, $M \times M$ covariance matrix \mathbf{C} , so $\boldsymbol{\epsilon} \sim \mathcal{N}(\mathbf{0}, \mathbf{C})$. The length L vector of observations is \mathbf{d} and \mathbf{B}^T is a $L \times M$ matrix. The lower bound for the variance of such an estimator is then

$$E[(\hat{\boldsymbol{\tau}} - \boldsymbol{\tau})(\hat{\boldsymbol{\tau}} - \boldsymbol{\tau})^T] \geq \mathbf{J}^{-1}, \quad (\text{A.2})$$

with \mathbf{J} the Fisher information matrix. This matrix is defined as

$$\mathbf{J} = -E \left[\frac{d^2}{d\boldsymbol{\tau}^2} \ln p(\mathbf{d}|\boldsymbol{\tau}) \right], \quad (\text{A.3})$$

with $p(\mathbf{d}|\boldsymbol{\tau})$ the probability density function of \mathbf{d} given $\boldsymbol{\tau}$. This creates an $L \times L$ matrix with entries

$$\mathbf{J} = \begin{bmatrix} -E \left[\frac{d^2}{d\tau_1^2} \ln p(\mathbf{d}|\boldsymbol{\tau}) \right] & -E \left[\frac{d^2}{d\tau_2 d\tau_1} \ln p(\mathbf{d}|\boldsymbol{\tau}) \right] & \dots \\ -E \left[\frac{d^2}{d\tau_1 d\tau_2} \ln p(\mathbf{d}|\boldsymbol{\tau}) \right] & -E \left[\frac{d^2}{d\tau_2^2} \ln p(\mathbf{d}|\boldsymbol{\tau}) \right] & \dots \\ \vdots & \vdots & \ddots \end{bmatrix}. \quad (\text{A.4})$$

The probability density function of the observations given the parameters is

$$p(\mathbf{d}|\boldsymbol{\tau}) = (2\pi)^{-\frac{L}{2}} |\mathbf{C}|^{-\frac{1}{2}} \exp(-1/2(\mathbf{d} - \boldsymbol{\mu})^T \mathbf{C}^{-1}(\mathbf{d} - \boldsymbol{\mu})) \quad (\text{A.5})$$

with $\boldsymbol{\mu} = E[\mathbf{d}]$. Taking the natural logarithm gives

$$\ln p(\mathbf{d}|\boldsymbol{\tau}) = -2L \ln(2\pi) - 2 \ln(|\mathbf{C}|) - 1/2((\mathbf{d} - \boldsymbol{\mu})^T \mathbf{C}^{-1}(\mathbf{d} - \boldsymbol{\mu})). \quad (\text{A.6})$$

Taking the derivative with respect to $\boldsymbol{\tau}$ then gives

$$\frac{d}{d\boldsymbol{\tau}} \ln p(\mathbf{d}|\boldsymbol{\tau}) = -1/2 \left(\left(\frac{d\boldsymbol{\mu}}{d\boldsymbol{\tau}} \right)^T \mathbf{C}^{-1}(\mathbf{d} - \boldsymbol{\mu}) + (\mathbf{d} - \boldsymbol{\mu})^T \mathbf{C}^{-1} \left(\frac{d\boldsymbol{\mu}}{d\boldsymbol{\tau}} \right) \right), \quad (\text{A.7})$$

when assuming $\frac{d}{d\boldsymbol{\tau}} \mathbf{C} = 0$. Taking the derivative again gives

$$\frac{d^2}{d\boldsymbol{\tau}^2} \ln p(\mathbf{d}|\boldsymbol{\tau}) = -1/2 \left(2 \left(\frac{d\boldsymbol{\mu}}{d\boldsymbol{\tau}} \right)^T \mathbf{C}^{-1} \left(\frac{d\boldsymbol{\mu}}{d\boldsymbol{\tau}} \right) + \left(\frac{d^2\boldsymbol{\mu}}{d\boldsymbol{\tau}^2} \right)^T \mathbf{C}^{-1}(\mathbf{d} - \boldsymbol{\mu}) + (\mathbf{d} - \boldsymbol{\mu})^T \mathbf{C}^{-1} \left(\frac{d^2\boldsymbol{\mu}}{d\boldsymbol{\tau}^2} \right) \right). \quad (\text{A.8})$$

The expected value is taken, and because $E[\mathbf{d} - \boldsymbol{\mu}] = \mathbf{B}^T \boldsymbol{\tau} - \mathbf{B}^T \boldsymbol{\tau} = 0$, the expression becomes

$$E \left[\frac{d^2}{d\boldsymbol{\tau}^2} \ln p(\mathbf{d}|\boldsymbol{\tau}) \right] = - \left(\left(\frac{d\boldsymbol{\mu}}{d\boldsymbol{\tau}} \right)^T \mathbf{C}^{-1} \left(\frac{d\boldsymbol{\mu}}{d\boldsymbol{\tau}} \right) \right). \quad (\text{A.9})$$

Using the fact that $\boldsymbol{\mu} = \mathbf{B}^T \boldsymbol{\tau}$, the Fisher information matrix becomes

$$\mathbf{J} = \mathbf{B}\mathbf{C}^{-1}\mathbf{B}^T. \quad (\text{A.10})$$

Its inverse is then the bound on the variance that was sought,

$$E[(\hat{\boldsymbol{\tau}} - \boldsymbol{\tau})(\hat{\boldsymbol{\tau}} - \boldsymbol{\tau})^T] \geq (\mathbf{B}\mathbf{C}^{-1}\mathbf{B}^T)^{-1}. \quad (\text{A.11})$$

B

List of Abbreviations and Symbols

\mathbf{x} Vector \mathbf{x} .

\mathbf{X} Matrix \mathbf{X} .

$X_{i,j}$ The element at index i, j of a matrix.

$\mathbf{x}^T, \mathbf{X}^T$ Transpose of vector or matrix.

$\mathbf{x}^H, \mathbf{X}^H$ Hermetian transpose of vector or matrix.

$|\mathbf{X}|$ Determinant of matrix.

$E[\cdot]$ The expected value.

Var(\cdot) The variance.

Cov(\cdot, \cdot) The covariance.

$\mathcal{N}(\mu, \sigma^2)$ A Gaussian distribution with mean μ and variance σ^2 .

$N(i)$ The set of neighbors of node i .

AA Atrial Activity.

AF Atrial Fibrillation.

AFL Atrial Flutter.

CRLB Cramér-Rao lower bound.

ECG Electrocardiogram.

FFT Fast Fourier Transform.

GLS Generalized Least Squares.

IAF Induced Atrial Fibrillation.

LAT Local Activation Time.

ML Maximum Likelihood.

NCC Normalized Cross-Correlation.

NCC-P Normalized Cross-Correlation, using P th order neighbors.

NDCC Normalized Derivative Cross-Correlation, using the 1st order time-derivative of the data.

OLS Ordinary Least Squares.

RMSE Root Mean Square Error.

SD Steepest Deflection.

SG Spatial Gradient.

SNCC Single hop-order Normalized Cross-Correlation.

SVD Singular Value Decomposition.

VA Ventricular Activity.

Bibliography

- [1] G. Santulli *et al.*, "Epidemiology of cardiovascular disease in the 21st century: updated numbers and updated facts," *J Cardiovasc Dis*, vol. 1, no. 1, pp. 1–2, 2013.
- [2] D. Mozaffarian, E. J. Benjamin, A. S. Go, D. K. Arnett, M. J. Blaha, M. Cushman, S. R. Das, S. De Ferranti, J.-P. Després, H. J. Fullerton, *et al.*, "Executive summary: heart disease and stroke statistics, 2016 update: a report from the american heart association," *Circulation*, vol. 133, no. 4, pp. 447–454, 2016.
- [3] A. D. Krahn, J. Manfreda, R. B. Tate, F. A. Mathewson, and T. E. Cuddy, "The natural history of atrial fibrillation: Incidence, risk factors, and prognosis in the manitoba follow-up study," *The American Journal of Medicine*, vol. 98, no. 5, pp. 476 – 484, 1995.
- [4] S. S. Chugh, R. Havmoeller, K. Narayanan, D. Singh, M. Rienstra, E. J. Benjamin, R. F. Gillum, Y.-H. Kim, J. H. McNulty Jr, Z.-J. Zheng, *et al.*, "Worldwide epidemiology of atrial fibrillation: a global burden of disease 2010 study," *Circulation*, vol. 129, no. 8, pp. 837–847, 2014.
- [5] H. Calkins, G. Hindricks, R. Cappato, Y.-H. Kim, E. B. Saad, L. Aguinaga, J. G. Akar, V. Badhwar, J. Brugada, J. Camm, P.-S. Chen, S.-A. Chen, M. K. Chung, J. Cosedis Nielsen, A. B. Curtis, D. W. Davies, J. D. Day, A. d'Avila, N. M. S. (Natasja) de Groot, L. Di Biase, M. Duytschaever, J. R. Edgerton, K. A. Ellenbogen, P. T. Ellinor, S. Ernst, G. Fenelon, E. P. Gerstenfeld, D. E. Haines, M. Haissaguerre, R. H. Helm, E. Hylek, W. M. Jackman, J. Jalife, J. M. Kalman, J. Kautzner, H. Kottkamp, K. H. Kuck, K. Kumagai, R. Lee, T. Lewalter, B. D. Lindsay, L. Macle, M. Mansour, F. E. Marchlinski, G. F. Michaud, H. Nakagawa, A. Natale, S. Nattel, K. Okumura, D. Packer, E. Pokushalov, M. R. Reynolds, P. Sanders, M. Scanavacca, R. Schilling, C. Tondo, H.-M. Tsao, A. Verma, D. J. Wilber, T. Yamane, and D. Reviewers:, "2017 hrs/ehra/ecas/aphrs/solaece expert consensus statement on catheter and surgical ablation of atrial fibrillation," *EP Europace*, vol. 20, no. 1, pp. e1–e160, 2018.
- [6] W. Einthoven, "Galvanometrische registratie van het menselijk electrocardiogram," *Herinneringsbundel Professor S.S. Rosenstein. Leiden: Eduard Ijdo*, pp. 101–107, 1902.
- [7] P. Kligfield, "The centennial of the einthoven electrocardiogram," *Journal of Electrocardiology*, vol. 35, no. 4, Part B, pp. 123 – 129, 2002.
- [8] W. Fye, "A history of the origin, evolution, and impact of electrocardiography," *The American Journal of Cardiology*, vol. 73, no. 13, pp. 937 – 949, 1994.
- [9] A. Yaksh, L. J. van der Does, C. Kik, P. Knops, F. B. Oei, P. C. van de Woestijne, J. A. Bekkers, A. J. Bogers, M. A. Allesie, and N. M. de Groot, "A novel intra-operative, high-resolution atrial mapping approach," *Journal of Interventional Cardiac Electrophysiology*, vol. 44, pp. 221–225, Dec 2015.
- [10] M. S. Spach, R. C. Barr, G. A. Serwer, J. M. Kootsey, and E. A. JOHNSON, "Extracellular potentials related to intracellular action potentials in the dog purkinje system," *Circulation research*, vol. 30, no. 5, pp. 505–519, 1972.
- [11] S. M. Shors, A. V. Sahakian, H. J. Sih, and S. Swiryn, "A method for determining high-resolution activation time delays in unipolar cardiac mapping," *IEEE transactions on biomedical engineering*, vol. 43, no. 12, pp. 1192–1196, 1996.
- [12] J. G. Betts, *Anatomy and physiology*. Houston, Texas: OpenStax College, Rice University, 2013.
- [13] D. E. Wilcken, "Physiology of the normal heart," *Surgery (Oxford)*, vol. 36, no. 2, pp. 48 – 51, 2018.
- [14] S. Weidmann, "Electrical constants of trabecular muscle from mammalian heart," *The Journal of physiology*, vol. 210, no. 4, pp. 1041–1054, 1970.
- [15] N. Jost, "Transmembrane ionic currents underlying cardiac action potential in mammalian hearts," *Advances in cardiomyocyte research. Ed. Péter P. Nánási. Transworld Research Network, Tivandrum, Kerala, India*, pp. 1–45, 2009.
- [16] M. Courtemanche, R. J. Ramirez, and S. Nattel, "Ionic mechanisms underlying human atrial action potential properties: insights from a mathematical model," *American Journal of Physiology-Heart and Circulatory Physiology*, vol. 275, no. 1, pp. H301–H321, 1998.
- [17] W. Einthoven, "Ueber die form des menschlichen electrocardiogramms," *Archiv für die gesamte Physiologie des Menschen und der Tiere*, vol. 60, pp. 101–123, Mar 1895.
- [18] T. Lewis, "Report cxix. auricular fibrillation: A common clinical condition," *BMJ*, vol. 2, no. 2552, pp. 1528–1528, 1909.
- [19] E. Prystowsky, "Tachycardia-induced-tachycardia: a mechanism of initiation of atrial fibrillation," *Atrial Arrhythmias: State of the Art. Armonk, NY: Futura*, pp. 81–95, 1995.
- [20] M. M. Gallagher and J. Camm, "Classification of atrial fibrillation," *The American Journal of Cardiology*, vol. 82, no. 7, Supplement 1, pp. 18N – 28N, 1998.

- [21] J. W. Waks and M. E. Josephson, "Mechanisms of atrial fibrillation—reentry, rotors and reality," *Arrhythmia & electrophysiology review*, vol. 3, no. 2, p. 90, 2014.
- [22] G. K. Moe, "Atrial fibrillation as a self sustaining arrhythmia independent of focal discharge," *American Heart Journal*, vol. 58, pp. 59–70, 1959.
- [23] G. K. Moe, W. C. Rheinboldt, and J. Abildskov, "A computer model of atrial fibrillation," *American Heart Journal*, vol. 67, no. 2, pp. 200–220, 1964.
- [24] K. T. Konings, C. J. Kirchhof, J. R. Smeets, H. J. Wellens, O. C. Penn, and M. A. Allesie, "High-density mapping of electrically induced atrial fibrillation in humans," *Circulation*, vol. 89, no. 4, pp. 1665–1680, 1994.
- [25] E. A. Lanters, A. Yaksh, C. P. Teuwen, L. J. van der Does, C. Kik, P. Knops, D. M. van Marion, B. J. Brundel, A. J. Bogers, M. A. Allesie, *et al.*, "Spatial distribution of conduction disorders during sinus rhythm," *International journal of cardiology*, vol. 249, pp. 220–225, 2017.
- [26] M. A. Allesie, N. M. S. de Groot, R. P. M. Houben, U. Schotten, E. Boersma, J. L. Smeets, and H. J. Crijns, "Electropathological substrate of long-standing persistent atrial fibrillation in patients with structural heart disease: longitudinal dissociation," *Circulation: Arrhythmia and Electrophysiology*, vol. 3, no. 6, pp. 606–615, 2010.
- [27] N. M. S. de Groot, R. P. M. Houben, J. R. L. M. Smeets, E. Boersma, U. Schotten, M. J. Schalij, H. J. Crijns, and M. A. Allesie, "Electropathological substrate of longstanding persistent atrial fibrillation in patients with structural heart disease: epicardial breakthrough," *Circulation*, vol. 122 17, pp. 1674–82, 2010.
- [28] M. Haïssaguerre, P. Jaïs, D. C. Shah, A. Takahashi, M. Hocini, G. Quiniou, S. Garrigue, A. Le Mouroux, P. Le Métayer, and J. Clémenty, "Spontaneous initiation of atrial fibrillation by ectopic beats originating in the pulmonary veins," *New England Journal of Medicine*, vol. 339, no. 10, pp. 659–666, 1998. PMID: 9725923.
- [29] S. V. Pandit and J. Jalife, "Rotors and the dynamics of cardiac fibrillation," *Circulation research*, vol. 112, no. 5, pp. 849–862, 2013.
- [30] S. M. Narayan, D. E. Krummen, and W.-J. RAPPÉL, "Clinical mapping approach to diagnose electrical rotors and focal impulse sources for human atrial fibrillation," *Journal of cardiovascular electrophysiology*, vol. 23, no. 5, pp. 447–454, 2012.
- [31] A. Bajpai, I. Savelieva, and A. J. Camm, "Treatment of atrial fibrillation," *British Medical Bulletin*, vol. 88, no. 1, pp. 75–94, 2008.
- [32] M. Haïssaguerre, P. Sanders, M. Hocini, Y. Takahashi, M. Rotter, F. Sacher, T. Rostock, L.-f. Hsu, P. Bordachar, S. Reuter, R. Roudaut, J. Clémenty, and P. Jaïs, "Catheter ablation of long-lasting persistent atrial fibrillation: Critical structures for termination," *Journal of Cardiovascular Electrophysiology*, vol. 16, no. 11, pp. 1125–1137, 2005.
- [33] T. Baykaner, A. J. Rogers, G. L. Meckler, J. Zaman, R. Navara, M. Rodrigo, M. Alhousseini, C. A. Kowalewski, M. N. Viswanathan, S. M. Narayan, *et al.*, "Clinical implications of ablation of drivers for atrial fibrillation: a systematic review and meta-analysis," *Circulation: Arrhythmia and Electrophysiology*, vol. 11, no. 5, p. e006119, 2018.
- [34] M. A. Allesie, K. Konings, C. J. Kirchhof, and M. Wijffels, "Electrophysiologic mechanisms of perpetuation of atrial fibrillation," *The American Journal of Cardiology*, vol. 77, no. 3, pp. 10A–23A, 1996. A Symposium: Supraventricular Arrhythmias: Update 1995.
- [35] J. L. Cox, T. Canavan, R. Schuessler, M. Cain, B. Lindsay, C. Stone, P. Smith, P. Corr, and J. Boineau, "The surgical treatment of atrial fibrillation. ii. intraoperative electrophysiologic mapping and description of the electrophysiologic basis of atrial flutter and atrial fibrillation," *The Journal of thoracic and cardiovascular surgery*, vol. 101, no. 3, pp. 406–426, 1991.
- [36] M. A. Allesie, "Total mapping of atrial excitation during acetylcholine-induced atrial flutter and fibrillation in the isolated canine heart," *Atrial fibrillation*, vol. 44, 1982.
- [37] M. A. Allesie, "Experimental evaluation of moe's multiple wavelet hypothesis of atrial fibrillation," *Cardiac electrophysiology and arrhythmias*, pp. 265–275, 1985.
- [38] T. Sueda, H. Nagata, H. Shikata, K. Orihashi, S. Morita, M. Sueshiro, K. Okada, and Y. Matsuura, "Simple left atrial procedure for chronic atrial fibrillation associated with mitral valve disease," *The Annals of Thoracic Surgery*, vol. 62, no. 6, pp. 1796–1800, 1996.
- [39] T. Nitta, Y. Ishii, Y. Miyagi, H. Ohmori, S.-i. Sakamoto, and S. Tanaka, "Concurrent multiple left atrial focal activations with fibrillatory conduction and right atrial focal or reentrant activation as the mechanism in atrial fibrillation," *The Journal of thoracic and cardiovascular surgery*, vol. 127, no. 3, pp. 770–778, 2004.
- [40] M. Holm, R. Johansson, J. Brandt, C. Lührs, and S. B. Olsson, "Epicardial right atrial free wall mapping in chronic atrial fibrillation: documentation of repetitive activation with a focal spread - a hitherto unrecognised phenomenon in man," *European Heart Journal*, vol. 18, no. 2, pp. 290–310, 1997.
- [41] N. Virag, V. Jacquemet, C. Henriquez, S. Zozor, O. Blanc, J.-M. Vesin, E. Pruvot, and L. Kappenberger, "Study of atrial arrhythmias in a computer model based on magnetic resonance images of human atria," *Chaos: An Interdisciplinary Journal of Nonlinear Science*, vol. 12, no. 3, pp. 754–763, 2002.
- [42] C. D. Cantwell, C. H. Roney, F. S. Ng, J. H. Siggers, S. Sherwin, and N. S. Peters, "Techniques for automated local activation time annotation and conduction velocity estimation in cardiac mapping," *Computers in biology and medicine*, vol. 65, pp. 229–242, 2015.

- [43] B. M. Steinhaus, "Estimating cardiac transmembrane activation and recovery times from unipolar and bipolar extracellular electrograms: a simulation study," *Circulation research*, vol. 64, no. 3, pp. 449–462, 1989.
- [44] M. S. Spach and J. M. Kootsey, "Relating the sodium current and conductance to the shape of transmembrane and extracellular potentials by simulation effects of propagation boundaries," *IEEE transactions on biomedical engineering*, no. 10, pp. 743–755, 1985.
- [45] M. S. Spach and P. C. Dolber, "Relating extracellular potentials and their derivatives to anisotropic propagation at a microscopic level in human cardiac muscle. evidence for electrical uncoupling of side-to-side fiber connections with increasing age.," *Circulation research*, vol. 58, no. 3, pp. 356–371, 1986.
- [46] R. Dubois, S. Labarthe, Y. Coudière, M. Hocini, and M. Haïssaguerre, "Global and directional activation maps for cardiac mapping in electrophysiology," in *2012 Computing in Cardiology*, pp. 349–352, IEEE, 2012.
- [47] J. Duchateau, M. Potse, and R. Dubois, "Spatially coherent activation maps for electrocardiographic imaging," *IEEE Transactions on Biomedical Engineering*, vol. 64, no. 5, pp. 1149–1156, 2017.
- [48] W. S. Ellis, S. J. Eisenberg, D. M. Auslander, M. W. Dae, A. Zakhor, and M. D. Lesh, "Deconvolution: A novel signal processing approach for determining activation time from fractionated electrograms and detecting infarcted tissue," *Circulation*, vol. 94, no. 10, pp. 2633–2640, 1996.
- [49] I. Chouvarda, N. Maglaveras, J. M. de Bakker, F. J. van Capelle, and C. Pappas, "Deconvolution and wavelet-based methods for membrane current estimation from simulated fractionated electrograms," *IEEE transactions on biomedical engineering*, vol. 48, no. 3, pp. 294–301, 2001.
- [50] B. Abdi, R. C. Hendriks, A.-J. van der Veen, and N. M. de Groot, "A compact matrix model for atrial electrograms for tissue conductivity estimation," *Computers in Biology and Medicine*, 2019.
- [51] B. B. Punske, Q. Ni, R. L. Lux, R. S. Macleod, P. R. Ershler, T. J. Dustman, M. J. Allison, and B. Taccardi, "Spatial methods of epicardial activation time determination in normal hearts," *Annals of biomedical engineering*, vol. 31, no. 7, pp. 781–792, 2003.
- [52] E. J. Ciaccio, M. M. Scheinman, V. Fridman, H. Schmitt, J. Coromilas, and A. L. Wit, "Dynamic changes in electrogram morphology at functional lines of block in reentrant circuits during ventricular tachycardia in the infarcted canine heart: a new method to localize reentrant circuits from electrogram features using adaptive template matching," *Journal of cardiovascular electrophysiology*, vol. 10, no. 2, pp. 194–213, 1999.
- [53] R. P. Houben, N. M. de Groot, F. W. Lindemans, and M. A. Allesie, "Automatic mapping of human atrial fibrillation by template matching," *Heart Rhythm*, vol. 3, no. 10, pp. 1221–1228, 2006.
- [54] R. Plonsey and R. C. Barr, *Bioelectricity: a quantitative approach*. Springer Science & Business Media, 2007.
- [55] S. M. Kay, *Fundamentals of statistical signal processing*, vol. Volume I: Estimation Theory of *Prentice Hall signal processing series*. Upper Saddle River, NJ: Prentice Hall PTR, 1993.
- [56] A. Ben-Israel and T. N. Greville, *Generalized inverses: theory and applications*, vol. 15. Springer Science & Business Media, 2003.
- [57] A. C. Aitken, "Iv. on least squares and linear combination of observations," *Proceedings of the Royal Society of Edinburgh*, vol. 55, pp. 42–48, 1936.
- [58] H. White *et al.*, "A heteroskedasticity-consistent covariance matrix estimator and a direct test for heteroskedasticity," *econometrica*, vol. 48, no. 4, pp. 817–838, 1980.
- [59] T. Amemiya, *Advanced econometrics*. Harvard university press, 1985.
- [60] A. Amiri-Simkooei, "Weighted total least squares with singular covariance matrices subject to weighted and hard constraints," *Journal of Surveying Engineering*, vol. 143, no. 4, p. 04017018, 2017.
- [61] C. R. Henderson, O. Kempthorne, S. R. Searle, and C. Von Krosigk, "The estimation of environmental and genetic trends from records subject to culling," *Biometrics*, vol. 15, no. 2, pp. 192–218, 1959.
- [62] S. R. Searle and A. I. Khuri, *Matrix algebra useful for statistics*. John Wiley & Sons, 2017.
- [63] H. Cramér, *Mathematical methods of statistics*, ch. 32. Princeton U. Press, Princeton, 1946.